NONLINEARITIES AND NOISE IN MICROMECHANICAL RESONATORS: FROM UNDERSTANDING TO CHARACTERIZATION AND DESIGN TOOLS

By

Pavel M. Polunin

A DISSERTATION

Submitted to
Michigan State University
in partial fulfillment of the requirements
for the degree of

Mechanical Engineering - Doctor of Philosophy
Physics - Doctor of Philosophy

2016

ABSTRACT

NONLINEARITIES AND NOISE IN MICROMECHANICAL RESONATORS: FROM UNDERSTANDING TO CHARACTERIZATION AND DESIGN TOOLS

By

Pavel M. Polunin

In this work we consider several nonlinearity-based and/or noise-related phenomena that were observed recently in micro-electromechanical resonators. The main goal here is to closely examine these phenomena, understand their underlying fundamental physics, and find ways to employ them for measurement purposes and/or to improve the performance of specific classes of micro-electromechanical systems (MEMS). The general perspective of this work is based on the acceptance of the fact that nonlinearity and noise represent integral parts of the models for these systems, and the discussion is constructed about the cases where these generally "undesirable" features can be utilized rather than avoided.

In this dissertation we consider three different, but related, topics. To start, we analyze the stationary probability distribution of a nonlinear resonator driven by Poisson noise at a non-zero temperature of the environment. We show that Poisson pulses with low pulse rates cause the power-law divergence of the probability density at the resonator equilibrium in the rotating frame both in overdamped and underdamped regimes. We have also found that the shape of the probability distribution away from the equilibrium position is qualitatively different for overdamped and underdamped cases. In particular, in the overdamped regime, the form of the secondary singularity in the probability distribution strongly depends on the reference phase of the resonator response as well as the pulse modulation phase, while in the underdamped regime there are several singular peaks, and their location is determined by the resonator decay rate in the rotating frame. Finally, we show that even weak Gaussian

noise affects the probability distribution by smoothing it in the vicinity of singular peaks.

Second, we discuss a time-domain technique for characterizing parameters for models of a single vibrational mode of symmetric micromechanical resonators, including coefficients of conservative and dissipative nonlinearities as well as the strengths of noise sources acting on the mode of interest. These nonlinearities result in an amplitude-dependent frequency and a non-exponential decay, while noise sources cause fluctuations in the resonator amplitude and phase. We capture these features in the modal ringdown response. Analysis of the amplitude of the ringdown response allows one to estimate the quality factor and the dissipative nonlinearity, and the zero-crossing points in the ringdown measurement can be used for characterization of the linear natural frequency and the Duffing and quintic nonlinearities of the vibrational mode which arise from a combination of mechanical and electrostatic effects. Additionally, we show that statistical analysis of the zero-crossing points in the resonator response allows us to separate effects of additive, multiplicative, and measurement noises and estimate their corresponding intensities.

Finally, we examine the problem of self-induced parametric amplification in ring/disk resonating gyroscopes. We model the dynamics of this type gyroscopes by considering flexural (elliptical) vibrations of a free thin ring and show that the parametric amplification arises naturally from a nonlinear intermodal coupling between the drive and sense modes of the gyroscope. Analysis shows that this modal coupling results in substantial increase in the sensitivity of the gyroscope to the external angular rate. This improvement in the gyroscope performance strongly depends both on the modal coupling strength and the operating point of the gyroscope, and we further explore ways to enhance this effect by changing the shape of the resonator body and attendant electrodes and utilizing electrostatic tuning.

ACKNOWLEDGMENTS

Looking back at my three and a half years of working on my Ph.D. dissertation at Michigan State University, there are many people who provided their support, guidance, motivation, encouragement, and feedback and to whom I am sincerely grateful for this.

First of all, I would like to express my sincerest gratitude to my academic advisers: Professor Steven W. Shaw and Professor Mark I. Dykman, for their patience, continuous support, and encouragement during my Ph.D. program. Besides providing their academic instruction and technical guidance, both Steve and Mark have been my great mentors in many aspects of my life (including surfing Florida waves or finding perfect sweets in East Lansing area), and their mentorship will keep guiding me through my professional career and personal life. I am truly honored to have had an opportunity to work with Professor Shaw and Dykman and learn from these experts.

I am also very grateful to my Guidance Committee Members: Professor Brian F. Feeny, Professor Vladimir G. Zelevinsky, and Professor Ranjan Mukherjee, for their invaluable feedback during my graduate program and overseeing this dissertation. I have been extremely fortunate to take a few classes with each of these gentlemen, from whom I learned many interesting theories and methods that helped me in my work on this dissertation.

Next, I would like to thank my collaborators: Professor Thomas W. Kenny (Stanford), Professor Ho Bun Chan (HKUST), and Professor Kimberly L. Turner (UCSB). I have deeply enjoyed working with these outstanding scholars and their students. Special thanks here goes to Yushi Yang (Stanford), Lily L. Li (UCSB), and Panpan Zhou (HKUST) for numerous in-depth discussions, both on science and life in general, which have broaden my horizons in different directions.

Special thanks goes to my former and fellow lab-mates for a very friendly and warm atmosphere that we have kept in our lab and that has triggered countless coversations about peculiar scientific problems and life challenges. These include Nick Miller, Scott Strachan, Oriel Shoshani, Venkat Ramakrishnan, Brendan Vidmar, Mustafa Acar, Gizem Acar, Smruti Panigrahi, Xing Xing, Kirill Moskovtsev, Yaxing Zhang, Juan Atalaya, and Ayse Sapmaz.

A huge thanks goes to my wonderful friends: Andrey Maslennikov, Oleksii Karpenko, Oleg Tarasov, Anton Efremov, Brian Zhou, and Jennifer Kirk, for helping me to maintain a healthy work-and-life balance. I feel very lucky to have you in my life.

To my family back in Russia, there are no words that can express my love and gratitude towards my family members. Thank you, Mom and Dad, for your endless support, unconditional love, and your encouragement during difficult periods of my life. Last but not least, thanks goes to my dear and lovely wife Roshan Angoshtari for her continuous love, support, patience, and understanding during my on-going life adventure.

TABLE OF CONTENTS

LIST OF TABLES

LIST OF FIGURES

Chapter 1

Introduction

Generally, micro-electro-mechanical systems (MEMS) that can be described by linear models are more widely desired for applications, while systems exhibiting nonlinear behavior are avoided. There are a number of reasons for this, including the fact that the dynamic behavior of linear systems is well understood, that these systems are significantly simpler from characterization and design points of view, and that they allow for relatively simple tuning in terms of system model parameters. At the same time, MEMS operating in their linear regimes have certain fundamental limitations in terms of their performance, due to the restricted nature of their input-output properties and the fact that the linear range is often restrictively small in many applications. Furthermore, linear systems are not suitable for applications that necessarily involve nonlinear phenomena, like the limit cycles required for frequency generators [1, 2], certain types of atomic force microscopy [3–5], and the sub- and super-harmonics needed for frequency conversion [6, 7] in signal processing applications. Noise sources are generally treated as unwanted in MEMS since they negatively affect device performance by reducing their precision. While this is generally true, systematic approaches for reducing the effects of noise on the system dynamics cannot be fully realized without a detailed understanding of the noise properties and, preferably, knowledge of their origins [8–10]. As a result, further improvement in the performance of these MEMS requires a comprehensive understanding of various nonlinear and noise-induced phenomena.

In this chapter we describe the scientific background that motivated present research

and outline the main contributions described in this dissertation. In Section 1.1 we briefly introduce readers to the field of micro-electromechanical systems and discuss the importance of studying nonlinear behavior in MEMS. In Section 1.2 we elicit the physical origin of the nonlinearities and noise sources in MEMS models, as well as their effect on the system dynamic behavior, and describe recent findings that motivated current these research efforts. In Section 1.3 we summarize our major contributions to this field.

1.1 Why nonlinear and noisy models for MEMS?

*Design for **linear** dynamic range is a **nonlinear** problem.*

– Steven W. Shaw

Micro-electromechanical systems is a well established field of science that was initiated by the pioneering concepts and ideas of Feynman [11], Nathanson [12] and Petersen [13]. Here we focus on MEMS resonators, that is, vibratory devices with light damping, which have achieved success in numerous applications, including stable frequency generation [14–17], precise sensing [18, 19], and signal processing [20, 21], to name but a few. For a detailed overview of different types of MEMS operating in their linear regime we refer the reader to [22], while here we focus on nonlinear behavior of MEMS resonators and highlight features that make this an important and interesting field for research.

In time-keeping and sensing applications, quartz crystal resonators provide highly stable and precise frequency-selective elements, but their relatively large size, as compared with MEMS, makes it challenging to integrate them with integrated circuit technologies. This is a crucial shortcoming in modern applications, such as health monitoring and smartphone applications, which are driven by continuos miniaturization. MEMS provide a promising

alternative to quartz resonators due to their small dimensions, low power consumption, and excellent on-chip integrability [23–25]. Additionally, their small effective mass makes MEMS ideal candidates for a number of sensing applications, for example the precise measurement of acceleration [26], angular rate [27], mass [18], force [28] and electron spin [29]. On the other hand, these very features of MEMS resonators make them extremely sensitive to various noise sources, such as those arising from thermal and electronic fluctuations, which degrade the performance of MEMS devices. Specifically, the strong susceptibility of MEMS resonators to noise sources results in relatively low signal-to-noise ratios (SNR) when operating in their linear dynamic range.

The standard way to increase SNR and improve, for example, sensor measurement precision, is to drive MEMS resonators to larger vibration amplitudes. However, as the resonator vibration energy increases, various nonlinear effects come into play, thus making linear system models no longer valid. In this situation, we have two general options to choose: one option is to operate the device at the onset of nonlinearity; in this case the system response essentially remains linear, but we limit ourselves by relatively low vibration amplitude, resulting in low SNR and limited device performance and precision. Another option is to drive the resonator in its nonlinear regime, which allows one to improve the SNR, but at the cost of facing and dealing with nonlinearity-induced phenomena, such as amplitude-dependent vibration frequency [30, 31] and nonlinear friction [32–35].

As noted above, nonlinear system models are significantly more complicated to work with when compared to linear models and, as a result, the majority of contemporary MEMS-based systems operate in their linear range [36–38]. Recently, several research groups have investigated different approaches to increase the linear range of existing MEMS resonators [39–42]. In this situation, as practice shows, in order to design a resonator with increased linear

range [43] or reduced phase noise [1], it is first necessary to obtain a comprehensive understanding of the nonlinearities and/or noise sources one is trying to minimize or eliminate. In this thesis we take a different approach; rather than avoiding and/or neglecting nonlinearities and noise, we focus on: (i) methods for characterizing nonlinearity and noise, (ii) achieving a better understanding of their effects on system dynamic behavior, and (iii) utilizing this knowledge to design systems with improved performance.

1.2 Nonlinearities and noise in MEMS

Any vibrational system will exhibit nonlinear behavior under some operating conditions. Linear models serve as first-order approximations to the system description, and in certain cases the accuracy provided by these approximations is sufficient for an accurate description of observed phenomena, while in other situations one must necessarily go beyond this assumption and account for higher-order (nonlinear) effects.

In MEMS resonators nonlinearities can be separated in two major groups. The first group of nonlinear effects arise from mechanical properties and are associated with the resonator body itself. These include nonlinearities due to resonator vibrations at large amplitudes, and can be further classified into material and kinematic effects. Material nonlinearities arise at large vibration amplitudes due to the fact that material properties such as Young's modulus actually depend on the vibration amplitude [31] and the orientation of the strain field with respect to crystallographic principal axes, which is important in, for example, resonators made of single crystal silicon [38] or other anisotropic materials. In addition, it has been found recently that doping level can affect resonator response at large vibration amplitudes in a non-trivial way [44]. Generally, material nonlinearities affect the resonator potential

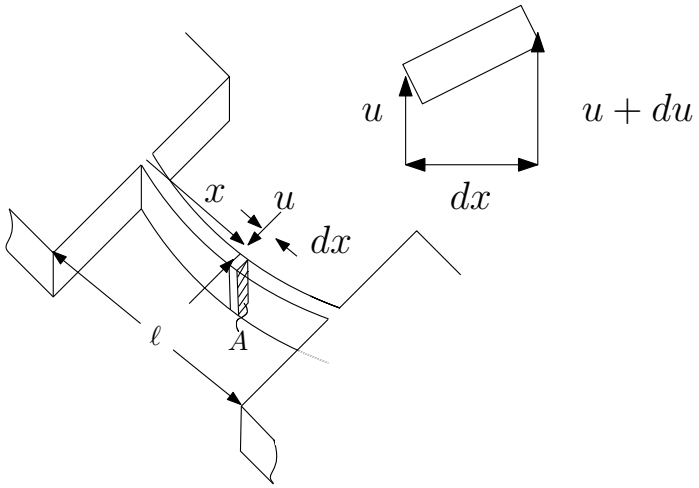

Figure 1.1: Schematic representation of the flexural vibration of a clamped-clamped beam, shown in a deformed configuration. The element depicted in the beam, and shown top-view in the inset, is used to derive the non-linear effects of mid-line stretching [46].

energy while leaving the kinetic energy unchanged. On the other hand, kinematic nonlinearities result from finite deformations of the resonator body during its vibration. In this case, the particular way nonlinear effects reveal themselves depends of the vibrational mode shape and can result in nonlinear stiffness and/or nonlinear inertial terms. In particular, for flexural vibrations of a clamped-clamped beam resonator, which will be considered in Chapter 3, the mid-line stretching of the resonator at large vibrational amplitudes results in a nonlinear modal restoring force [45]; see Fig. 1.1. This mid-line stretching leads to an amplitude-dependent vibration frequency and has to be taken into account at relatively small vibration amplitudes, specifically, at amplitudes on the order of the beam thickness. When it comes to flexural in-plane vibrations of rings, for example, for the elliptic vibrational modes in micromechanical gyroscopes, kinematic nonlinearities appear not only in the system potential energy, but also alter the kinetic energy of the resonator body, leading to inertial nonlinearities, as discussed in detail in Chapter 4. Kinematic nonlinearities also affect the resonator kinetic energy in cantilever beam resonators, which are commonly used

in sensing applications [47, 48].

A second major group of nonlinear effects is associated with the interaction of the resonator body with the environment, for example, used for actuation of the resonator and for transduction of signals from the resonator response. In this work we focus our attention on electrostatically driven MEMS resonators with capacitive actuation and readout schemes [22]. The electrostatic potential is a highly nonlinear function of the resonator displacement and depends inversely on the distance between the resonator body and the attendant electrodes. When the vibration amplitude a is small as compared with the electrode gap size d, $a \ll d$, the corresponding electrostatic forces can be approximated as linear functions of the resonator modal amplitude. On the other hand, when $a \sim d$, even $a \sim 0.1d$, the linear approximation of the electrostatic forces is no longer valid and one must keep higher-order terms in the electrostatic force model.

Note that the aforementioned nonlinearities in MEMS resonators have different physical origins and, as a consequence, generally contribute to the resonator dynamics at different vibration amplitudes. Therefore, it can happen that more than one source of nonlinearity affects the resonator dynamic behavior for a given vibration energy. In this case, nonlinearities originating from different sources, e.g. mid-line stretching and the electrostatic potential, essentially renormalize each other in the corresponding nonlinear terms in the resonator modal restoring force. This interplay of different nonlinear effects can result in very interesting and non-trivial resonator responses, such as that shown on Fig. 1.2.

Damping, or friction, also originates from the interaction of the resonator with its environment, which necessarily has temperature T. This interaction is captured by the coupling of the resonator to a thermal bath, and the effects we are about to describe, which include damping and noise, have a *thermal* origin. In a useful framework, the resonator is mod-

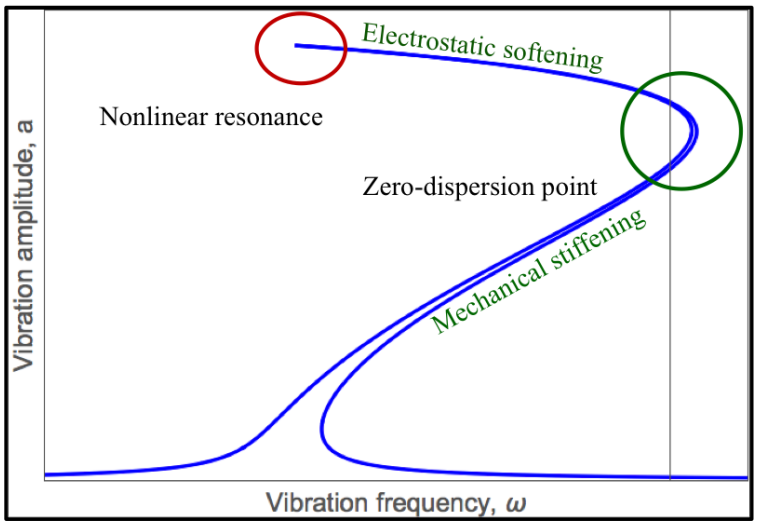

Figure 1.2: Frequency response showing the combined effects of mechanical and electrostatic nonlinearities. At small vibration amplitudes the mechanical component of the nonlinear restoring force dominates the electrostatic effects, leading to hardening behavior. As the vibration amplitude increases, the electrostatic forces starts to play a more dominant role, resulting in the appearance of the so-called zero-dispersion point on the resonator frequency response, beyond which the resonator behavior is softening.

eled as interacting with a set of microscopic "oscillators" that describe the modes of the environment according to the following model,

$$\ddot{q} + U'(q) = -\frac{\partial U_i(q, \{q_k\})}{\partial q}, \tag{1.1a}$$

$$\ddot{q}_k + \omega_k^2 q_k = -\frac{\partial U_i(q, \{q_k\})}{\partial q_k}, \tag{1.1b}$$

where $U(q)$ is the resonator potential, which can be harmonic or anharmonic, q_k denotes the coordinate associated with a mode of the bath ($k = 1, 2, ..., N$, where $N \gg 1$), and $U_i(q, \{q_k\})$ is the interaction potential between the resonator of interest and the modes of the thermal bath. In the simplest case, this interaction potential has the form

$$U_i(q, \{q_k\}) = q \sum_k \epsilon_k q_k, \tag{1.2}$$

where ϵ_k describes the coupling strength of the resonator of interest with the k^{th} mode of the environment. Considering this simple form of $U_i(q, \{q_k\})$, one can show that this interaction leads to irreversible losses of the resonator vibration energy, i.e., decay of unforced vibrations, and results in a random force acting on the resonant mode [49]. When the resonator vibration amplitude is relatively small, its decay rate is essentially constant and the random force is independent of the resonator modal coordinate, which is modeled as an additive noise [33]. As expected, when the resonator vibration energy is large, the coupling of the resonator to the environment becomes nonlinear, which results in an amplitude-dependent friction coefficient (nonlinear damping) and additional parametric noise [50].

The nature of the noise processes acting on the resonator is, however, not limited to thermal origins. Depending on the system of interest and its application, there can exist different microscopic effects interacting with the resonator directly or through the attendant electrodes and thus affecting the system dynamic behavior. In a mass sensing experiment, for example, a frequently encountered source of noise is a random process associated with the attachment/detachment of molecules to the resonator surface [51]. Due to the finite mass of these molecules, the resonator effective mass changes in a discrete manner, $m \to m + \delta m$, which results in discrete change of the resonator natural frequency,

$$\omega + \delta\omega = \sqrt{\frac{k}{m + \delta m}} \approx \omega\left(1 - \frac{\delta m}{2m}\right), \quad \to \quad \delta\omega \approx -\omega\frac{\delta m}{2m}, \tag{1.3}$$

where k is the resonator effective linear stiffness and it is assumed that $\delta m \ll m$, i.e., the mass of individual molecules is much smaller as compared with the resonator effective mass. Depending on the time scale of this attachment/detachment process, the associated frequency noise can treated as white Gaussian, Poisson (see Chapter 2 and Appendix A) or

telegraph, and, in general, will have different effects on the resonator dynamics.

Another type of noise that is inherently present in virtually all systems is so-called *measurement* or *detector* noise, which appears due to imperfections of the sensing/detection scheme. Typically, this noise manifests itself in a random perturbation added to the measured signal, for example, a voltage corresponding to the resonator modal displacement or velocity. While this noise is assumed to have no effect on the resonator dynamics itself, its effect on the measured signal can be frequently attributed to some "unaccounted" noises acting on the resonator, which can obviously lead to discrepancies in analytical predictions and/or misleading conclusions. As a result, it is important to be able to distinguish different noise sources present in MEMS resonators in order to explain their dynamic behavior, and to account for them to improve performance.

The brief overview of nonlinear and noise processes presented above motivates the need for a better understanding of these phenomena in MEMS resonators and the development of accurate characterization techniques for quantifying these effects. A thorough and comprehensive understanding of these nonlinear and noise-induced effects allows not only for effective prediction of the resonator response across a wide range of model parameters and operating conditions, but also provides information that is essential for designing MEMS resonators with desired dynamic behavior, see Fig. 1.3. At the same time, characterization methods also play an important role in developing a fundamental understanding of the underlying physics, while also providing information about MEMS performance.

In this light, the main goal of this dissertation is to push forward the frontiers of our fundamental understanding of different nonlinearities and noise processes in MEMS resonators with a focus on characterization techniques and design methods.

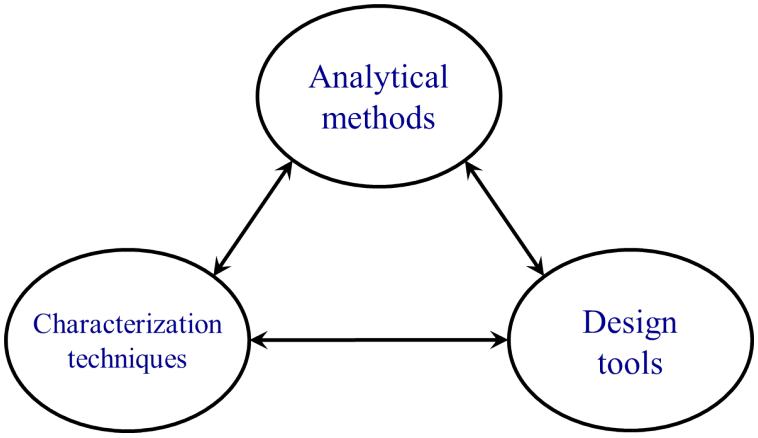

Figure 1.3: Analytical methods, effective characterization techniques, and reliable design tools are the key ingredients in building MEMS resonators with optimal performance for different applications.

1.3 Summary of the work

The first topic in this dissertation is an analysis of the stationary probability distribution of a nonlinear parametrically driven resonator under the action of Poisson pulses in the presence of thermal noise. In this case, the Poisson pulses are modulated at one half of the driving frequency, where the system sensitivity to the external force is highest. We consider the dynamics of a micro-mechanical resonator model in the rotating frame and examine its probability distribution projected onto the selected direction as a function of the Poison noise pulse rate and its modulation phase. Modulated Poisson pulses result in effective jumps in the resonator states in the rotating frame and we show that Poisson noise with low pulse rates causes a power-law divergence of the probability density at the resonator equilibrium in both the overdamped and underdamped regimes. Additionally, we have found that in the overdamped regime the form of the secondary singularity in the probability distribution, at a finite distance from the equilibrium position, strongly depends on the Poisson noise modulation phase and the phase of the resonator response. In contrast, the structure of the probability density function in the underdamped regime is essentially independent of

the selected resonator phase and Poisson pulse direction. We also examine the effect of weak additive Gaussian noise, a consequence of non-zero temperature of the environment, on the shape of the probability distribution. Analysis shows, and experimental results from collaborators at Hong Kong University of Science and Technology verify, that even weak Gaussian noise affects the probability distribution by smoothing its shape in the vicinity of Poisson noise-induced singular peaks.

Second, we describe a time-domain technique for characterizing parameters of a single vibrational mode in symmetric micro-mechanical resonators. In particular, we show that a modal ringdown response can be used for characterization of not only linear model parameters Q (quality factor) and ω_n (natural frequency), but also of coefficients representing conservative and dissipative nonlinearities, as well as the intensities and statistical properties of various types of noise sources acting on the mode of interest. These nonlinearities result in an amplitude-dependent frequency (conservative) and a non-exponential decay (dissipative), while the noise sources cause fluctuations in the resonator amplitude and phase. Specifically, we show that the behavior of the modal vibration amplitude is independent of the nonlinearities in the resonator restoring force, which allows us to estimate linear and nonlinear friction constants. On the other hand, the modal vibration frequency is determined solely (up to noise-induced fluctuations) by the form of the system potential energy, which can be used to characterize the linear natural frequency and coefficients of the cubic (Duffing) and quintic terms in the modal restoring force. Furthermore, we show that in some cases it is possible to individually characterize mechanical and electrostatic (both linear and nonlinear) effects that influence the mode dynamics, and we formulate the conditions for such characterization. Finally, we illustrate that a statistical analysis of the zero-crossing points in the modal response can reveal the presence of additive (thermal), multiplicative (frequency), and mea-

surement (readout) noise sources, providing a unique way for independent characterization of the noise strengths.

Finally, we examine the problem of self-induced parametric amplification in ring/disk resonating MEMS gyroscopes. We show that the degenerate elliptical modes of gyroscopes with ring-like geometries are coupled dispersively through both stiffness and inertial nonlinearities, and we illustrate the effects of the electrostatic potential on individual modal nonlinearities and on the strength of nonlinear modal coupling. We further study the effect of the dispersive modal coupling on the gyroscope performance and sensitivity. In particular, we illustrate that the back-action of the sense mode vibrations on the drive mode dynamics can be neglected when the strength of the modal coupling and external angular rate are small. This fact allows us to simplify the gyroscope model and treat the sense mode as being "driven" by the drive mode through the Coriolis force, as well as parametrically through nonlinear modal coupling effects, which results in a substantial increase in the sensitivity of the gyroscope to the external angular rate. Furthermore, we show how this extra gain, due to parametric amplification, depends on the drive mode vibration amplitude and the coupling strength. Finally, we use this model to demonstrate ways for additional improvement of the gyroscope performance as an angular rate sensor by adjusting the modal coupling strength through variations in the geometry of the gyroscope body and attendant electrodes, as well as utilizing electrostatic tuning methods. These modeling and optimization approaches are a first step in controlling and exploiting nonlinear behavior to improve sensor design.

Chapter 2

Singular probability distribution of vibrational systems driven by Poisson and thermal noises

In this chapter we study the probability distribution of a torsional micromechanical resonator driven by modulated Poisson pulses in the presence of weak thermal noise. Specifically, weakly damped micromechanical resonator is driven parametrically into the resonance, and both Poisson and thermal noise sources perturb the resonator dynamics about its deterministic state. Modulated Poisson noise is a sequence of bursts of the periodic signal with the frequency close to the resonator natural frequency. These bursts appear randomly and their times of arrival are independent from arrivals of previous pulses. The mean time between pulses is much longer than the resonator characteristic decay time and the duration of each burst is much longer than the resonator vibration period. This problem is of fundamental importance as it addresses the combined effects of two noises having different, descriptions, namely "continuous" and discrete in time. In the absence of Poisson noise, the weak thermal noise, having a symmetric probability distribution, essentially "thermalizes" the resonator around its stable state, in which case the resonator probability distribution in the rotating frame is Gaussian along any selected direction. In contract, the Poisson noise has drastically

different effect on the resonator dynamics. The discreteness of the noise pulses and the associated asymmetry of Poisson distribution are evident when the resonator parameters are such that its dynamics in the vicinity of the stable state exhibits overdamped behavior. For example, if Poisson pulses all have the same sign (the unipolar case), the resonator probability distribution becomes strongly asymmetric with respect to the stable state in the direction of the Poisson pulses. Depending on the Poisson mean pulse rate, the probability distribution can diverge in the location of the stable state (the case of low pulse rate) or decay to zero with a power-law of the distance to the stable state (the case of frequent pulses). When the system parameters are chosen in such a way that resonator performs decaying oscillations about its stable state (i.e., the underdamped regime), the system still can exhibit a singularity in the distribution near the stable state, but the probability distribution becomes essentially symmetric about it. In this chapter we shall also show that Poisson noise results in interesting and non-trivial features of the resonator probability distribution at a finite distance from the stable state, and illustrate the smoothing effects of the weak thermal noise on the singular behavior of the probability density functions.

Compared with the works described in subsequent chapters, the motivation for this study is more fundamental in nature. As one of the main sources of fluctuations in dynamical systems, Poisson noise attracts great interest from researchers in different areas of science. Fluctuations induced by Poisson pulses can be effectively used to analyze mesoscopic devices providing access to physics of these systems due to non-vanishing high-order statistics [52]. However, estimation of non-Gaussian distributions is often quite challenging and involves sophisticated techniques in direct measurement processes [53, 54]. Alternative theoretical approaches proposed for microresonators [55–57] and Josephson junctions [58–60] rely on the breaking of the symmetry in random switching of the system between its stable states

that stems from the inherent Gaussian noise. Already these examples clearly show the necessity for better understanding of the dynamic behavior of mesoscopic systems driven by Poisson noise.

A significant amount of work has been done in analyzing the features of activated escape due to Poisson noise [61–64]. Additionally, the probability distribution of a linear resonator driven by Poisson pulses in a static potential was investigated in detail by Ichiki et al. [9]. In particular, it has been shown that the probability distribution exhibits a singular peak in the origin for arbitrary damping, as long as the Poisson mean pulse rate is sufficiently small. The behavior of the distribution away from the origin, however, depends on the dynamic regime of the system in the vicinity of its stable state (overdamped or underdamped), the relative strength of the resonator damping as compared with its natural frequency, and on the mean frequency of the Poisson pulses.

In this chapter we take one step further in understanding Poisson noise-induced dynamics of mesoscopic systems by examining the stationary probability distribution (in the rotating frame) of a parametric resonator driven by modulated Poisson pulses and weak thermal noise. In particular, we show that, upon transformation to the rotating frame, modulated Poisson noise transforms into regular Poisson pulses kicking the system away from its equilibrium along the direction specified by the noise modulation phase. For sufficiently weak pulses, the resonator probability distribution, when being observed from different directions dictated by the phase between the resonator in-phase and quadrature components, resembles essential (singular) features of the linear system in a static potential driven by Poisson noise only, see [9]. The main contribution of the present study lies in our ability to control both the direction of the Poisson pulses in the rotating frame as well as the observation phase, which allows us to study aspects of the resonator probability density function that cannot be

observed in the system analyzed by Ichiki et al. Furthermore, we also investigate the effects of weak thermal noise on the resonator probability density function, which becomes smoothened by thermal noise in the vicinity of the singular peaks. From the application point of view, the model considered in this work can be directly applied to the analysis of mesoscopic vibrational systems with direct frequency noise of Poisson type. In this case, however, the direction of the Poisson pulses in the rotating frame is predetermined by the location of the system stable state, but the resonator noise-induced dynamics can still be analyzed from different observation directions.

The remaining part of the chapter is organized as follows. In Section 2.1 we describe the micromechanical resonator under study in experimental work performed by our collaborators in H. B. Chan's group at the Hong Kong University of Science and Technology, and provide the corresponding resonator model. Next, we discuss the qualitative picture of the resonator dynamics in the rotating frame in the presence of Poisson and thermal noise sources in Section 2.2. In Section 2.3.1 we analyze the noise-induced stationary probability distribution in the overdamped regime and show that, in addition to the singularity at the stable state, the resonator probability density can exhibit a secondary singular peak at a finite distance from the system fixed point. The case of a weakly damped resonator is considered in Section 2.3.2, where we illustrate that in this case the resonator probability density function can exhibit, in addition to the main peak at the system fixed point, multiple singular peaks away from the stable state, which arise from the slow oscillatory nature of the response in the rotating frame. The effect of weak thermal noise on the resonator dynamics is also discussed for both the strongly and weakly damped regimes in Section 2.3.3. Finally, we provide some conclusions in Section 2.4.

2.1 Experimental setup and resonator dynamical model

2.1.1 Micromechanical torsional resonator

In this work measurements have been performed with a micromechanical torsional resonator (Fig. 2.1a) consisting of a movable, highly doped polysilicon plate (200 $\mu m \times 200$ $\mu m \times 3.5$ μm) suspended by two centrally placed torsional rods (4 $\mu m \times 36$ $\mu m \times 2$ μm). Beneath the plate, there are two fixed electrodes (200 $\mu m \times 100$ μm) on each side of the torsional springs. The 2 μm gap underneath the plate is created by etching away a sacrificial silicon oxide layer. Figure 2.1b shows a cross-sectional schematic of the device with actuation and measurement circuitry. The effective spring constant is modulated electrostatically by a periodic voltage V_ω at frequency ω near twice the natural frequency ($\omega_0/2\pi \sim 20$ kHz) riding on top of a much larger bias voltage V_{DC}, which is necessary for efficient readout.

The resonator motion is detected capacitively. Periodic carrier voltages V_c at frequency ω_c of 5 MHz with opposite phases are applied to the two bottom electrodes. As the plate rotates, the capacitance between the plate and the bottom electrodes changes. A lock-in amplifier connected to the plate detects the charge flowing out and amplifies it. In this case, the rotation angle θ is proportional to the amplitude of the carrier voltage at ω_c at the output of the amplifier. Vibration of the plate is detected by measuring this output with the amplifier referenced at the sideband frequency $\omega_c + \omega/2$. Alternatively, the reference of the lock-in can be set at ω_c, with its output measured by a second lock-in referenced at $\omega/2$. Both methods yield the quadratures X and Y of the oscillations of the plate rotation angle

$$\theta(t) = C[X\cos(\omega t/2) + Y\sin(\omega t/2)] \tag{2.1}$$

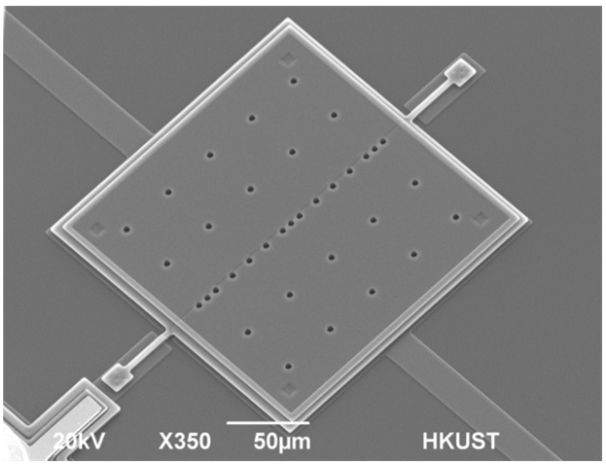

(a) Scanning electron micrograph of the micromechanical torsional oscillator used in the experiment.

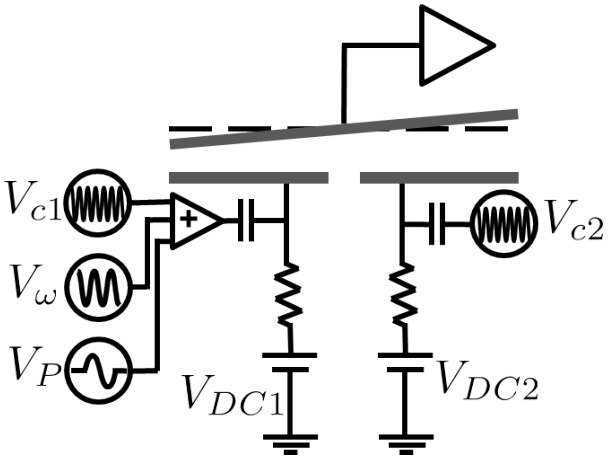

(b) Schematic of the device actuation and readout circuitry (not to scale).

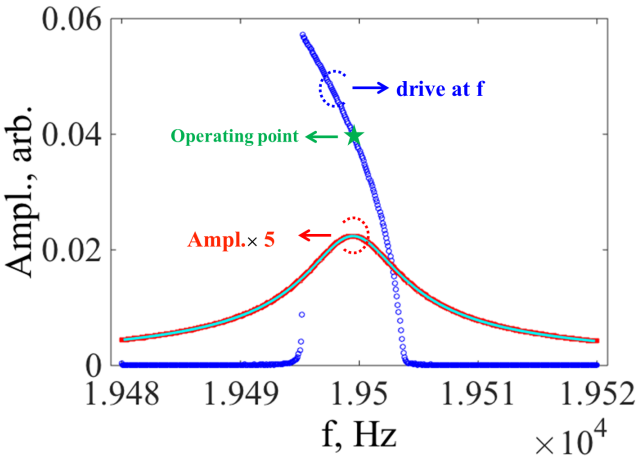

(c) Representative frequency responses of the resonator driven directly (the red curve) and parametrically (the blue curve). The green star indicates the location of the device operating point in the experiment.

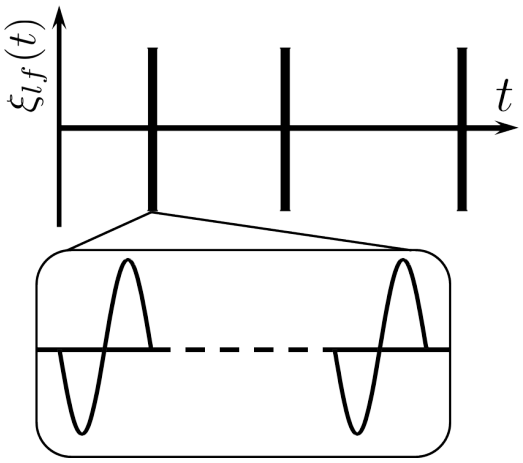

(d) Modulated Poisson pulses $\xi_{lf}(t)$. The duration of each pulse is much shorter than the inverse of the mean pulse rate ν, which allows us to approximate Poisson pulses as Dirac delta-functions on the resonator decay time scale, Γ^{-1}.

Figure 2.1: Micromechanical torsional resonator under study and experimental setup.

at $\omega/2$ frequency. Measurements have been performed at room temperature ($T = 300K$) with pressure of less than 10^{-6} torr.

The dynamic response of the torsional resonator under study can be modeled by the

following equation of motion,

$$\ddot{\theta} + 2\Gamma\dot{\theta} + (\omega_0^2 + h\cos\omega t)\theta + \gamma\theta^3 = \xi_{\rm lf}(t) + f(t), \tag{2.2}$$

where ω_0 is the resonator eigenfrequency (including mechanical and electrostatic components), $\Gamma = 24.7$ rad/s is the resonator decay rate in the laboratory reference frame, $\gamma = -6.30 \times 10^{11}$ s^{-2} is the coefficient of the cubic stiffness (Duffing) nonlinearity (of which the electrostatic component related to the dependence of the device capacitance on the plate angular displacement is dominant in this device), h represents the modulation amplitude of the effective spring constant, $\xi_{\rm lf}(t)$ is the modulated Poisson noise (subscript "lf" stands for the laboratory frame) and $f(t)$ is a weak thermal noise with the following statistics

$$\langle f(t)\rangle = 0, \quad \langle f(t)f(t')\rangle = D\delta(t-t'). \tag{2.3}$$

The intensity D of thermal noise $f(t)$ is related to the ambient temperature by the fluctuation-dissipation theorem $D = 4k_BT\Gamma/I$, where I is the resonator moment of inertia about its axis of rotation. With no noise, when the spring modulation amplitude is below the critical threshold, only the zero-amplitude resonator response is stable. When the modulation is increased beyond the threshold value [65], two stable oscillation states emerge, which have the same oscillation frequency ($\omega/2$) and amplitude but are phase shifted by π radians, which corresponds to a classical parametric resonance, see Fig. 2.1c.

The form of the modulated Poisson pulses $\xi_{\rm lf}(t)$ is shown in Fig. 2.1d. In order to generate such a noise signal we connect the output of a Gaussian noise voltage generator to the trigger input of a pulse generator. Whenever the noise voltage, in a rare large outburst, exceeds a

threshold value, the generator produces a square pulse. The threshold is chosen much larger than the mean-square noise amplitude. Respectively, the duration of the pulse ($t_p = 2\ ms$) is much smaller than the reciprocal pulse rate, ν^{-1}, which allows us to approximate the pulses as delta functions in the rotating frame in our analysis, i.e.

$$\xi(t) = g \sum_j \delta(t - t_j), \tag{2.4}$$

where g is the pulse area representing the strength of Poisson noise. The statistics of the pulses is Poissonian in this case. To exploit the high sensitivity of the resonator at frequencies close to ω_0, we modulate the Poisson pulses $\xi(t)$ at half of the spring modulation frequency to obtain

$$\xi_{\rm lf}(t) = \xi(t) \cos(\omega t/2 + \phi_p), \tag{2.5}$$

where ϕ_p represents the phase of the pulse modulation. As we will show below, ϕ_p plays an important role in studying the resonator noise-induces dynamics as it determines the direction of Poisson kicks in the resonator rotating frame.

2.1.2 Resonator model in the rotating frame

The resonator dynamics can be well characterized by two slow dimensionless variables, the scaled in-phase and quadrature components X and Y of the resonator rotation angle, defined as follows,

$$\theta = C(X \cos(\omega t/2) + Y \sin(\omega t/2)), \quad \dot{\theta} = -C\frac{\omega}{2}(X \cos(\omega t/2) + Y \sin(\omega t/2)), \tag{2.6}$$

where $C = \sqrt{2h/(3|\gamma|)}$ is the scaling factor. By scaling the time as $\tau = \Gamma t$ in Eq. (2.2), we obtain the following equation of motion for X and Y coordinates,

$$\dot{\boldsymbol{q}} = \boldsymbol{G}(\boldsymbol{q}) + \boldsymbol{l}_p \xi(\tau) + \boldsymbol{f}(\tau), \tag{2.7}$$

where $\boldsymbol{q} = (X, Y)$ is the vector consisting of the resonator in-phase and out-of-phase quadratures, respectively. Deterministic nonlinear vector field $\boldsymbol{G}(\boldsymbol{q})$ reads

$$\boldsymbol{G}(\boldsymbol{q}) = \begin{pmatrix} -X - \Delta\Omega Y - \alpha Y(2 - (X^2 + Y^2)\mathrm{sgn}(\gamma)) \\ -Y + \Delta\Omega X - \alpha X(2 + (X^2 + Y^2)\mathrm{sgn}(\gamma)) \end{pmatrix}, \tag{2.8}$$

where

$$\Delta\Omega = \frac{\omega - 2\omega_0}{2\Gamma}, \tag{2.9a}$$

$$\alpha = \frac{h}{4\omega\Gamma}, \tag{2.9b}$$

$$\mathrm{sgn}(\gamma) = \frac{\gamma}{|\gamma|}. \tag{2.9c}$$

In Eq. (2.7), $\xi(\tau)$ represents the demodulated and scaled Poisson pulses kicking the system in the rotating frame along the direction $\boldsymbol{l}_p = (\sin\phi_p, \cos\phi_p)$ determined by the modulation phase ϕ_p. The mean pulse rate and pulse area in the rotating frame are

$$\nu' = \frac{\nu}{\Gamma}, \tag{2.10a}$$

$$g' = g\sqrt{\frac{3|\gamma|}{2h\omega^2}}, \tag{2.10b}$$

respectively. Finally, $\boldsymbol{f}(\tau) = (f_X(\tau), f_Y(\tau))$ is the Gaussian noise vector acting on the resonator quadratures. As detailed in [49], the components of $\boldsymbol{f}(\tau)$ are two independent delta-correlated white noises of equal intensity

$$D' = \frac{3|\gamma|D}{h\omega^2\Gamma}. \tag{2.11}$$

Since the main goal of this work is to analyze the resonator probability distribution due to the presence of modulated Poisson pulses, we shall assume for now that thermal noise is not present in the system, i.e., $\boldsymbol{f}(\tau) = 0$. However, we will return to the discussion of the thermal noise effect on the probability density function in Section 2.3.3. In this light, in the absence of the Poisson noise, $\xi(\tau) = 0$, the stationary solution $\boldsymbol{q}_0$ to Eq. (2.7) satisfies $\boldsymbol{G}(\boldsymbol{q}_0) = \boldsymbol{0}$. If the Poisson pulses are weak, then in order to capture their effect on the resonator dynamics in the vicinity of its stable state, we can linearize $\boldsymbol{G}(\boldsymbol{q})$ about $\boldsymbol{q}_0$ and write the noise-induced resonator response in terms of the fundamental matrix $\boldsymbol{\Phi}(\tau)$, an analog of the integrating factor for systems of differential equations [66], as follows

$$\boldsymbol{q}(\tau) = \boldsymbol{\Phi}(\tau) \int_{-\infty}^{\tau} d\tau' \boldsymbol{\Phi}^{-1}(\tau') \boldsymbol{l}_p \xi(\tau'). \tag{2.12}$$

The joint probability distribution of the resonator quadratures X and Y can be described using the standard kinetic equation [64]

$$\partial_t \rho(\boldsymbol{q}, t) = - \bigtriangledown \cdot \big[\boldsymbol{G}(\boldsymbol{q})\rho(\boldsymbol{q}, t)\big] + \nu' \big[\rho(\boldsymbol{q} - \boldsymbol{l}_p g', t) - \rho(\boldsymbol{q}, t)\big], \tag{2.13}$$

which describes the temporal evolution of the system probability density and is useful for studying the escape dynamics of the system out of its metastable states. In this work,

however, we study the Poisson noise induced dynamics of the periodically driven resonator by analyzing the projection of the stationary probability distribution $\rho(\boldsymbol{q})$ onto a selected observation direction, which is described from a qualitative point of view in Section 2.2. We then proceed to the formal derivation of the resonator probability distribution along the chosen resonator phase in Section 2.3, where we follow closely with the method utilized by Ichiki et al. [9], but outline important differences of our approach along the discussion.

2.2 Qualitative picture of resonator fluctuations

The behavior of the probability distribution can be understood using a qualitative picture of the resonator response to an isolated Poisson pulse in the rotating frame. Under transformation from the laboratory coordinates to the rotating frame, the modulated Poisson pulses are converted into regular pulses that kick the system out of its equilibrium position in the direction dictated by the modulation phase ϕ_p, as depicted in Figs. 2.2a and 2.2b. In the experiment, the resonator motion is very lightly damped in the laboratory reference frame, $\omega_0 \gg \Gamma$, and the system quality factor $Q \sim 2500$. However, its dynamics in the rotating frame of X and Y quadratures can be either overdamped or underdamped, depending on the modulation frequency and amplitude. In the overdamped (underdamped) case, the noise-free impulse response is non-oscillatory (oscillatory) in the quadrature space; see Figs. 2.2a and 2.2b, respectively. The overdamped regime occurs when the eigenvalues $\lambda_{1,2}$ of the Jacobian $\partial \boldsymbol{G}/\partial \boldsymbol{q}|_{\boldsymbol{q}_0}$ in Eq. (2.7) are real; otherwise, the system is underdamped.

Let us define $q_m(\tau)$ as the system response $\boldsymbol{q}(\tau)$ projected onto the direction $\boldsymbol{l}_m =$

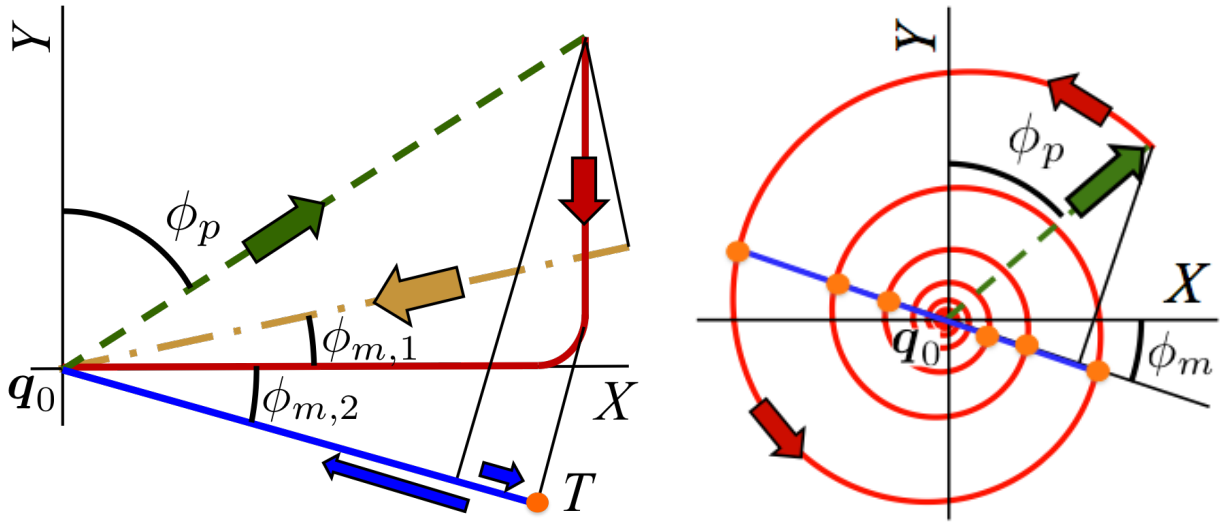

(a) Resonator relaxation in the rotating frame in the overdamped regime due to a single Poisson pulse.

(b) Resonator relaxation in the rotating frame in the underdamped regime due to a single Poisson pulse.

Figure 2.2: Schematic of the resonator response to a single Poisson pulse excitation in the rotating frame in overdamped (a) and underdamped (b) regimes. For panel (a) we have assumed, for simplicity, that the system is in strongly overdamped regime, i.e. $|\lambda_1| \ll |\lambda_2|$, with the corresponding eigenvectors coinciding with the X and Y directions.

$(\cos\phi_m, \sin\phi_m)$ at angle ϕ_m relative to the resonator in-phase component X,

$$q_m(\tau) = \boldsymbol{l}_m^T \boldsymbol{q}(\tau) = X(\tau)\cos\phi_m + Y(\tau)\sin\phi_m. \tag{2.14}$$

When the pulse rate ν' is small compared to the resonator decay rate in the rotating frame, determined by $\min(|\lambda_1|, |\lambda_2|)$, the system relaxes back to nearly its equilibrium position $\boldsymbol{q}_0$ before the next pulse arrives, leading to an accumulation of the probability distribution at $q_m = 0$. In the overdamped regime, there is no overshoot as the system relaxes towards the equilibrium point, see Fig. 2.2a, and the system does not access the quadrature space in directions opposite to the pulse direction, i.e., the directions where $\boldsymbol{l}_m^T \boldsymbol{l}_p < 0$. As a result, $\rho(q_m) = 0$ for $q_m < 0$ (in the absence of thermal noise) and the peak in the probability distribution at the equilibrium point is strongly asymmetric.

Away from the main peak at the equilibrium point, the shape of the probability distribution strongly depends on the modulation phase ϕ_p and the phase of the measurement direction ϕ_m. Depending on the value of ϕ_m, the system relaxation to its stationary state can be generally viewed as monotonic (non-monotonic), see $\phi_{m,1}$ ($\phi_{m,2}$) in Fig. 2.2a, respectively. In the latter case, the system relaxation along $\boldsymbol{l}_m$ has a turning point T where $\dot{q}_m = 0$ and the resonator motion, as viewed from $\boldsymbol{l}_m$, slows down. While the resonator relaxation slows down, the system necessarily spends more time in the vicinity of the turning point, which, in turn, leads to an accumulation of the probability density and results in an additional sharp peak in the distribution at a finite q_m. In contrast, when the resonator relaxation along $\boldsymbol{l}_m$ is monotonic, the probability distribution is also monotonic and smooth away from the resonator equilibrium. Note, however, that if $\boldsymbol{l}_p$ coincides with either of the system eigenvectors, the resonator relaxes back to $\boldsymbol{q}_0$ along the same direction. In this case, independently of the observation direction we choose, the resonator trajectory towards its equilibrium will be seen as monotonic relaxation and the secondary peak will not emerge.

In the underdamped regime, the relaxation path towards the equilibrium point in the quadrature space is a spiral, as shown in Fig. 2.2b. In this case, for sufficiently rare pulses, the system has access to both positive and negative values of q_m, regardless of the choice of $\boldsymbol{l}_m$, and the peak at the equilibrium point is almost symmetric in strongly underdamped regime. Additionally, as the system relaxes back towards $\boldsymbol{q}_0$, it passes through multiple turning points T_i, at which $\dot{q}_m = 0$, with positions that depend on the mutual orientation of $\boldsymbol{l}_p$ and $\boldsymbol{l}_m$. As in the overdamped regime, the system spends more time near these points and additional peaks in the probability distribution occur. Importantly, if the Poisson pulses are sufficiently weak so that the linearization of Eq. (2.7) about $\boldsymbol{q}_0$ holds, these secondary peaks result in a self-similar structure of the resonator probability distribution. If, however,

the Poisson pulses are sufficiently strong so that full system in Eq. (2.7) must be considered, the structure of the probability distribution beyond the linear limit is no longer self-similar, due to an amplitude-dependent frequency shift along the spiral towards $\boldsymbol{q}_0$.

2.3 Resonator stationary probability distribution in the rotating frame

2.3.1 Overdamped regime

We study the probability distribution in the rotating frame in the strongly overdamped regime by applying a periodic modulation slightly below the threshold value , i.e., $\alpha \lessapprox 1$, so that the only stable state is the zero-amplitude solution. In this case we have, without loss of generality,

$$\epsilon = |\lambda_1| \ll |\lambda_2| \approx 2, \quad \epsilon \ll 1. \tag{2.15}$$

For the Poisson noise applied, the phase of modulation ϕ_p was initially chosen so that each pulse produces a translation in the quadrature space along the slow eigendirection; in measuring the vibration, ϕ_m was also chosen to lie along this direction. This choice of ϕ_p and ϕ_m is very convenient for studying the resonator probability distribution in the vicinity of $\boldsymbol{q}_0$ because the system motion in the rotating plane is essentially restricted along the slow eigendirection. Figure 2.3a shows a typical record of q_m as a function of time in this case. As the resonator relaxes towards the equilibrium point, the subsequent pulses arrive at random instants of time to produce further jumps. To obtain the probability distribution $\rho(q_m)$, the q_m axis is divided into bins and the time spent by the resonator in each bin is measured.

In order to derive the resonator stationary probability distribution along $\boldsymbol{l}_m$, we start

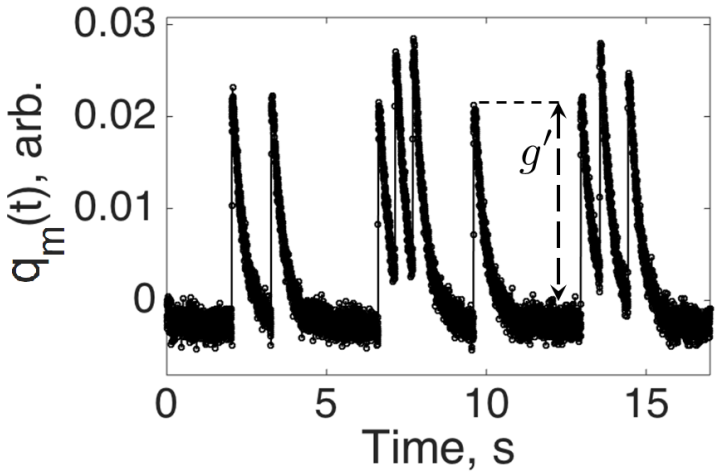

(a) Sample of the real-time response of the resonator quadrature along the system slow eigendirection in the overdamped regime. The Poisson mean pulse rate is $\nu = 0.52$ Hz.

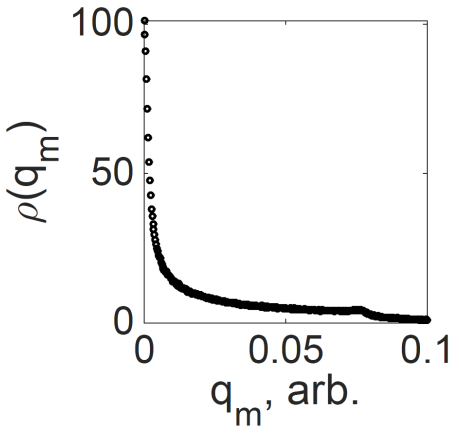

(b) Probability distribution $\rho(q_m)$ of the resonator quadrature along the system slow eigendirection.

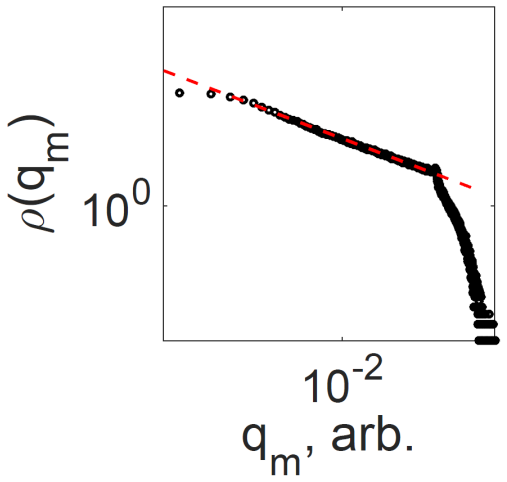

(c) Probability distribution $\rho(q_m)$ of the resonator quadrature along the system slow eigendirection shown on a logarithmic scale. The dashed line represents the least-squares fit of the power-law behavior of the probability distribution in the vicinity of $q_m = 0$.

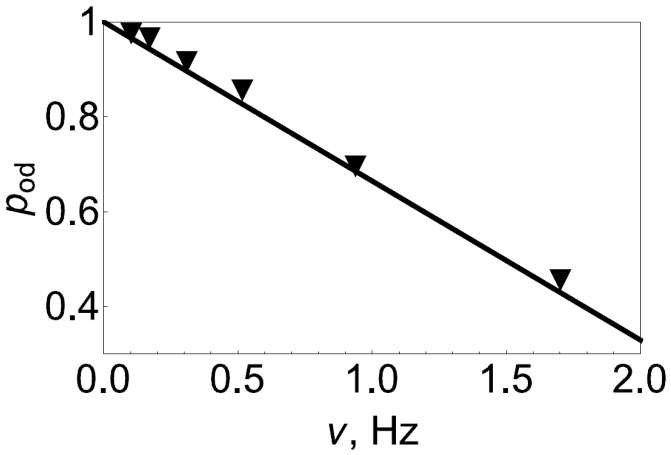

(d) Power-law exponent of $\rho(q_m)$ in the overdamped regime for different values of the Poisson mean pulse rate ν. The solid line and triangles represent the theoretical prediction and experimentally extracted values of p_{od}, respectively.

Figure 2.3: Poisson noise-induced resonator dynamics in the rotating frame in the overdamped regime.

with its conventional form

$$\rho(q_m) = \langle \delta(q_m - q_m(0)) \rangle, \tag{2.16}$$

see [67]. From Eqs. (2.12) and (2.14) we have

$$q_m(\tau) = \int_{-\infty}^{\tau} d\tau' \eta_\xi(\tau - \tau')\xi(\tau'), \tag{2.17a}$$

$$\eta_\xi(\tau - \tau') = \boldsymbol{l}_m^T \boldsymbol{\Phi}(\tau)\boldsymbol{\Phi}^{-1}(\tau')\boldsymbol{l}_p, \tag{2.17b}$$

where $\eta_\xi(\tau)$ is the resonator susceptibility along $\boldsymbol{l}_m$ to Poisson pulses along $\boldsymbol{l}_p$ in the quadrature space. This form of $q_m(\tau)$ further yields

$$q_m(0) = \int_{-\infty}^{0} d\tau' \eta_\xi(-\tau')\xi(\tau') = \int_0^{\infty} ds \eta_\xi(s)\xi(-s), \tag{2.18}$$

where we have introduced new time variable $s = -\tau'$ and flipped the limits of integration. In this light, the resonator probability distributions $\rho(q_m)$ becomes

$$\rho(q_m) = \langle \delta(q_m - q_m(0)) \rangle = \int_{-\infty}^{\infty} \frac{dk}{2\pi} e^{-ikq_m} \left\langle e^{ikq_m(0)} \right\rangle_\xi, \tag{2.19}$$

where $\langle\rangle_\xi$ denotes statistical averaging over different Poisson noise realizations. Given that $\xi(\tau') = g' \sum_j \delta(\tau' - \tau_j')$ and $\tau_j' < 0$ in Eq. (2.18), we have

$$\left\langle e^{ikq_m(0)} \right\rangle_\xi = \left\langle \exp\left[ikg' \sum_j \int_0^{\infty} ds \eta_\xi(s)\delta(s - s_j) \right] \right\rangle_\xi, \tag{2.20}$$

where $s_j = -\tau_j' > 0$. The expression on the right-hand side in Eq. (2.20) represents the characteristic functional for the series of Poisson pulses [68]. Accordingly, we derive the

general form of the resonator probability density function $\rho(q_m)$, which reads

$$\begin{aligned}\rho(q_m) &= \int_{-\infty}^{\infty} \frac{dk}{2\pi} e^{-ikq_m} \exp\Big[-\nu' \psi(k) \Big], \\ \psi(k) &= \int_0^{\infty} d\tau \Big[1 - e^{ikg' \eta_\xi(\tau)} \Big],\end{aligned} \tag{2.21}$$

In the overdamped regime, the resonator susceptibility can be expressed in the following form

$$\eta_\xi(\tau) = \eta_\xi^{(od)}(\tau) = c_1 \exp[-\epsilon\tau] + c_2 \exp[-2\tau], \tag{2.22}$$

where c_i are constants that depend on ϕ_p, ϕ_m, and the orientation of the system eigendirections. As we mentioned above, in this case there is no overshoot in the relaxation, which yields $\rho(q_m) = 0$ for $q_m < 0$. Since in strongly overdamped regime $|\lambda_1| \ll |\lambda_2|$, the second term in Eq. (2.22) decays much faster than the first one, $\propto \exp[-\epsilon\tau]$, and the resonator susceptibility can be approximated as

$$\eta_\xi^{(od)}(\tau) \approx c_1 \exp[-\epsilon\tau], \quad \text{for} \quad \tau > 1. \tag{2.23}$$

As a result, the leading-order contribution to $\psi_{od}(k)$ in Eq. (2.21) comes from the interval $\tau > 1$. By denoting this contribution as $\psi_{od}^{(0)}(k)$, we have

$$\begin{aligned}\psi_{od}^{(0)}(k) &= \int_1^{\infty} d\tau \Big[1 - e^{ikg' c_1 \exp[-\epsilon\tau]} \Big] \\ &= \int_1^{\infty} d\tau \Big[1 - \cos\Big(c_1 k g' e^{-\epsilon\tau} \Big) - i \sin\Big(c_1 k g' e^{-\epsilon\tau} \Big) \Big].\end{aligned} \tag{2.24}$$

In order to compute the last integral, we introduce a new variable $z = c_1 k g' \exp[-\epsilon\tau]$. After

some algebra, $\psi_0(k)$ becomes

$$\begin{aligned}\psi_{od}^{(0)}(k) &= \epsilon^{-1}\int_0^{c_1 kg'} dz \frac{1-\cos z - i\sin z}{z} \\ &= \epsilon^{-1}\big[\ln(c_1 kg') - \mathrm{Ci}(c_1 kg') - i\mathrm{Si}(c_1 kg') + \gamma_E\big],\end{aligned} \tag{2.25}$$

where Ci() and Si() are the cosine and sine integral functions, see [69], and γ_E is the Euler-Mascheroni constant. The resonator probability distribution $\rho(q_m)$ in the vicinity of the stable state is primarily determined by the large$-k$ behavior of $\psi_{od}^{(0)}(k)$ in Eq. (2.21), while the small$-k$ piece of $\psi_{od}^{(0)}(k)$ describes the smooth part of $\rho(q_m)$. In particular, for large k cosing and sine integral functions can be approximated by their asymptotic expansions and we have

$$\psi_{od}^{(0)}(k) \approx \epsilon^{-1}\left[\ln c_1 kg' + i(c_1 kg')^{-1} e^{ic_1 kg'} - i\frac{\pi}{2} + \gamma_E\right]. \tag{2.26}$$

By substituting this expression in Eq. (2.21), we obtain that $\psi_{od}^{(0)}(k)$ leads to the power-law behavior of $\rho(q_m)$ near the origin,

$$\begin{aligned}\rho(q_m) &\approx \int_{-\infty}^{\infty}\frac{dk}{2\pi} e^{-ikq_m}(c_1 kg')^{-\nu'/\epsilon}\exp\left[-\frac{\nu'}{\epsilon}\left(\gamma_E - i\frac{\pi}{2}\right)\right] \propto q_m^{-p_{od}}, \\ p_{od} &= 1 - \frac{\nu'}{\epsilon},\end{aligned} \tag{2.27}$$

where p_{od} is the power-law exponent of the resonator probability distribution in the vicinity of the stable state. This power-law exponent is determined by the ratio of ν' to the decay rate ϵ along the slow direction of the response in the rotating frame. For sufficiently low pulse rates, $\nu' < \epsilon$, the exponent is positive and the probability distribution diverges at the origin. As we shall discuss in Section 2.3.3, the presence of thermal noise regularizes this singular distribution.

Figure 2.3b shows the measured probability distribution in the overdamped regime, which is in qualitative agreement with the theoretical analysis. Figure 2.3c shows the same data plotted on a semi-logarithmic scale, with the linear fit yielding the measured power-law exponent of the probability distribution in the vicinity of the origin. Figures 2.3b and 2.3c are derived from the record of q_m over 30 minutes. Figure 2.3d shows the measured exponent (triangles) as a function of the Poisson pulse rate, along with the theoretical prediction (solid line) which uses no fitting parameters, demonstrating excellent agreement between measurement and theory.

In addition to the behavior close to the origin described above, there are additional interesting features of the resonator probability density function for $q_m \neq 0$. These features are due to the small contribution to $\psi_{od}(k)$ coming from the time interval $\tau \in [0, 1]$. In this case, the integral in Eq. (2.21) can be approximated for large k by employing the method of stationary phase. Depending on the phase ϕ_m of the measurement quadrature in the rotating frame, $\eta_\xi(\tau)$ can be monotonic, $c_1 c_2 > 0$, or non-monotonic, $c_1 c_2 < 0$. When $\eta(\tau)$ is a monotonic function of τ, there is no stationary point, i.e., $\dot{\eta}(\tau) \neq 0$ for all τ, and we have

$$\begin{aligned} \psi_{od}^{(1)}(k) &= \int_0^1 d\tau \left[1 - e^{ikg'\eta_\xi(\tau)}\right] \sim 1 - \frac{\exp[ikg'\eta_\xi(\tau)]}{ikg'\eta_\xi'(\tau)}\Big|_0^1 \\ &\approx 1 - \frac{i\exp[ic_1 kg']}{\epsilon c_1 kg'} + \frac{i\exp[i(c_1+c_2)kg']}{kg'(\epsilon c_1 + 2c_2)}, \end{aligned} \tag{2.28}$$

where the second term cancels the exponential term in $\psi_{od}^{(0)}(k)$. As it follows from Eqs. (2.26) and (2.28), $\psi_{od}^{(1)}(k)$ is $O(\epsilon)$ as compared with $\psi_{od}^{(0)}(k)$, which allows us write the resonator

probability distribution and corresponding correction due to $\psi_{od}^{(1)}(k)$ as

$$\rho(q_m) \approx \int_{-\infty}^{\infty} \frac{dk}{2\pi} e^{-ikq_m} \exp\left[-\nu' \psi_{od}^{(0)}(k) \right] \left(1 - \nu' - \nu' \frac{i \exp[i(c_1+c_2)kg']}{kg'(\epsilon c_1 + 2c_2)} \right), \tag{2.29a}$$

$$\delta\rho(q_m) \approx -\nu' \int_{-\infty}^{\infty} \frac{dk}{2\pi} e^{-ikq_m} \exp\left[-\nu' \psi_{od}^{(0)}(k) \right] \frac{i \exp[i(c_1+c_2)kg']}{kg'(\epsilon c_1 + 2c_2)}. \tag{2.29b}$$

As a result, the correction to $\psi_{od}(k)$, being taken into account in Eq. (2.21), yields an additional peak in $\rho(q_m)$ with the shape described by

$$\begin{gathered} \delta\rho(q_m) \propto |q_m - q_2|^{-p_{od}+1}, \\ q_2 = (c_1 + c_2)g' \end{gathered} \tag{2.30}$$

From Eq. (2.29b) it follows that this peak is asymmetric, since the prefactor depends on the sign of $q_m - q_2$. Remarkably, $\rho(q_m)$ does not diverge at $q_m = q_2$ since $p_{od} < 1$ for all values of the pulse rate, even though the divergence can still be seen in $\partial_{q_m}\rho$ for sufficiently small ν. Figure 2.4a shows a typical form of the resonator probability distribution when the observation direction is chosen such that the resonator susceptibility $\eta_\xi(\tau)$ is monotonic.

If, however, we choose the observation direction such that $\eta_\xi(\tau)$ is non-monotonic, there is a stationary point τ_T in the resonator susceptibility where $\dot{\eta}_\xi(\tau_T) = 0$. Physically, this stationary point corresponds to the turning point in the resonator relaxation path as seen from the observation direction, see Fig. 2.2a. In this case the result for $\psi_{od}^{(1)}(k)$ is similar to that obtained in [9] and reads

$$\psi_{od}^{(1)}(k) \sim 1 - \sqrt{\frac{\pi}{4\epsilon c_1 kg'}} \exp\left[ic_1 kg' - \mathrm{sgn(c_1)} \frac{\pi}{4} \right], \tag{2.31}$$

where sgn() denotes the sign of the quantity in the brackets. Following the same line of

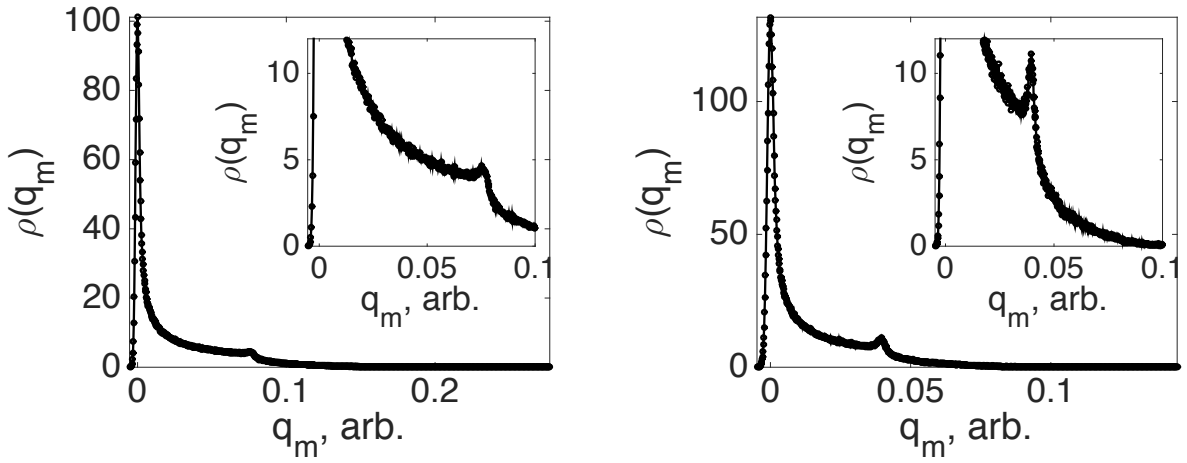

(a) Reduced peak due to monotonic response function, for $c_1 = 0.99, c_2 = 0.1$.

(b) Sharp peak due to non-monotonic response function, for $c_1 = \sqrt{3}/2, c_2 = -1/2$.

Figure 2.4: Measured probability distribution $\rho(q_m)$ in the rotating frame due to Poisson pulses along the out-of-phase quadrature with $\nu = 0.94$ Hz and thermal noise at $T = 300$K in the overdamped regime. In contrast to the data shown in Fig. 2.2a, the resonator eigendirections in the experiment are $(1, \pm(\alpha - \Omega))$ in (X, Y) space and are not aligned with either the in-phase or out-of-phase resonator components. The latter fact allows us to observe singular or flat peak structures of the resonator probability distribution at a finite distance from the origin by changing the observation direction.

thoughts that led us to Eq. (2.29b), it becomes clear that the correction to the probability distribution due to $\psi^{(1)}_{od}(k)$ defined in Eq. (2.31) results in an additional peak in the resonator probability distribution. In particular, we have

$$\begin{aligned}\delta\rho(q_m) &\approx \nu' \int_{-\infty}^{\infty} \frac{dk}{2\pi} e^{-ikq_m} \exp\left[-\nu' \psi^{(0)}_{od}(k) \right] \sqrt{\frac{\pi}{4\epsilon c_1 k g'}} e^{ic_1 k g' - \mathrm{sgn}(c_1)\pi/4} \\ &\propto |q_m - c_1 k g'|^{-p_{od}+1/2}.\end{aligned} \tag{2.32}$$

where p_{od} is defined in Eq. (2.27). In this situation, the probability distribution displays singular behavior away from the origin for pulse rates for which $p_{od} > 1/2$; otherwise, the probability distribution has flat peak, while $\partial_q \rho$ still can display divergence. Figure 2.4b illustrates the singular behavior of the resonator probability distribution in the case when the resonator susceptibility $\eta_\xi(\tau)$ is non-monotonic function of time.

2.3.2 Underdamped regime

It turns out that we can also derive the general form of the resonator probability distribution when the resonator is driven far from the sub-critical bifurcation and where the system behavior in the rotating frame is strongly underdamped. The analysis corresponding to this case of the resonator dynamics is essentially identical to the case of the underdamped linear resonator in a static potential [9], so here we highlight the main results. In particular, in the underdamped regime the resonator eigenvalues are complex,

$$\lambda_{1,2} = -\lambda_r \pm i\lambda_i, \quad \lambda_i \gg \lambda_r > 0, \tag{2.33}$$

where λ_r dictates the resonator relaxation rate in the rotating frame, while λ_i determines the system angular frequency of its spiral motion towards equilibrium. As a result, the resonator susceptibility along chosen observation direction has the following form,

$$\eta_{\xi}^{(ud)}(\tau) = c_3 e^{-\lambda_r \tau} \sin(\lambda_i \tau + \beta), \tag{2.34}$$

where c_3 and β are constants that depend, as before, on the modulation phase of the Poisson pulses ϕ_p, observation direction $\boldsymbol{l}_m$, and the resonator parameters. Figure 2.5a shows a typical trajectory of the system in the quadrature space in response to a single Poisson pulse. Unlike in the overdamped case, the system spirals toward the equilibrium point and spends time in the $q_m < 0$ region regardless of our choice of ϕ_m. As a result, in the underdamped regime, $\rho(q_m) \neq 0$ for $q_m < 0$ and the shape of the probability distribution is nearly symmetric with respect to the stationary state. First, we study the resonator

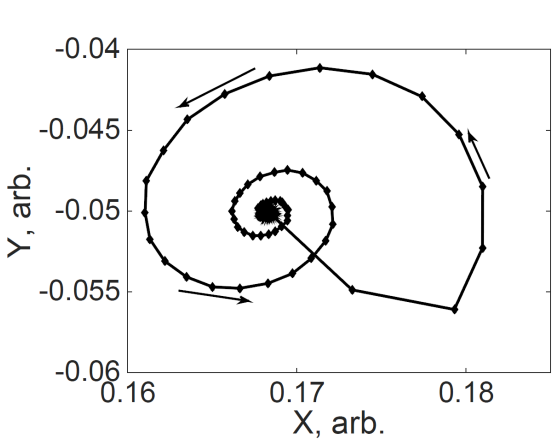

(a) Sample of the real-time response of the resonator to a single Poisson pulse in the underdamped regime in the rotating frame.

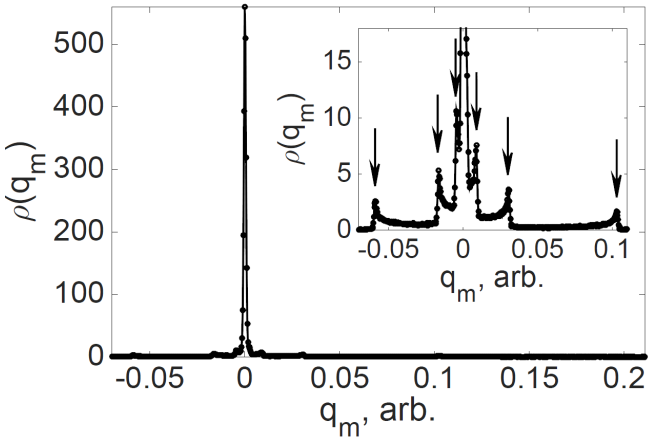

(b) Measured probability distribution $\rho(q_m)$ projected onto $\boldsymbol{l}_p$ in the underdamped regime due to Poisson pulses with $\nu = 4.92$ Hz and thermal noise at $T = 300$K. Inset: multiple peaks occur at positions predicted by $q_n = (-1)^n c_3 g' e^{-\lambda_r \tau_n}$.

Figure 2.5: The resonator dynamics and the associated probability distribution in the rotating frame in the underdamped regime.

distribution in the vicinity of stable state. Inserting $\eta_\xi^{(ud)}(\tau)$ into Eq. (2.21) yields,

$$\psi_{ud}(k) \approx \psi_{ud}^{(0)}(k) = \lambda_r^{-1} \int_0^{c_3 k g'} dz \frac{1 - J_0(z)}{z}, \tag{2.35}$$

where we have introduced a new variable,

$$z = c_3 k g' e^{-\lambda_r \tau}, \tag{2.36}$$

and used Jacobi-Anger expansion [69] of the term $\exp[iz \sin \lambda_i \tau]$ to the leading order because $z \to 0$ as $\tau \to \infty$. In Eq. (2.37) $J_0(z)$ is the zero-order Bessel function of the first kind. As we mentioned above, integration over the range of large k gives singular contribution to the

distribution $\rho(q_m)$. For large k, we can approximate $\psi_{ud}^{(0)}(k)$ as

$$\psi_{ud}^{(0)}(k) \approx \lambda_r^{-1}\left(\ln\frac{c_3 k g'}{2} + \gamma_E\right), \tag{2.37}$$

from where it follows that the probability distribution $\rho(q_m)$ also exhibits a power-law behavior in the vicinity of $q_m = 0$ in the underdamped case. In particular, we have

$$\begin{gathered}\rho(q_m) \approx \int_{-\infty}^{\infty}\frac{dk}{2\pi}e^{-ikq_m}\left(\frac{c_3 k g'}{2}\right)^{-\nu'/\lambda_r}\exp\left[-\frac{\nu'}{\lambda_r}\gamma_E\right] \propto |q_m|^{-p_{ud}}, \\ p_{ud} = 1 - \frac{\nu'}{\lambda_r}.\end{gathered} \tag{2.38}$$

The power-law exponent p_{ud} is defined, as before, by the ratio of the mean pulse rate to the relaxation rate of the system, λ_r, but the peak at the origin is now symmetric due to the underdamped nature of the resonator dynamics in the rotating frame.

In addition to the singularity at the origin, the probability distribution has multiple peaks at finite values of q_m due to the existence of multiple turning points T_n, as we discussed in Section 2.2. These turning points correspond to the stationary points of $\eta_\xi(\tau)$, i.e., where $\dot{\eta}_\xi = 0$. In the strongly underdamped case, $\lambda_r \ll \lambda_i$, these points are found to satisfy

$$\lambda_i \tau_n + \beta = \pi\left(n + \frac{1}{2}\right), \quad n = 0, 1, 2, \ldots. \tag{2.39}$$

In this case, by partitioning the integration range in Eq. (2.21) into multiple bins, each of which containing one τ_n, we can obtain the correction $\psi_{ud}^{(1)}(k)$ following the method of

stationary phase [70],

$$\psi_{ud}^{(1)}(k) \approx \lambda_r^{-1}\left(1 - \frac{\lambda_r}{\lambda_i}\sqrt{\frac{\pi}{2c_3 k g'}}\sum_{n=0}^{N} e^{\lambda_r \tau_n/2} e^{i\phi_n(k)}\right),$$
$$\phi_n(k) = (-1)^n\left(c_3 k g' e^{-\lambda_r \tau_n} - \frac{\pi}{4}\right), \tag{2.40}$$

where number N is chosen such that $c_3 k g' \exp[-\lambda_r \tau_N] = z_n \gg 1$. In this case, as it follows from Eq. (2.40), corrections to $\psi_{ud}(k)$ due to the presence of turning points $T_n \propto \lambda_r/\lambda_i$ and small in the strongly underdamped regime. As a result, the associated corrections to the resonator probability density function $\rho(q_m)$ become

$$\delta\rho_n(q_m) \approx -\frac{\nu'}{\lambda_i} e^{\lambda_r \tau_n/2}\int_{-\infty}^{\infty}\frac{dk}{2\pi} e^{-ikq_m}\exp\left[-\nu'\psi_{od}^{(0)}(k)\right] e^{i\phi_n(k)}$$
$$\propto |q_m - q_n|^{-p_{ud}+1/2}, \tag{2.41}$$

where locations q_n are defined as

$$q_n = (-1)^n c_3 g' e^{-\lambda_r \tau_n}. \tag{2.42}$$

As it follows from the from of $\delta\rho_n(q_m)$, the resonator probability distribution has multiple peaks away from the system fixed point; these peaks form a geometric progression and exhibit the same power-law behavior dictated by the ratio of the Poisson mean pulse rate to the resonator relaxation rate λ_r in the rotating frame. Importantly, when $p_{ud} > 1/2$, secondary peaks in the probability distributions are divergent; in the opposite scenario the divergence can only be seen in the derivative $\partial_{q_m}\rho$. Figure 2.5b shows the measured probability distribution $\rho(q_m)$, in which the positions of the peaks, as marked by the arrows, are in good agreement with theoretical predictions obtained by using Eq. (2.42).

2.3.3 Effects of thermal noise

The presence of weak thermal noise $f(t)$ affects the resonator probability distribution induced by the modulated Poisson pulses. In particular, $\boldsymbol{f}(\tau)$ contributes to the resonator motion $\boldsymbol{q}(\tau)$ in the rotating frame as follows,

$$\boldsymbol{q}(\tau) = \boldsymbol{q}_\xi(\tau) + \boldsymbol{\Phi}(\tau) \int_{-\infty}^{\tau} d\tau' \boldsymbol{\Phi}^{-1}(\tau') \boldsymbol{f}(\tau'), \tag{2.43}$$

where $\boldsymbol{q}_\xi(\tau)$ is Poisson noise-induced resonator response defined is Eq. (2.12). Consequently, we can rewrite the resonator response along chosen observation direction $q_m(\tau)$ as

$$q_m(0) = q_{m\xi}(0) + \int_0^\infty ds \eta_X(s) f_X(-s) + \int_0^\infty ds \eta_Y(s) f_Y(-s), \tag{2.44}$$

where f_X and f_Y are the components of thermal noise vector $\boldsymbol{f}(\tau)$ and η_X and η_Y are the corresponding susceptibilities of q_m to f_X and f_Y, respectively. Accounting for the statistical properties of f_X and f_Y, namely

$$\langle f_X(t_1) f_X(t_2) \rangle = \langle f_Y(t_1) f_Y(t_2) \rangle = D' \delta(t_1 - t_2), \quad \langle f_X(t_1) f_Y(t_2) \rangle = 0, \tag{2.45}$$

see [49], we can show, following the same line of thoughts as in Section 2.3.1, that the presence of thermal noise results in an additional exponential factor, [68], in Eq. (2.21),

$$\begin{aligned} \rho_{\xi,f}(q_m) &= \int \frac{dk}{2\pi} e^{-ikq_m} e^{-\nu' \psi(k)} \exp\left[-\frac{k^2 D' A}{2} \right], \\ A &= \int_0^\infty d\tau (\eta_X^2(\tau) + \eta_Y^2(\tau)), \end{aligned} \tag{2.46}$$

where $\rho_{\xi,f}(q_m)$ is the resonator probability distribution in the presence of both Poisson pulses and thermal noise. From Eq. (2.46) it follows that thermal noise, no matter how small, dominates the dynamics for large k, since $k^2 \gg \psi(k) \sim \ln k$ for $k \to \infty$, and thus we expect to see Gaussian behavior of the probability distribution in the vicinity of singular peaks located at the resonator stable state $q_m = 0$ and at the turning points $q_m = q_T$ along the system relaxation trajectory, both in the overdamped and underdamped regimes. Figures 2.4a, 2.4b and 2.5b show that thermal noise regularizes singular behavior of the probability density, and $\rho(q_m)$ has normal distribution in the vicinity of its maxima. Of course, thermal noise affects the resonator dynamics along the whole relaxation path. However, its effect on the resonator dynamics becomes more noticeable in the vicinity of points where the resonator relative velocity is small, and $\boldsymbol{f}(\tau)$ essentially "thermalizes" the resonator in the close proximity to singular (for rare Poisson pulses) peaks. For weak thermal noise, $\rho(q_m)$ quickly deviates from the normal distribution away from "singular" peaks. As we mentioned in Section 2.3.1, thermal noise also leads to a non-vanishing contribution to $\rho(q_m)$ for $q_m < 0$ when the resonator is in the overdamped regime. Physically, the only way the resonator can enter this region is due to thermal noise when $q_m \lesssim \sqrt{D'}$ and, thus, the probability distribution is normal in $q_m < 0$ region. In the underdamped regime, as it follows from Eq. (2.46), $\boldsymbol{f}(\tau)$ also distorts the singular behavior of the probability density and makes $\rho(q_m)$ finite for all ν over the entire range of q_m, which was confirmed in the experiment, see Fig. 2.5b.

The analytical approach developed in this chapter and experimental methods presented above allow one to study the dynamics of mesoscopic vibrational systems with eigenfrequency fluctuations having Poisson statistics. In this case, the analysis is quite similar to the one developed in Section 2.1, see Appendix A. However, the main difference between the model considered in this chapter and systems with multiplicative noise of Poisson type is in the fact

that, in the latter case, the modulation phase of Poisson pulses is essentially predetermined by the resonator fixed point in the rotating frame and, thus, is harder to manipulate in the experiment. However, one still can vary the observation direction and, thus, investigate singular features of the resonator probability distribution from different angles. Finally, it is worth noting that our methods are not limited to parametrically modulated resonators and can be similarly applied to directly excited resonant systems.

2.4 Outlook

As mentioned at the beginning of this chapter, this work was motivated by the necessity of a better fundamental understanding of the dynamic behavior of mesoscopic systems in the presence of Poisson noise. In this light, we have studied the probability distribution of the nonlinear torsional parametric resonator in the rotating frame. In addition to parametric forcing, the resonator was driven by modulated Poisson pulses and weak thermal noise. With the ability to tune the direction of Poisson pulses and choose the measurement quadrature in the rotating frame, we have shown that for sufficiently small pulse rates the probability distribution exhibits a power-law singularity near the resonator equilibrium both in the overdamped and underdamped regimes. Additionally, we have described the dependence of the corresponding exponent on the Poisson mean pulse rate and the system decay rate in the rotating frame. We also found additional peak(s) in the distribution away from the origin and specified their positions and the conditions for their appearance. In particular, we demonstrated that the probability distribution is strongly asymmetric in the overdamped regime, while in the underdamped regime it has a self-similar structure. Weak thermal noise affects the system by smoothening singular peaks in the probability distribution and making

the distribution Gaussian in the vicinity of these peaks. Our analytical results for power-law exponents near the peaks and for the positions of peaks in the probability distribution are in excellent agreement with experimental observations from the micromechanical resonator.

Chapter 3

Characterizing nonlinearities and noise in MEMS: ringdown-based approach

In this chapter we discuss a time-domain technique for complete characterization of nonlinear symmetric MEMS resonators whose response is governed by a single vibrational mode. The characterization method is based on the analysis of the transient response of the resonator when external forcing is absent, that is, on its so-called ringdown response. Our primary purpose is to find a way to extract model parameters associated with both deterministic and random properties of the resonator and the readout of its response. The deterministic parameters are associated with linear and nonlinear stiffness, linear and nonlinear damping, and the parameters for the random part of the model are the intensities of additive (thermal), multiplicative (frequency) and measurement noise sources. The fact that the dynamic behavior of the resonator vibration amplitude during the ringdown is independent of the shape of the resonator potential allows us to investigate its decay rate as a function of the instantaneous amplitude, thus, providing a way to estimate the resonator quality factor and the associated nonlinearity in the damping force. At the same time, the resonator vibration frequency in the ringdown follows the "backbone" curve, which entirely depends on the form

of the system potential energy. In this work we utilize the sequence of zero-crossing points in order to extract the resonator vibration frequency as a function of time, or, equivalently, amplitude, and estimate not only the linear natural frequency of the system, but also characterize the coefficients of higher-order terms (Duffing and quintic) in the resonator restoring force, thus allowing one to describe hardening, softening, and mixed types of conservative nonlinearities. Furthermore, a statistical analysis of the sequence of zero-crossing points allows us to separate the effects of measurement noise on the measured resonator response from resonator-related additive and multiplicative noise sources, and to estimate their relative strengths. We have tested this technique using simulated data, as well as ringdown responses of double-anchored double-ended-tuning-fork (DA-DETF) resonators that have been measured by our collaborators in Tom Kenny's group at Stanford University.

The primary motivation for this study is the fact that parameter estimation in vibrational systems is a challenging problem arising in systems of different size scales [45, 56, 71–73]. It is important since it allows one to describe the dynamics of systems of interest using standard models [74–76], to understand the fundamental physical mechanisms responsible for certain observed effects [77, 78], and to design systems with desired performance characteristics [79, 80]. While several methods have been developed for nonlinear system identification [81], a common approach for determining the model parameters of MEMS resonators is based on the resonant response of a vibrational mode to a periodic force. In this case, the resonator amplitude and phase are measured as a function of the frequency of the external driving field for a fixed level of the drive amplitude. For systems operating in the linear regime this spectral method provides estimates for the linear resonant frequency and the quality factor [82] from a frequency response. When the resonator is driven into its nonlinear regime, the shape of the frequency response is determined by both conservative [31]

and dissipative nonlinearities [32–34, 83]. As a result, it is necessary to perform several measurements at different forcing amplitudes in order to completely characterize the parameters of the vibrational mode [31, 82], and the precision is limited, particularly where several nonlinear mechanisms are involved.

Estimation of statistical parameters of the noise sources in nonlinear micromechanical resonators is also an important and challenging task in applications involving parametric sensing [10] and measurement of time and frequency [84]. Due to their different nature, noise sources can affect resonator amplitude and/or frequency [8], and several methods have been developed for noise characterization in driven systems. For example, in order to analyze the frequency noise in self-sustained oscillators, one can measure the fluctuations in the modal amplitude and phase [2]. In more recent work [78], by analyzing the shape of the spectrum of a driven nanomechanical resonator, the authors determine the presence of the direct frequency fluctuations and estimate its intensity compared with the thermal noise. In both methods, however, estimation of the noise statistics will necessarily have additional errors due to instrumental uncertainties in the driving electronics and/or elements of the feedback loop [85, 86].

We begin our discussion, in Section 3.1, by describing the device under study and the experimental setup used for measurement of the resonator ringdown response. Further, in Section 3.2, we provide a model for DA-DETF resonator, describe its validity and limitations and show how the resonator amplitude and frequency, or phase, behavior depends on model parameters. In Section 3.3 we discuss the characterization technique itself and illustrate the post-processing procedure that leads to estimation of deterministic modal parameters. We then proceed to characterization of noise sources affecting the resonator dynamics and measured response in Section 3.4. Finally, we provide concluding remarks in Section 3.5.

3.1 Device under study and measurement setup

In this work we carry out the ringdown-based characterization for the DA-DETF resonator shown in Fig. 3.1. The resonator was fabricated using an epitaxial polysilicon encapsulation

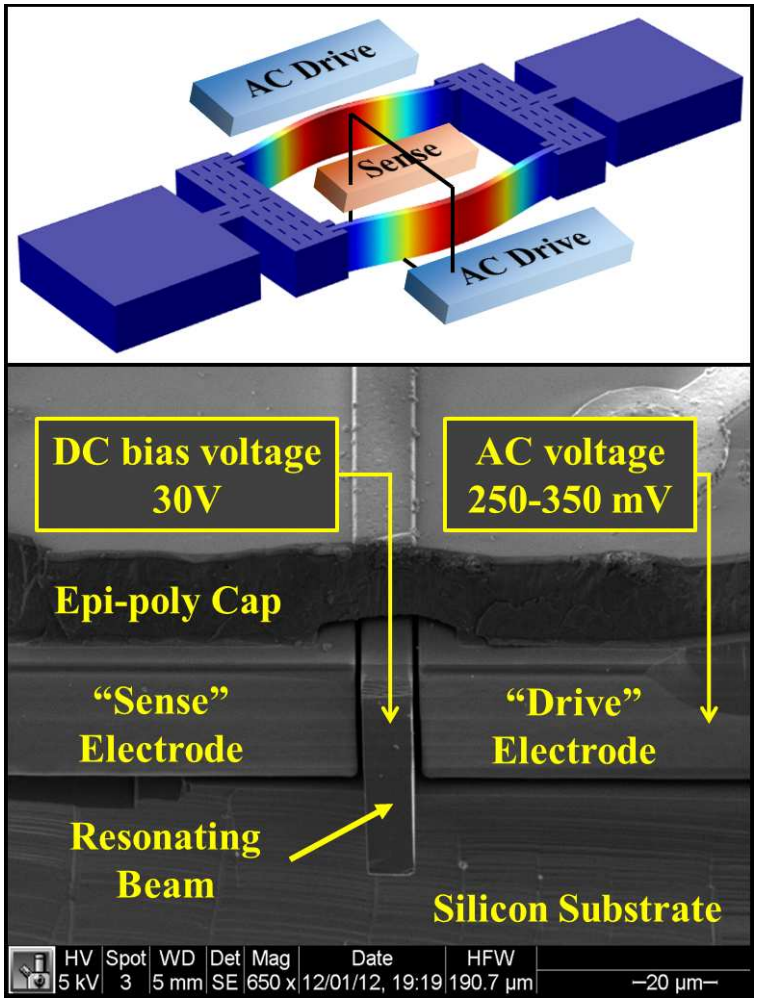

Figure 3.1: Top: COMSOL model of a micromechanical DA-DETF resonator showing the symmetric vibrational mode under study. The expected (using FEM analysis) values of the resonator linear parameters in the experiment are as follows: effective mode mass $m_{eff} \sim 0.2$ μg, quality factor $Q \sim 10^3 - 10^4$, and natural frequency $f_0 \approx 1.2$ MHz. The square denotes the location of the cross-sectional SEM. Bottom: SEM from a 45°-view angle of the resonator encapsulated with the *epi-seal* process.

process (*epi-seal*) [87] and it consists of two micromechanical beams $200\mu m$ long, $6\mu m$ wide and $40\mu m$ thick that are connected on both ends to perforated masses, which are further

anchored to the base. The perforation in the coupling mass serves as release-etch holes and does not affect the device performance. The encapsulation process results in a pressure of < 1 Pa in the cavity containing the resonator.

To prepare the system for the ringdown measurement, we first force the resonator to oscillate in the nonlinear regime using feedback loop. Previous research has demonstrated stable oscillation of this device beyond the critical bifurcation limit by controlling the operating phase of the resonator when the latter is driven in the closed-loop configuration [30]. Physically, the feedback loop compensates the losses in the resonator due to damping and provides an additional shift in the resonator phase ensuring that Barkhausen stability criterion is met. In this work, a Zurich HF2LI lock-in amplifier is used to control and maintain a variable-phase feedback loop, as shown in Fig. 3.2. The output of the lock-in amplifier

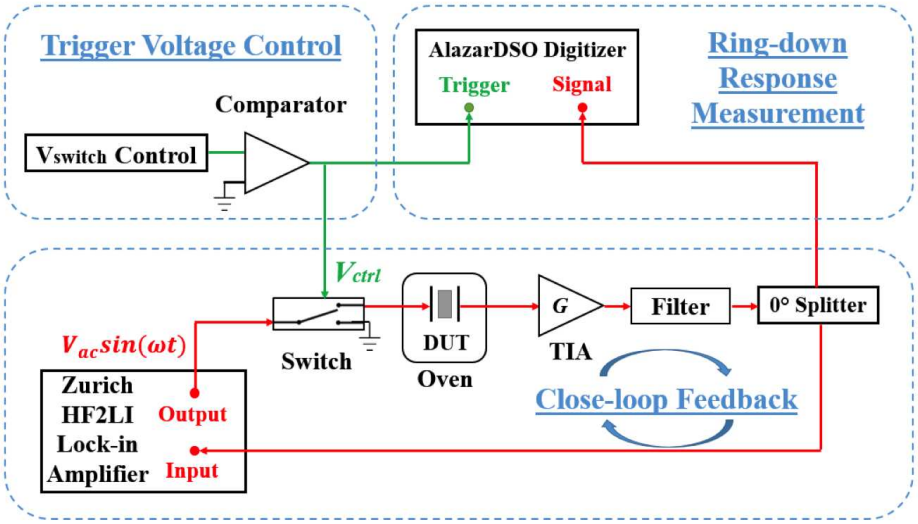

Figure 3.2: Variable-phase closed-loop feedback system with added capability for ringdown measurements. The encapsulated devices are placed into a Thermotron S-1.2c environmental chamber for temperature stabilization at $-40°$ C.

maintains the resonator motion by supplying a periodic signal ($V_{AC} = 200 - 300mV$) to two "Drive" electrodes. By tuning the phase shift in the feedback loop, we achieve the frequency

of self-sustained oscillations to be close to the nonlinear resonance; see Fig. 3.3. To achieve a strong output signal, we apply a DC voltage ($V_{DC} = 30V$) to the resonator body. Additionally, we maintain both driving and sensing electrodes at the "ground" voltage potential, thus ensuring the symmetry of the system potential energy.

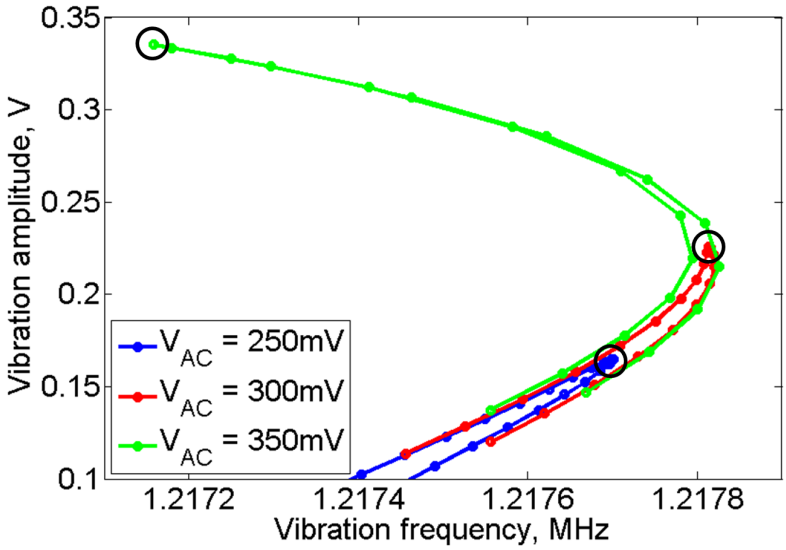

Figure 3.3: Measured amplitude-frequency responses of the micromechanical resonator in the feedback loop with $V_{DC} = 30V$ and different values of V_{AC} at $T = -40°$C. Each circle denotes the position of the nonlinear resonance where the system has been prepared for the subsequent ringdown measurement.

The resonator response is detected by the "Sense" electrode in the form of current that is electrostatically transduced due to the resonator vibration. This output current is then converted to a voltage signal and amplified via a transimpedance amplifier (TIA). We further pass the signal through a band-pass filter with corner frequencies 1.2 MHz and 7 MHz in order to remove low- and high-frequency measurement noise, and then split the signal with a 0° power splitter. One of the outputs is fed back to the lock-in amplifier, where the resonant frequency and amplitude can be tracked. The second signal component goes into an AlazarDSO ATS9360 digitizer for recording of the ringdown response. A voltage-controlled RF switch, placed between the lock-in output and the resonator, acts as the mechanism

for cutting the resonator driving. When the trigger voltage is set "High", the connection between the lock-in amplifier and resonator is closed, and we observe stable oscillatory signal via the AlazarDSO. Once the resonator vibrations reach steady-state, the trigger voltage is switched to "Low". In this case the falling edge cuts the input to the resonator coming from the lock-in amplifier and triggers the digitizer, allowing us to capture the full ringdown response, see Fig. 3.4. The collected data is then post-processed for characterization of the

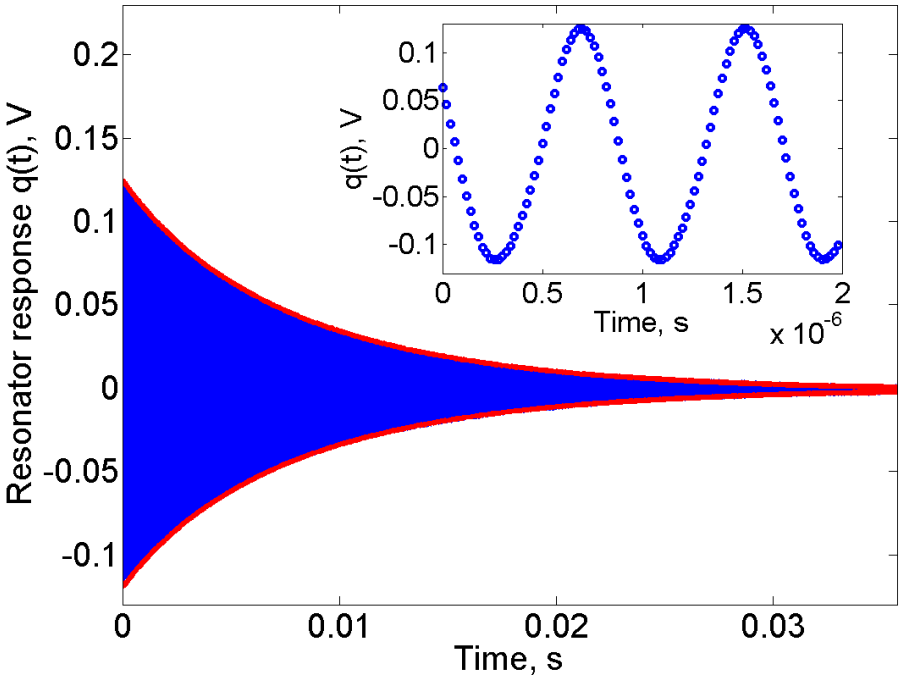

Figure 3.4: A measured ringdown response of the resonator under study; $V_{DC} = 30V$ and $V_{AC} = 250mV$. Red solid line indicates extracted vibrational envelope $a(t)$. Inset shows a time-expanded view of the initial portion of the signal.

parameters of the vibrational mode via the procedure described below.

3.2 Model

The dynamics of a micromechanical resonator with capacitive sensing depends on both mechanical forces arising in the resonator body and the electrostatic effects due to the bias

voltage [45]. In this work, the resonator flexural displacement $y(x,t)$, where x is the spatial coordinate along the beam, is much smaller than the resonator width, $y(x,t) \ll h$, which allows us to approximate the mechanical restoring force of the symmetric vibrational mode under the study by a 3^{rd}-order polynomial $\omega_{0m}^2 q + \gamma_m q^3$, where q is the modal displacement coordinate, ω_{0m} is the mechanical linear vibration frequency and γ_m is the mechanical Duffing nonlinearity which is positive for a clamped-clamped (CC) beam. These modal parameters can be obtained by (1) approximating the resonator deformation function as

$$y(x,t) = q(t)\theta(x), \tag{3.1}$$

where $\phi(x)$ is the ideal mode shape of a CC beam, which we approximate further by *an assumed mode*, given by a simple polynomial that satisfies the CC boundary conditions, namely,

$$\theta(x) = 16x^2(1-x)^2, \tag{3.2}$$

and (2) using the Galerkin projection of the original equation of motion for the beam on the specific vibrational mode [45, 88]. Further, since the resonator is biased symmetrically we model the electrostatic force acting on the resonator during its ringdown as

$$F_{el} = \kappa[(d - y(x,t))^{-2} - (d + y(x,t))^{-2}], \tag{3.3}$$

where d is the nominal electrode gap size and κ is the strength of the electrostatic force, which depends on the resonator dimensions and the bias voltage. In order to obtain the expression for an equivalent electrostatic force acting on the vibrational mode, one would have to project F_{el} on this mode, which is generally a challenging task, see Appendix B.

However, noticing that, by definition, $y(x,t)/d < 1$, we can expand F_{el} in a Taylor series about $q = 0$. Since $d \ll h$, we can keep in this expansion higher-order terms. These terms can become comparable to the nonlinear term $\propto q^3$ where the expansions of the both mechanical and electrostatic forces apply. We will keep terms up to 5^{th} order in q/d and then perform the Galerkin projection. It is important to note that the mechanical and electrostatic forces are both symmetric. Since the terms of different powers in q can become comparable in these two forces, different effects can come into play depending on the amplitude. The mechanical nonlinearity is hardening and the electrostatic nonlinearity is softening. The natural frequency (from the linear term) includes both effects, and for the present device and bias voltage the cubic term is dominated by mechanical effects and is hardening, while the quintic nonlinearity is dominated by the electrostatic effects and is softening. This leads to the inflection point on the amplitude dependence of the vibration frequency seen in Fig. 3.3.

After combining mechanical and electrostatic effects together, the dynamics of a vibrational mode of a symmetric micromechanical resonator can be described for moderate modal amplitudes by the following phenomenological model

$$\ddot{q} + 2(\Gamma_1 + \Gamma_2 q^2)\dot{q} + q(\omega_0^2 + 2\omega_0\eta(t)) + \gamma q^3 + \beta q^5 = f(t), \tag{3.4}$$

where q is again the modal displacement coordinate, ω_0 is the natural frequency of the mode, Γ_1 and Γ_2 are the coefficients of linear and nonlinear friction, and γ and β are the coefficients of the conservative Duffing and quintic nonlinearities respectively. The linear damping constant Γ_1 determines the resonator decay at small vibration amplitudes and is related to the resonator quality factor as $Q = \omega_0/2\Gamma_1$. Note that ω_0 is primarily defined by

ω_{0m}, but is slightly reduced by the presence of the electrostatic actuation/sensing scheme (electrostatic frequency tuning effect). To complete the model, we also include additive, $f(t)$, and multiplicative, $\eta(t)$, noise sources, which can be of thermal or non-thermal origin.

Qualitatively, the nonlinear and noise terms in Eq. (3.4) have the following effects, to the first order: the stiffness nonlinearities γ and β cause an amplitude-dependent frequency shift, the nonlinear damping Γ_2 produces an amplitude-dependent damping (and a non-exponential decay), while the noise processes make both the amplitude and frequency fluctuate about the deterministic response of the resonator. The decay of the oscillation amplitude is determined by the terms of Eq. (3.4) proportional to Γ_1 and Γ_2, and also by $f(t)$ and $\eta(t)$. Thus, in a standard spectral measurement, γ, β and Γ_2 (and the noise terms [78]) lead to a deviation of the spectral contour from the Lorentzian, and it is usually impossible to accurately extract these parameters from a single frequency sweep. In contrast, as we show, a ringdown measurement is very sensitive to these nonlinearities and noise sources.

In the absence of the noise terms in Eq. (3.4), the dynamics of the resonator ringdown response can be studied in terms of slowly-varying (on the time scale $\sim \omega_0^{-1}$) resonator amplitude $a(t)$ and phase $\phi(t)$

$$q(t) = a(t)\cos\left(\omega_0 t + \phi(t)\right), \tag{3.5a}$$

$$\dot{q}(t) = -\omega_0 a(t)\sin(\omega_0 t + \phi(t)). \tag{3.5b}$$

Substituting this change of variables into equation Eq. (3.4), applying the method of averaging and neglecting fast-oscillating terms [89], we obtain the following equations of motion

for the modal amplitude and phase

$$\dot{a} = -\left(\Gamma_1 + \frac{1}{4}\Gamma_2 a^2\right)a, \tag{3.6a}$$

$$\dot{\phi} = \frac{3\gamma}{8\omega_0}a^2 + \frac{5\beta}{16\omega_0}a^4. \tag{3.6b}$$

From Eq. (3.6a) it is clear that the amplitude dynamics are unaffected by the conservative nonlinearities, while the phase depends on the amplitude through both γ and β, as expected. In fact, it can be shown that the amplitude decay is independent of γ and β even in the presence of noise [49]. The solution for the resonator vibrational envelope can be obtained in closed form,

$$a(t) = a_0 e^{-\Gamma_1 t}/\sqrt{g(t)}, \quad g(t) = 1 + \frac{1}{4}\frac{\Gamma_2}{\Gamma_1}a_0^2(1 - e^{-2\Gamma_1 t}) \tag{3.7}$$

where a_0 is the initial value of the modal amplitude in the ringdown response; see Fig. 3.4. Using this solution in the expression for $\dot{\phi}$ in Eq. (3.6b), we obtain the solution for the resonator phase

$$\phi(t) = \frac{3}{4\omega_0\Gamma_2}\left(\gamma - \frac{10\beta\Gamma_1}{3\Gamma_2}\right)\ln g(t) + \frac{5\beta a_0^2}{8\omega_0\Gamma_2}\frac{g(t) - e^{-2\Gamma_1 t}}{g(t)}, \tag{3.8}$$

where we omit the initial resonator phase since it is determined by an arbitrary choice of $t = 0$. The existence of closed-form solutions for the resonator amplitude and phase allows us to develop a ringdown-based technique for estimating the resonator parameters, including conservative and dissipative nonlinear coefficients, see Section 3.3.

It is worth mentioning a possible origin of the nonlinear dissipation in MEMS resonators.

According to the microscopic theory of dissipation discussed in [49], nonlinear friction is an essential consequence of the nonlinear interaction of the primary resonant mode with phonons, as is also the case for linear friction [49]. For high-Q resonators, the adequate description of nonlinear friction is in fact given by Eq. (3a); in the phenomenological picture, the term $\propto \Gamma_2$ can come either from the friction force of the form of $q^2\dot{q}$ or $\dot{q}^3$, or from their combination. If the phonons that lead to the relaxation are in thermal equilibrium, there is an interrelation between the nonlinear friction coefficient Γ_2 and the intensity of the noise $\eta(t)$ with the spectrum around $2\omega_0$, see [33], similar to the familiar interrelation between Γ_1 and the intensity of the additive noise $f(t)$.

3.3 Characterization of $\omega_0, \Gamma_1, \Gamma_2, \gamma$ and β parameters

As we mentioned in the introductory part of the chapter and showed formally in Section 3.2, the resonator stiffness and dissipation parameters have qualitatively different effects on the system ringdown response. In particular, the resonator damping coefficients Γ_1 and Γ_2 determine the resonator vibration envelope, as it follows directly from Eq. (3.7). At the same time, the resonator instantaneous vibration frequency is dictated by the form of the system potential energy, which, in turn, is determined by a combined effect of stiffness parameters ω_0, γ and β, see Eq. (3.6b). In this light, by separating the resonator vibration envelope and the frequency-amplitude relationship in the system ringdown response, we can effectively separate effects of the resonator conservative and dissipative parameters, see Fig. 3.5. Furthermore, we expect that as the resonator vibration amplitude decreases, the system returns to its linear regime, meaning that the resonator vibration frequency approaches its amplitude-independent value ω_0 and the energy decay is essentially exponential as being

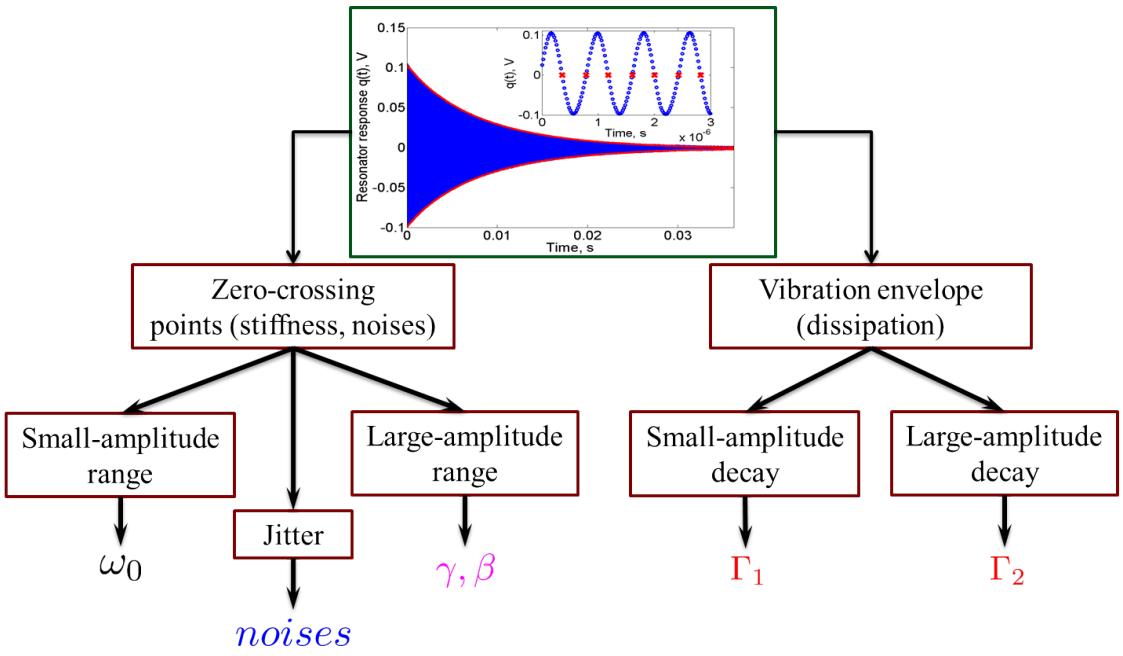

Figure 3.5: The road-map for the ringdown-based characterization method. Separation of dissipative and conservative parameters of the system under study is achieved through independent analyses of the vibration envelope and the form of the resonator "backbone." Furthermore, small- and large-amplitude components of the system ringdown signal are used for effective characterization of the resonator linear and nonlinear coefficients, while the jitter in the ringdown zero-crossing points provides information about noise sources present in the system.

dominated by Γ_1. As a result, the small-amplitude part of the resonator ringdown measurement can be used for immediate characterization of the system linear parameters: the natural frequency ω_0 and linear damping constant Γ_1. In contrast, nonlinear terms in the resonator dissipative and restoring forces affect the large-amplitude part of the resonator ringdown, which allows us to estimate the values of γ, β and Γ_2 coefficients from a single ringdown measurement.

In order to extract the resonator vibration envelope and the "backbone" curve (the dependence of the instantaneous oscillation frequency on the resonator amplitude) from the ringdown response, one can utilize different post-processing methods, such as fast Fourier transform (FFT) and Hilbert decomposition, see [90–92]. In Section 3.3.1, we have employed

the heterodyning technique for extracting the resonator vibration envelope since this method also allows us to study the dynamic behavior of the resonator slowly-varying quadratures during the ringdown [83]. To obtain the relationship between the resonator instantaneous frequency and amplitude, we have utilized the method of zero-crossing points in Section 3.3.2. While this method is very intuitive and simple to use, the main advantage of using zero-crossing points is that this technique provides means for studying thermal, frequency and measurement noise sources, which result in fluctuations, or *jitter*, of the locations of zero-crossing points in the system response [84]. Analysis of this jitter, as discussed in Section 3.4, allows one to reveal all mentioned noise sources and, more importantly, to estimate noise intensities.

3.3.1 Revealing nonlinear friction and extracting Γ_1, Γ_2

In this work we have started the resonator characterization process by estimating the system damping coefficients from the resonator vibration envelope. In order to extract the resonator vibrational amplitude $a(t)$, the recorded ringdown data shown in Fig. 3.4 has been heterodyned with the in-phase and quadrature components at the frequency of self-sustained oscillations prior to the ringdown measurement,

$$\omega_{ss} = \omega_0 + \Delta\omega(a_0), \tag{3.9}$$

see Fig. 3.6. Next, we have passed mixed signals through a low-pass filter in order to remove the second and other higher-order harmonics and isolate slowly-varying (on the time scale $\sim \omega_0^{-1}$) resonator quadratures, $q_x(t)$ and $q_y(t)$. Finally, we have reconstructed the resonator vibrational envelope using the well-known relationship between the Cartesian and polar

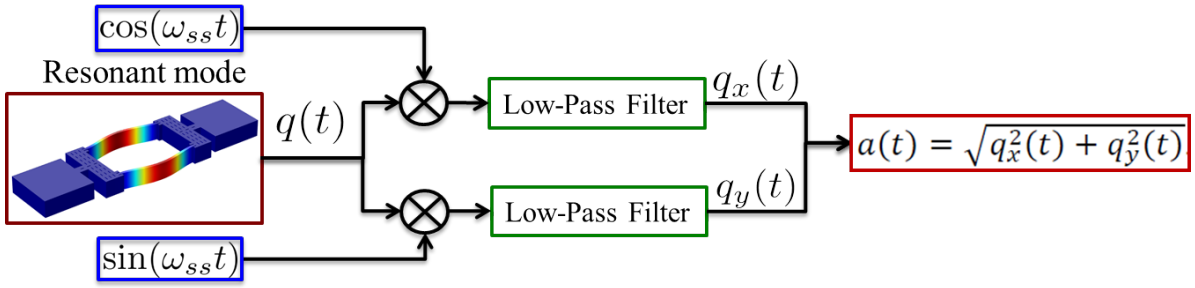

Figure 3.6: Post-processing method used for extracting the resonator vibrational envelope from the ringdown measurement. Initial heterodyning of the resonator ringdown response with in-phase and quadrature signals at ω_{ss} and subsequent isolation of the system slowly-varying quadratures allows one to reconstruct the resonator vibrational amplitude $a(t)$.

coordinates as

$$a(t) = \sqrt{q_x^2(t) + q_y^2(t)}. \tag{3.10}$$

In order to reveal the presence of nonlinear dissipation in the resonant system of interest, it is convenient to plot the resonator vibration amplitude $a(t)$ on logarithmic scale, see Fig. 3.7. As expected, when the resonator rings down, its amplitude decreases and the effect of Γ_2 on the vibrational envelope becomes smaller. In the final part of the ringdown response, the resonator motion is essentially independent of Γ_2 and the resonator energy decays exponentially with the speed determined by Γ_1 and proportional to the slope of the curve in Fig. 3.7. By finding this slope one can estimate the resonator linear decay rate Γ_1, see Table 3.1. As expected, the resonator decay pattern deviates from a simple exponential

Table 3.1: Estimated values of the linear and nonlinear dissipation coefficients and conservative nonlinearity for different initial amplitudes. Ringdown measurements have been performed with $V_{DC} = 30$V and at $T = -40^{\circ}C$.

$a_0(mV)$	$\Gamma_1(s^{-1})$	$\Gamma_2(s^{-1}V^{-2})$	$\gamma(s^{-2}V^{-2})$	$\beta(s^{-2}V^{-4})$
130	116.8	7893	1.12×10^{12}	-2.2×10^{13}
175	122.4	8479	0.93×10^{12}	-2.64×10^{13}
265	119	6011	1.05×10^{12}	-2.07×10^{13}

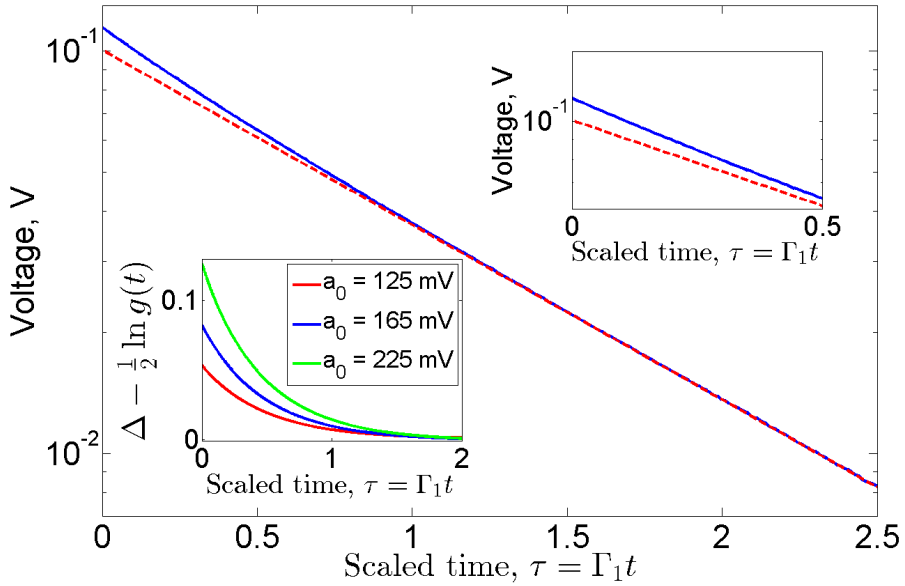

Figure 3.7: Measured vibrational amplitude of the DETF resonator during its ringdown response with $V_{DC} = 30$V (solid line). The dashed line represents the exponential decay of the resonator amplitude at low vibration amplitudes, extended throughout the amplitude range. Upper inset: nonlinear friction causes the ringdown amplitude envelope to deviate from exponential at large amplitudes, which can be used for characterization of Γ_2. Lower inset: the effect of nonlinear dissipation on the ringdown response becomes stronger as the initial amplitude increases.

form at large-to-moderate vibration amplitudes due to the presence of nonlinear damping, see the upper inset in Fig. 3.7. Importantly, this effect becomes stronger as the initial amplitude increases. Analysis of equation Eq. (3.7) shows that the maximum of this deviation (on logarithmic scale) reads

$$\Delta = \lim_{t\to\infty}\left[\ln\left(\frac{a_0}{a(t)\exp(\Gamma_1 t)}\right)\right] = \frac{1}{2}\ln\left(1+\frac{\Gamma_2 a_0^2}{4\Gamma_1}\right), \tag{3.11}$$

which can be used to estimate the magnitude of Γ_2, see Table 3.1. Alternatively, one can fit extracted vibrational amplitude $a(t)$ with the model described in equation Eq. (3.7) using, for example, the least-square method and estimate both damping coefficients Γ_1 and Γ_2.

3.3.2 Extracting the resonator stiffness coefficients ω_0, γ, β

After characterizing the resonator dissipative parameters, we can proceed with estimating the system natural frequency ω_0 as well as Duffing and quintic nonlinearities γ and β. According to Eq. (3.6b), the resonator instantaneous frequency depends on the amplitude $a(t)$ as follows,

$$\omega(t) = \omega_0 + \frac{3\gamma}{8\omega_0}a^2(t) + \frac{5\beta}{16\omega_0}a^4(t). \tag{3.12}$$

This behavior of the vibration frequency corresponds to decay along the resonator "backbone" curve in the amplitude-frequency space. As we discussed above, the effects of β and γ are expected to diminish as the resonator enters its linear regime, where the modal frequency approaches ω_0. In order to extract the resonator instantaneous frequency and estimate ω_0, γ and β from a single ringdown response, we analyze the sequence of the zero-crossing times $\{\tau_k\}$ in the resonator response, i.e., the points that satisfy $q(\tau_k) = 0$, as outline below.

During the resonator ringdown, the vibration amplitude and frequency are not constant, but change smoothly in time (ignoring the effects of noise). Based on this, we partition the ringdown response into N segments of length $2\pi/\omega_0 \ll \Delta t \ll \Gamma_1^{-1}$. We assume that the vibration amplitude and frequency remain essentially fixed within each segment, but change in a discrete manner from one segment to the next. In this case our procedure corresponds to a discretization of smooth amplitude and frequency functions. In this spirit, we define the vibration period associated with i^{th} time segment as

$$T_i = 2\frac{t_{i,n_i} - t_{i,1}}{n_i - 1} = \frac{2\pi}{\omega_i}, \tag{3.13}$$

where $t_{i,j}$ is the j^{th} zero-crossing point and n_i is the number of zero-crossing points within

the i^{th} interval. Extracted values of the vibration period T_i are then used to compute the resonator quasi-instantaneous vibration frequency shown in Fig. 3.8 for $N = 50$. Note that

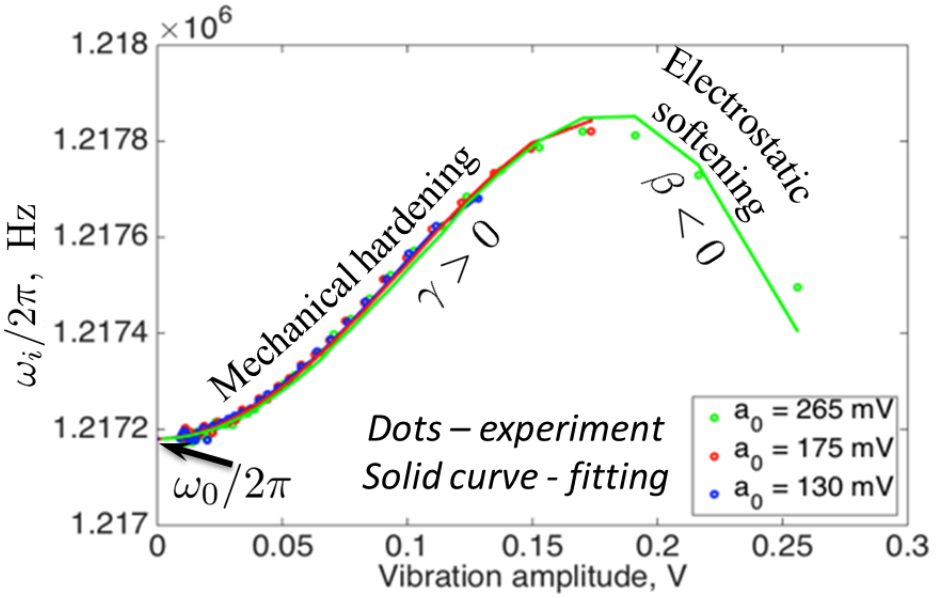

Figure 3.8: Vibration frequency of the resonator during the ringdown as a function of its amplitude for different values of initial amplitude. Due to amplitude-dependent frequency pulling, the frequency varies with amplitude, allowing characterization of ω_0, γ and β from a single measurement. Discrete dots represent extracted values of the vibration frequency $\omega_k/2\pi$ during the ringdown response (error bars $\approx 1 - 10\ Hz$, not shown). The solid lines represent the curve fits of extracted "backbones" using the model in Eq. (3.12).

partitioning of the resonator ringdown results in the vibration frequency being averaged over Δt, and mentioned above jitter in zero-crossing points is essentially averaged out. As a result, by choosing specific value of N one would always compromise between the amount of data points in the resonator "backbone" and the amount of jitter that is being averaged/retained.

The form of the resonator frequency-amplitude dependence exhibits several features of interest. First, as expected, the value of the vibration frequency at the beginning of the ringdown, ω_1, depends on the initial vibration amplitude a_0 and on stiffness nonlinearities γ and β, due to the amplitude-dependent frequency pulling. As the resonator motion decays, the vibration frequency changes in a monotonic (for $\gamma\beta > 0$ *or* if the initial amplitude is below the turning point) or non-monotonic (for $\gamma\beta < 0$ *and* the initial amplitude above the turning

point) manner and gradually approaches ω_0, from where we estimated the linear resonant frequency to be $f_0 \approx 1.2172$ MHz. After obtaining the vibration period (and frequency) as a function of time, we can estimate the resonator Duffing and quintic nonlinearities by fitting the amplitude-dependent frequency shift

$$\Delta\omega(a) = \omega(a) - \omega_0 \tag{3.14}$$

to the model described in Eq. (3.12) using the least-square fitting method, see Table 3.1.

It is worth mentioning that the zero-crossing-based method presented here can be easily extended and used to capture the resonator stiffness nonlinearities of orders higher than 5. These higher-order nonlinearities will result in additional terms in Eqs. (3.6b) and (3.12) that dictate the behavior of $\Delta\omega(a)$. Clearly, this method of zero-crossing points is accurate and very simple from a computational point of view, as it allows one to extract ω_0, γ and β directly from the raw data without involving the Fourier transform of a signal that has a non-stationary and, generally, non-monotonic vibration frequency.

3.3.3 Separating mechanical and electrostatic effects in MEMS resonators

The dynamic behavior of MEMS resonators with electrostatic transduction is determined by both mechanical restoring forces arising from elastic deformations in the resonator body and the electrostatic interaction of the resonator with attendant electrodes, which arises from a finite bias voltage [45]. Knowledge of both mechanical and electrostatic contributions to the resonator amplitude-dependent frequency pulling effect becomes crucial for accurate tuning of the resonator parameters, for example, for maximizing the resonator linear dynamic

range using systematic shape optimization of the resonator body [43]. While decoupling of mechanical/kinematic and electrostatic effects can be achieved in electrostatic MEMS by using, for example, a piezoelectric stack actuator [93] and optical sensing method [94] to achieve a purely mechanical response, this technique requires considerable change of the resonator driving/sensing apparatus and additional measurement tools. Moreover, such a method is not applicable for resonant systems that are encapsulated [87]. In this light, there is a need for a simple and reliable characterization method that allows one to estimate both mechanical and electrostatic contributions to the linear and nonlinear resonator stiffness parameters, while employing an electrostatic drive/sense setup. As we show below, it is possible to adapt the ringdown-based characterization method described above for separating mechanical and electrostatic effects in MEMS resonators with electrostatic actuation and/or sensing schemes.

Mechanical forces in flexural-mode resonators vibrating in a single plane originate from two qualitatively different mechanisms: resonator bending (flexure) and mid-line stretching (extension). In particular, restoring forces due to resonator bending normally dominate the system dynamics at vibrational amplitudes that are much smaller than the resonator thickness h in the direction of vibration. The effect of mid-line stretching, on the other hand, is nonlinear in the resonator displacement and reveals itself at higher vibration amplitudes [95], and it results in an amplitude-dependent shift of the resonator vibrational frequency [96]. Physically, this manifests itself in an effective *hardening* of the resonator stiffness, resulting in an increase in the vibration frequency as the amplitude increases. Here, the resonator thickness h serves as an important characteristic length scale that dictates the appearance of nonlinear effects in the resonator stiffness that arise due to normal stresses occurring in the resonator body during its vibratory response.

Unlike mechanical restoring forces, both linear and nonlinear electrostatic effects originate from the same physical process of electrostatic interaction of the resonator body with the attendant electrodes. The effect of this interaction is expressed by a single electrostatic potential function, which diverges when the resonator amplitude approaches the electrode gap size d. Since the resonator displacement $y(x,t)$ cannot physically exceed d[1], one can expand the electrostatic potential about the resonator equilibrium position and obtain corresponding electrostatic contributions to both linear and nonlinear resonator restoring forces. Importantly, the larger the resonator displacement, the more terms one has to keep in the expansion of the electrostatic potential for accurate modeling of the system dynamics. In this light, the electrode gap size d is another important length scale that determines the appearance of certain electrostatic effects in the potential, or, equivalently, in the expansion of the attendant restoring force.

Typically, the electrode gap size is the smaller of these length scales in MEMS resonators with electrostatic transduction and high frequency, so that $d \ll h$ often holds. Consequently, depending on the relative magnitudes of h and d, one may have to retain mechanical and/or electrostatic nonlinear terms of different orders in the resonator displacement, as was done in Section 3.2. Physically, the electrostatic forces pull the resonator away from its equilibrium position and therefore reduce the resonator stiffness and cause *softening* of the resonator frequency response [99]. As a result, the resonator dynamic behavior is determined by the competition of mechanical (hardening) and electrostatic (softening) effects, and this interplay of different restoring mechanisms can result in peculiar forms of the resonator amplitude-frequency response, such as the one shown in Fig. 3.3.

[1]In fact, $y(x,t) \lesssim 0.7d$ is frequently satisfied in order to avoid the pull-in phenomenon [97, 98] and/or prevent the device from electrical shorting.

By accounting for the aforementioned mechanical and electrostatic forces acting on the resonator, we can obtain the following model for the resonator natural frequency and amplitude-dependent frequency shift (see Appendix B for details),

$$\omega_0 = \sqrt{\omega_{0m}^2 - \frac{3C_e}{d}}, \tag{3.15a}$$

$$\Delta\omega(a) = \Delta\omega_m(a) + \Delta\omega_e(a), \tag{3.15b}$$

where ω_{0m} is the resonator mechanical natural frequency and

$$C_e = \frac{2\epsilon_0 V_b^2}{3\rho h d^2} \tag{3.16}$$

is the strength of electrostatic potential that depends on the beam mass density ρ, beam in-plane thickness h, electrode gap size d, and the applied bias voltage V_b. In Eq. (3.15b), $\Delta\omega_{m,e}(a)$ are the corrections to the modal vibration frequency due to nonlinear mechanical and electrostatic effects, respectively. Closed-form expressions for $\Delta\omega_{m,e}(a)$ are quite cumbersome and are relegated to Appendix B. In practice, however, modal amplitudes in high-frequency flexural-mode resonators with a "clamped-clamped beam" configuration frequently satisfy $a/h \ll a/d < 1$, which allows us to approximate the magnitudes of the mechanical and electrostatic nonlinear frequency pulling, as follows,

$$\Delta\omega_m(a) \approx \frac{3\gamma_m}{8\omega_0}a^2, \quad \gamma_m = \frac{\pi^4 E}{3\rho L^4}, \tag{3.17a}$$

$$\Delta\omega_e(a) \approx \frac{3\gamma_e}{8\omega_0}a^2 + \frac{5\beta_e}{16\omega_0}a^4, \quad \gamma_e = -\frac{35C_e}{8d^3}, \quad \beta_e = -\frac{693C_e}{128d^5}. \tag{3.17b}$$

Note that while we approximate $\Delta\omega_m(a)$ in Eq. (3.17a) only by the first non-vanishing

term $\propto a^2$, which comes from the cubic (Duffing) term in the resonator restoring force, we retain contributions from both cubic and quintic electrostatic nonlinearities in $\Delta\omega_e(a)$. The validity of this approximation has been verified in the analysis; in fact, even when $a \approx d$, the contribution of the mechanical quintic term (due to the mid-line stretching) to the resonator frequency shift, which is $\propto a^4$ in $\Delta\omega_m(a)$, is several orders of magnitude smaller than the corresponding contribution of the mechanical Duffing term, i.e.,

$$\frac{5|\beta_m|}{16\omega_0}d^4 \ll \frac{3\gamma_m}{8\omega_0}d^2.$$

In contrast, the electrostatic potential diverges as $a \to d$ and the electrostatic quintic term dominates the softening behavior of the resonator frequency at higher vibration amplitudes. In this light, the coefficient of the resonator quintic stiffness term is approximated as $\beta \approx \beta_e$, which we keep in the analysis in order to adequately describe the hardening-to-softening behavior of the resonator frequency response shown in Fig. 3.3.

These qualitative and quantitative differences between nonlinear mechanical and electrostatic forces allow us to characterize both effects using a single resonator ringdown response. In particular, our ability to characterize the resonator lumped stiffness parameters: ω_0, γ and β allows us to estimate the strength of the electrostatic potential C_e using the last expression in Eq. (3.17b). Knowing C_e, we can further calculate the corresponding electrostatic contributions to the resonator natural frequency and Duffing nonlinearity γ_e. Finally, by accounting for these electrostatic contributions, we can determine the mechanical natural frequency,

$$\omega_{0m} = \sqrt{\omega_0^2 + \frac{3C_e}{d}}, \tag{3.18}$$

Table 3.2: Estimated values of the mechanical natural frequency ω_{0m}, the mechanical contribution to the Duffing nonlinearity γ_m, and the electrostatic potential strength C_e in the DA-DETF resonator (see Fig. 3.1) for three independent ringdown measurements with the same bias voltage, $V_{DC} = 30\ V$.

$a_0\ (mV)$	$\omega_{0m}/2\pi\ (Hz)$	$\gamma_m\ (m^{-2}s^{-2})$	$C_e\ (m/s^2)$
130	1.241×10^6	1.237×10^{24}	6.51×10^5
175	1.238×10^6	1.403×10^{24}	7.81×10^5
265	1.242×10^6	1.155×10^{24}	6.1×10^5

and the Duffing nonlinearity,

$$\gamma_m = \gamma + \frac{35C_e}{8d^3}. \tag{3.19}$$

Table 3.2 shows some data obtained from a measured ringdown response.

It is worth mentioning that this method for separating mechanical and electrostatic effects is not limited to resonant systems with flexural vibrational modes and should be applicable to other types of MEMS resonators including, for example, bulk-mode resonators. While the physical origins of mechanical nonlinearities can include both geometric and material effects, their appearance in the resonator model is determined by relatively large resonator dimensions, such as the resonator thickness (for flexural modes) or width (for bulk modes). In contrast, electrostatic forces still originate from the electrostatic potential with the characteristic length equal to the electrode gap size, which remains the smallest geometric feature of MEMS resonators with electrostatic transduction. As a result, the resonator quintic stiffness term should still be dominated by the electrostatic potential and, by driving the resonator to sufficiently large vibration amplitude, one should be able to characterize the strengths of the electrostatic potential and mechanical contributions to the resonator stiffness parameters.

3.4 Characterization of thermal, frequency and measurement noise sources

To this point we have discussed how one can characterize the *deterministic* resonator parameters, both dissipative and conservative, using a single ringdown response measurement. Of course, the resonator dynamics are not deterministic but are influenced by interactions of the resonator body with an ambient environment. These interactions, as we described in Section 1.2, have different physical origins; however, the collective effect of these interactions on the resonator dynamic behavior can be modeled in the form of random excitations or *noises*.[1] Depending on a noise nature and origin, we can model them as *additive*, or thermal, noise, i.e., being independent of the resonator instantaneous displacement and velocity, or, as *multiplicative*, or frequency, noise. Also, when one measures the resonator response, the imperfections of the detecting device typically result in an additional noise that perturbs the measured signal, which we model as *measurement* noise. The effects of these noise sources on the resonator dynamics and the readout signal are illustrated schematically in Fig. 3.9, where we assume that measurement noise does not affect the resonator dynamics itself, but merely corrupts the readout signal. In this section we show how we can use the resonator

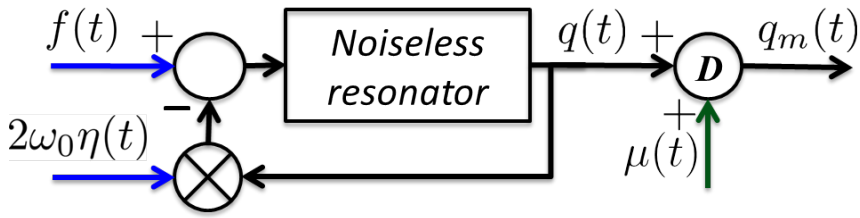

Figure 3.9: Schematic representation of the effects of thermal ($f(t)$) and frequency ($\eta(t)$) noises on the resonator dynamics, and the effect of measurement noise ($\mu(t)$) on the quality of the readout signal.

[1] These same interactions are also the source of the damping effects already studied, where dissipation is the mean component of these random effects and the fluctuating components are modeled as noise [49].

ringdown response for characterization of measurement, additive, and multiplicative noise sources. In particular, we demonstrate that these noises cause jitter in the zero-crossing points in the resonator ringdown and, more importantly, they have different signatures in the resonator timing jitter, which allows us to reveal and separate their effects and estimate their individual noise intensities.

In terms of notation, we use $(\cdot)_d$ to denote the deterministic value of the quantity in the parenthesis, such as the resonator amplitude, a, or frequency, ω, while $(\cdot)_r$ and $(\cdot)_\mu$ will denote variations of this quantity induced by resonator-related and measurement noise sources, respectively. The jitter in the zero-crossing points manifests itself in the fact that the location of an arbitrary zero-crossing point τ_k deviates from its deterministic value, τ_{dk}, obtained by solving Eq. (3.8) for $\phi(\tau_{dk}) = \pi k$, as

$$\tau_k = \tau_{dk} + \delta\tau_{rk} + \delta\tau_{\mu k}, \tag{3.20}$$

where $\delta\tau_{rk}$ and $\delta\tau_{\mu k}$ are random shifts of the location of τ_k due to resonator-related noises (thermal and frequency) and measurement noise, respectively. In order to analyze the jitter in zero-crossing points during the resonator ringdown, we have to account for the non-stationary nature of the resonator response itself, which ultimately leads to non-stationarity of the resonator frequency fluctuations. In this light, similar to the approach used in Section 3.3.2, we partition the ringdown measurement into N segments of width $\omega_0^{-1} \ll \Delta t \ll \Gamma_1^{-1}$, and assign index i, unless specified otherwise, to denote the counting number of these ringdown segments. Next, we calculate the following time intervals within the i^{th} ringdown segment

$$\mathcal{T}(i,j,k) = \tau_{i,j+k} - \tau_{i,j} = \mathcal{T}_d(i,j,k) + \delta\mathcal{T}(i,j,k), \tag{3.21}$$

$$\delta\mathcal{T}(i,j,k) = \delta\mathcal{T}_r(i,j,k) + \delta\mathcal{T}_\mu(i,j,k), \tag{3.22}$$

$$\delta\mathcal{T}_r(i,j,k) = \delta\tau_{ri,j+k} - \delta\tau_{ri,j}, \tag{3.23}$$

$$\delta\mathcal{T}_\mu(i,j,k) = \delta\tau_{\mu i,j+k} - \delta\tau_{\mu i,j}, \tag{3.24}$$

where $\tau_{i,j}$ is the j^{th} zero-crossing point within the i^{th} ringdown segment. Physically, $\mathcal{T}(i,j,k)$ corresponds to the time that it takes for the resonator to accumulate πk radians of phase starting from $\tau_{i,j}$ on the timeline. In what follows, we shall assume that measurement noise is independent and uncorrelated with the resonator-related noise sources $f(t)$ and $\eta(t)$, which results in the fact that $\delta\tau_{rk}$ and $\delta\tau_{\mu k}$ are also uncorrelated, i.e.,

$$\langle \delta\tau_{rk}\delta\tau_{\mu k}\rangle_k \equiv 0. \tag{3.25}$$

As a result, we have for $\delta\mathcal{T}(i,j,k)$

$$\langle \delta\mathcal{T}^2(i,j,k)\rangle_j = \langle \delta\mathcal{T}_r^2(i,j,k)\rangle_j + \langle \delta\mathcal{T}_\mu^2(i,j.k)\rangle_j, \tag{3.26}$$

where $\langle\cdot\rangle_j$ denotes averaging over the j index, which, in our case, is assumed to be equivalent to ensemble averaging for different time intervals $\mathcal{T}(i,j,k)$ within the same ringdown segment.

3.4.1 Measurement noise timing jitter $\delta\mathcal{T}_\mu(i,j,k)$

The measured resonator ringdown response is a digitial representation of the resonator displacement that is estimated, using an appropriate detecting device, at specified instances of time t_p. In this work, we assume that measurement noise does not affect the resonator

internal dynamics and thus model the effects of a detection scheme on the readout signal in the following way,

$$q_m(t_p) = q_r(t_p) + \mu(t_p), \tag{3.27}$$

where $q_r(t_p) = q_{rp}$ is the signal that describes the resonator dynamics affected by additive and multiplicative noise sources, which we would detect given an ideal measurement apparatus, $\mu(t_p) = \mu_p$ is a random component added to q_{rp} due to the presence of measurement noise, and $q_m(t_p) = q_{mp}$ is the readout of the resonator displacement. In what follows, we assume μ_p to be a random variable having a symmetric probability distribution with the following statistics,

$$\langle \mu_p \rangle_p = 0, \quad \langle \mu_p \mu_s \rangle_{ps} = \mathcal{M}\delta_{ps}, \tag{3.28}$$

where δ_{ps} is Kronecker delta symbol. As we shall show later, this model, despite its relative simplicity, allows one to explain certain noise-induced features of the ringdown responses obtained from the DA-DETF resonator.

Given the signal in the form of Eq. (3.27), as the measured resonator ringdown, we consider the sequence of measured zero-crossing points $\{\tau_{mi,j}\}$ satisfying $q_m(\tau_{mi,j}) = 0$. We denote the sampling rate at which measurements are performed as f_s, and assume that it is much higher than the resonator vibration frequency, i.e., $f_0 \ll f_s$, so that the zero-crossing points $\tau_{mi,j}$ can be obtained from the measured data with sufficient accuracy using linear interpolation of the resonator response in the vicinity of $q_{mi,j} = 0$. Thus, for an arbitrary zero-crossing point, considering Fig. 3.10, we see that

$$\begin{aligned} \tau_{mi,j} &= \frac{q_{m2}t_1 - q_{m1}t_2}{q_{m2} - q_{m1}} = \frac{(q_{r2} + \mu_2)t_1 - (q_{r1} + \mu_1)t_2}{q_{r2} - q_{r1} + \mu_2 - \mu_1} \\ &\approx \frac{q_{r2}t_1 - q_{r1}t_2}{q_{r2} - q_{r1}}\left[1 - \frac{\mu_2 - \mu_1}{q_{r2} - q_{r1}}\right] + \frac{\mu_2 t_1 - \mu_1 t_2}{q_{r2} - q_{r1}}, \end{aligned} \tag{3.29}$$

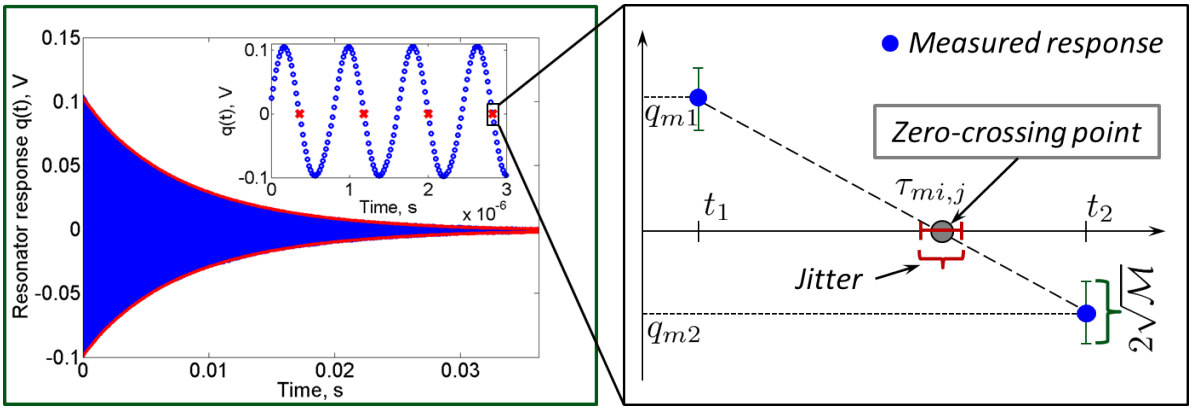

Figure 3.10: Measurement noise contribution to the jitter in the zero-crossing points in the resonator ringdown response. As expected, the resonator motion with larger amplitude is less susceptible to the effects of measurement noise, which is the fundamental necessity for high signal-to-noise ratio for precise frequency generators and clocks.

where, without loss of generality, $q_{m1} > 0$ and $q_{m2} < 0$ are the measured ringdown displacements at times t_1 and t_2, respectively, and we have assumed that the measurement noise is weak as compared with the original signal due to the resonator vibrations, i.e., $|\mu_2 - \mu_1| \ll |q_{r2} - q_{r1}|$. By introducing

$$\tau_{ri,j} = \frac{q_{r2}t_1 - q_{r1}t_2}{q_{r2} - q_{r1}} \tag{3.30}$$

as the zero-crossing point in the resonator response before a measurement is taken, Eq. (3.29) can be rewritten as

$$\begin{aligned} \tau_{mi,j} &= \tau_{ri,j} + \delta\tau_{\mu i,j}, \\ \delta\tau_{\mu i,j} &= \mu_2 \frac{t_1 - \tau_{ri,j}}{q_{r2} - q_{r1}} - \mu_1 \frac{t_2 - \tau_{ri,j}}{q_{r2} - q_{r1}}, \end{aligned} \tag{3.31}$$

where $\delta\tau_{\mu i,j}$ is the jitter induced by the measurement noise to the location of the j^{th} zero-crossing point on the i^{th} ringdown segment. Assuming the properties of μ_p described in

Eq. (3.28), the statistical properties of $\delta\tau_{\mu i,j}$ are

$$\langle \delta\tau_{\mu i,j} \rangle_j = 0, \tag{3.32a}$$

$$\langle \delta\tau_{\mu i,j} \delta\tau_{\mu i,k} \rangle_{jk} = \mathcal{M}\delta_{jk} \left[\left\langle \frac{(t_1 - \tau_{ri,j})^2}{(q_{r2} - q_{r1})^2} \right\rangle_j + \left\langle \frac{(t_2 - \tau_{ri,j})^2}{(q_{r2} - q_{r1})^2} \right\rangle_j \right]. \tag{3.32b}$$

In order to calculate the expression in the square brackets in Eq. (3.32b), we assume that the resonator-related noises only slightly perturb the resonator motion, which allows us to approximate the denominator as

$$|q_{r2} - q_{r1}| \approx a_{di}\omega_{di}(t_2 - t_1), \tag{3.33}$$

where a_{di} and ω_{di} are the resonator deterministic (averaged) amplitude and vibration frequency during the i^{th} ringdown segment. Due to the fixed sampling time and the fact that the resonator frequency, even its deterministic component (due to frequency pulling), is a function of time, we assume that the location of $\tau_{ri,j}$ on the interval $[t_1, t_2]$ is a random variable with the uniform distribution for different j's, i.e.,

$$prob(\tau_{ri,j} \in [t, t + dt]) = \frac{dt}{t_2 - t_1}, \quad \text{for} \quad t \in [t_1, t_2]. \tag{3.34}$$

The latter results in

$$\langle (t_1 - \tau_{ri,j})^2 \rangle_j = \langle (t_2 - \tau_{ri,j})^2 \rangle_j = \frac{1}{3}(t_2 - t_1)^2, \tag{3.35}$$

and we can rewrite Eq. (3.32b) as

$$\langle \delta\tau_{\mu i,j}^2 \rangle_j \approx \frac{2}{3}\frac{\mathcal{M}}{a_{di}^2 \omega_{di}^2}. \tag{3.36}$$

Once we have established the statistical properties of $\delta\tau_{\mu i,j}$, we can do the same for $\delta\mathcal{T}_\mu(i,j,k)$. In particular, from Eqs. (3.21), (3.32a) and (3.36) we have

$$\langle \delta\mathcal{T}_\mu(i,j,k) \rangle_j = 0, \tag{3.37a}$$

$$\langle \delta\mathcal{T}_\mu^2(i,j,k) \rangle_j \approx \frac{4}{3}\frac{\mathcal{M}}{a_{di}^2 \omega_{di}^2}. \tag{3.37b}$$

Note that the contribution of measurement noise to the jitter in the zero-crossing points is independent of k to leading order. As we will show in Sections 3.4.2 and 3.4.3, thermal and frequency noises result in a qualitatively different effect; in particular, their leading-order contribution to the timing jitter is proportional to k. This important difference allows us to separate measurement noise from resonator-related noise sources, as we will conclude in Section 3.4.4.

3.4.2 Resonator phase fluctuations during ringdown

It is well-known that both additive and multiplicative noise sources affect the resonator dynamics by inducing fluctuations in the resonator amplitude and phase [49, 50]. At the same time, the resonator phase is intrinsically related to time through the system vibration frequency, which serves as an effective scaling factor between these two quantities. As a result, if we use the resonator phase, or, more precisely, the phase difference, as a tool to measure time, we will measure it with a certain error due to the resonator/oscillator phase

noise. In this light, before we proceed to defining the timing jitter due to resonator phase fluctuations, we shall briefly revisit how additive and multiplicative noise sources contribute to the resonator frequency and, consequently, to phase noise. In order to illustrate these contributions, we simplify the original resonator model, described in Eq. (3.4), as follows,

$$\ddot{q} + 2\Gamma_1 \dot{q} + q(\omega_0^2 + 2\omega_0 \eta(t) + \gamma q^2) = f(t), \tag{3.38}$$

where $f(t)$ and $\eta(t)$ are additive (thermal) and multiplicative (frequency) noise sources acting on the system. The main advantage of the model in Eq. (3.38) over the one in Eq. (3.4) is the linearity of the dissipative force, which greatly simplifies the foregoing analysis. However, we shall return to the discussion of linear vs. nonlinear damping in Section 3.4.4, where we discuss the noise characterization protocol. Note that in Eq. (3.38) we have also omitted the quintic term in the resonator restoring force since this term does not change the qualitative picture of the resonator amplitude and phase fluctuations; if necessary, it can be included in a straightforward manner.

In order to analyze the resonator phase (and amplitude) fluctuations, we employ classical van der Pol transformation to the slowly-varying complex amplitude $u(t)$,

$$q(t) = u(t)e^{i\omega_0 t} + u^*(t)e^{-i\omega_0 t}, \quad \dot{q}(t) = i\omega_0[u(t)e^{i\omega_0 t} - u^*(t)e^{-i\omega_0 t}]. \tag{3.39}$$

By inserting Eq. (3.39) in Eq. (3.38) and neglecting fast-oscillating terms, we obtain the following equation of motion for $u(t)$, [49],

$$\dot{u} = -\Gamma_1 u + \frac{3i\gamma}{2\omega_0}|u|^2 u + iu\eta_0(t) - \frac{i}{2\omega_0} f_{\omega_0}(t), \tag{3.40}$$

where $\eta_0(t)$ represents the slowly-varying component of $\eta(t)$ and $f_{\omega_0}(t)$ is the slowly-varying component of $f(t)\exp(-i\omega_0 t)$. By expressing the slowly-varying complex amplitude in the polar form,

$$u = \frac{1}{2} a e^{i\phi}, \tag{3.41}$$

we can separate the resonator amplitude $a(t)$ and phase $\phi(t)$ as

$$\dot{a} = -\Gamma_1 a + \frac{1}{\omega_0}\left(f_{\omega_0}^{(i)}(t)\cos\phi - f_{\omega_0}^{(r)}(t)\sin\phi \right), \tag{3.42a}$$

$$\dot{\phi} = \frac{3\gamma}{8\omega_0} a^2 + \eta_0(t) - \frac{1}{a\omega_0}\left(f_{\omega_0}^{(r)}(t)\cos\phi + f_{\omega_0}^{(i)}(t)\sin\phi \right), \tag{3.42b}$$

where we have expressed thermal noise in the rotating frame as,

$$f_{\omega_0}(t) = f_{\omega_0}^{(r)}(t) + i f_{\omega_0}^{(i)}(t). \tag{3.43}$$

In the absence of additive and multiplicative noise sources the solution to the resonator amplitude and phase becomes

$$a_d(t) = a_0 e^{-\Gamma_1 t}, \tag{3.44a}$$

$$\phi_d(t) = \frac{3\gamma a_0^2}{16\Gamma_1\omega_0}\left(1 - e^{-2\Gamma_1 t} \right), \tag{3.44b}$$

which, of course, can be obtained from Eqs. (3.7) and (3.8) by letting $\beta = 0$ and taking the limit $\Gamma_2 \to 0$.

Next, we assume that the additive and multiplicative noise sources weakly perturb the resonator dynamics about its deterministic decay and represent their effect on the resonator

dynamics as follows,

$$a(t) = a_d(t) + \delta a(t), \tag{3.45a}$$

$$\phi(t) = \phi_d(t) + \delta\phi(t), \tag{3.45b}$$

where $\delta a(t)$ and $\delta\phi(t)$ are small ($|\delta a(t)| \ll a_d(t)$ and $|\delta\phi(t)| \ll \phi_d(t)$) perturbations to the deterministic resonator solution in Eqs. (3.44a) and (3.44b). This assumption about "smallness" of amplitude and phase fluctuations does not, of course, hold when the resonator amplitude becomes comparable with $\sqrt{\langle a_{th}^2 \rangle}$, the root-mean-square of the system thermal vibrations induced by $f(t)$. Thus, the analysis presented in this section is applicable to the initial part of the ringdown, where the resonator is far from thermal equilibrium. In this case, we can linearize Eqs. (3.42a) and (3.42b) about the noise-free solution, which yields the following equations of motion for $\delta a(t)$ and $\delta\phi(t)$,

$$\delta\dot{a} = -\Gamma_1 \delta a + \frac{1}{\omega_0}\left(f_{\omega_0}^{(i)}(t)\cos\phi_d - f_{\omega_0}^{(r)}(t)\sin\phi_d \right), \tag{3.46a}$$

$$\delta\dot{\phi} = \frac{3\gamma}{4\omega_0} a_d \delta a + \eta_0(t) - \frac{1}{a_d\omega_0}\left(f_{\omega_0}^{(r)}(t)\cos\phi_d + f_{\omega_0}^{(i)}(t)\sin\phi_d \right). \tag{3.46b}$$

In Eqs. (3.46a) and (3.46b), we assume that thermal and frequency noise sources are zero-mean random processes that are independent and uncorrelated, i.e., $\langle \eta_0(t_1) f(t_2) \rangle \equiv 0$. Additionally, we assume that the correlation time of each of these random processes to be much smaller than Γ_1^{-1}, which allows us to approximate these noise sources as delta-correlated, i.e.,

$$\langle \eta_0(t_1)\eta_0(t_2) \rangle = D_\eta \delta(t_1 - t_2), \quad \langle f(t_1) f(t_2) \rangle = D_f \delta(t_1 - t_2).$$

Using these assumptions, one can show that the thermal noise components $f_{\omega_0}^{(r)}(t)$ and $f_{\omega_0}^{(i)}(t)$ possess the following statistical properties [49],

$$\begin{aligned} \langle f_{\omega_0}^{(r)}(t)\rangle = \langle f_{\omega_0}^{(i)}(t)\rangle = 0, \quad \langle f_{\omega_0}^{(r)}(t_1) f_{\omega_0}^{(i)}(t_2)\rangle = 0, \\ \langle f_{\omega_0}^{(r)}(t_1) f_{\omega_0}^{(r)}(t_2)\rangle = \langle f_{\omega_0}^{(i)}(t_1) f_{\omega_0}^{(i)}(t_2)\rangle = \frac{D_f}{2}\delta(t_1 - t_2). \end{aligned} \tag{3.47}$$

From Eq. (3.46b) it follows that in order to calculate statistics of the resonator phase fluctuations, i.e., $\langle \delta\phi(t)\rangle$ and $\langle \delta\phi^2(t)\rangle$ (in this work we do not need the two-time correlation function $\langle \delta\phi(t_1)\delta\phi(t_2)\rangle$), we must first calculate the statistical properties of the resonator amplitude fluctuations. Fortunately, Eq. (3.46a) can be solved in a straightforward way and yields

$$\delta a(t) = \frac{1}{\omega_0}\int_0^t dt' e^{-\Gamma_1(t-t')}\left(f_{\omega_0}^{(i)}(t')\cos\phi_d(t') - f_{\omega_0}^{(r)}(t')\sin\phi_d(t')\right), \tag{3.48}$$

which, after some algebra, leads to the following expression for the resonator amplitude correlation function

$$\langle \delta a(t_1)\delta a(t_2)\rangle = \frac{D_f}{4\Gamma_1\omega_0^2}\left[e^{-\Gamma_1|t_1-t_2|} - e^{-\Gamma_1(t_1+t_2)}\right]. \tag{3.49}$$

We can now determine the statistical properties of the resonator phase. From Eqs. (3.46b) and (3.47), we have

$$\langle \delta\phi(t)\rangle = 0, \tag{3.50a}$$

$$\begin{aligned} \langle \delta\phi^2(t)\rangle &= \int_0^t dt_1 \int_0^t dt_2 \langle \delta\dot{\phi}(t_1)\delta\dot{\phi}(t_2)\rangle \\ &= D_\eta t + \frac{D_f}{4\Gamma_1\omega_0^2}\left[\frac{e^{2\Gamma_1 t}-1}{a_0^2} + \frac{9\gamma^2 a_0^2}{64\Gamma_1^2\omega_0^2}\left(1 - 4\Gamma_1 t e^{-2\Gamma_1 t} - e^{-4\Gamma_1 t}\right)\right]. \end{aligned} \tag{3.50b}$$

Equation (3.50b) shows the effects of both the additive and multiplicative noise sources on the variance of the resonator phase. As expected, the resonator frequency noise $\eta_0(t)$ results in a simple diffusion of the resonator phase. In contrast, the thermal noise contribution is more complicated, due to the non-stationary nature of the resonator ringdown response. In this work, however, we are interested in the resonator phase fluctuations on the time scale $\Delta t \ll \Gamma_1^{-1}$, in which case $\langle \delta\phi^2(t) \rangle$ can be approximated as follows,

$$\langle \delta\phi^2(t) \rangle \approx t\left(D_\eta + \frac{D_f}{2\omega_0^2 a_0^2} \right) + \frac{D_f \Gamma_1}{2\omega_0^2 a_0^2} t^2 + t^3 \left(\frac{3 D_f \gamma^2 a_0^2}{32\omega_0^4} + \frac{D_f \Gamma_1^2}{3\omega_0^2 a_0^2} \right), \tag{3.51}$$

where we have expanded all terms in Eq. (3.50b) to 3^{rd} order in t, which is necessary to illustrate the leading order effect of the resonator nonlinearity γ on the resonator phase fluctuations. From Eq. (3.51) two important conclusions can be made. First, the resonator phase variance goes to 0 as $t \to 0$, which follows from the simple fact that the resonator phase is the integral of the resonator instantaneous frequency. Second, the phase diffusion constant, defined as the coefficient of the linear term in t in Eq. (3.51), has two contributions corresponding to additive and multiplicative noise sources. Importantly, while the latter is independent of the resonator initial amplitude, the contribution of the thermal noise grows as the initial amplitude decreases. We shall return to this important difference between thermal and frequency noise sources when we discuss the noise characterization protocol in Section 3.4.4.

3.4.3 Phase noise timing jitter $\delta\mathcal{T}_r(i,j,k)$

In the previous section we have shown how resonator-related noise sources contribute to fluctuations of the resonator phase. Here we show that the phase noise $\delta\phi(t)$, in turn, causes

additional jitter, denoted $\delta\mathcal{T}_r(i,j,k)$, in the zero-crossing points, which is in addition to that caused by measurement noise, $\delta\mathcal{T}_\mu(i,j,k)$. To show this, consider the following phase difference,

$$\pi k = \phi(\tau_{ri,j+k}) - \phi(\tau_{ri,j}) = \int_{\tau_{ri,j}}^{\tau_{ri,j+k}} dt\omega_i(t) = \int_{\tau_{ri,j}}^{\tau_{ri,j+k}} dt\omega_{di}(t) + \int_{\tau_{ri,j}}^{\tau_{ri,j+k}} dt\delta\dot{\phi}_i(t), \tag{3.52}$$

where $\delta\dot{\phi}_i(t)$ represents the cumulative effect of additive and multiplicative noise sources; see Eq. (3.46b). By rearranging terms we can express the resonator phase fluctuations in the following way,

$$\begin{aligned}\delta\phi(i,j,k) = \int_{\tau_{ri,j}}^{\tau_{ri,j+k}} dt\delta\dot{\phi}_i(t) &= \pi k - \int_{\tau_{ri,j}}^{\tau_{ri,j+k}} dt\omega_{di}(t) \\ &\approx \pi k - \omega_{di}(\mathcal{T}_d(i,j,k) + \delta\mathcal{T}_r(i,j,k)),\end{aligned} \tag{3.53}$$

where we have assumed a sufficiently fine partitioning of the resonator ringdown signal, so that $\omega_{di}(t) \approx \omega_{di} = const.$ The same assumption also leads to

$$\begin{aligned}\mathcal{T}_d(i,j,k) \approx T_{di}\frac{k}{2} \quad &\rightarrow \quad \pi k \approx \omega_{di}\mathcal{T}_d(i,j,k), \\ \delta\phi(i,j,k) &\approx -\omega_{di}\delta\mathcal{T}_r(i,j,k).\end{aligned} \tag{3.54}$$

As a result, the statistical properties of $\delta\mathcal{T}_r(i,j,k)$ become

$$\begin{aligned}\langle\delta\mathcal{T}_r(i,j,k)\rangle_j &= -\omega_{di}^{-1}\langle\delta\phi(i,j,k)\rangle_j = 0, \\ \langle\delta\mathcal{T}_r^2(i,j,k)\rangle_j &= \omega_{di}^{-2}\langle\delta\phi^2(i,j,k)\rangle_j.\end{aligned} \tag{3.55}$$

Finally, using Eqs. (3.26), (3.51) and (3.55), we can express the statistical properties of the total timing jitter in the measured resonator ringdown response as

$$\begin{aligned}\langle \delta\mathcal{T}^2(i,j,k)\rangle_j &\approx \frac{4}{3}\frac{\mathcal{M}}{a_{di}^2\omega_{di}^2} + \frac{\langle \delta\phi^2(i,j,k)\rangle_j}{\omega_{di}^2} \\ &\approx \frac{4}{3}\frac{\mathcal{M}}{a_{di}^2\omega_{di}^2} + \frac{\pi k}{\omega_{di}^3}\left(D_\eta + \frac{D_f}{2\omega_{di}^2 a_{di}^2}\right), \quad \text{for} \quad \frac{\pi k}{\omega_{di}} \ll \Gamma_1^{-1},\end{aligned} \tag{3.56}$$

where we have, in the spirit of the ringdown partitioning, discretized time t in Eq. (3.51) as $\pi k/\omega_{di}$ and retained only the lowest-order (in k) term describing the temporal evolution of the variance of the measured time intervals $\mathcal{T}(i,j,k)$, which is due to the presence of noises $\mu(t), f(t)$ and $\eta(t)$.

3.4.4 Noise characterization protocol

In this section we summarize our understanding of how thermal, frequency, and measurement noise sources affect the resonator ringdown response, obtained in Sections 3.4.1 to 3.4.3, and formulate the noise characterization protocol using Eq. (3.56) as the central result. First, as follows from Eq. (3.56), the measurement and additive noise contributions to the timing jitter depend on the resonator vibration amplitude. Thus, by partitioning the resonator ringdown response into N segments of time length Δt, we effectively obtain several ringdown sub-measurements that have different initial amplitudes and vibration frequencies, where each is assumed to be essentially constant over each segment. Next, within the i^{th} segment of the ringdown response ($i = \overline{1:N}$), we calculate the number of time intervals $\mathcal{T}(i,j,k)$ that it takes for the resonator to accumulate πk radians of phase or, equivalently, to perform k half-cycles; see Fig. 3.11.

These collected time intervals are then analyzed statistically and the the variance $\langle \delta\mathcal{T}^2(i,j,k)\rangle_j$

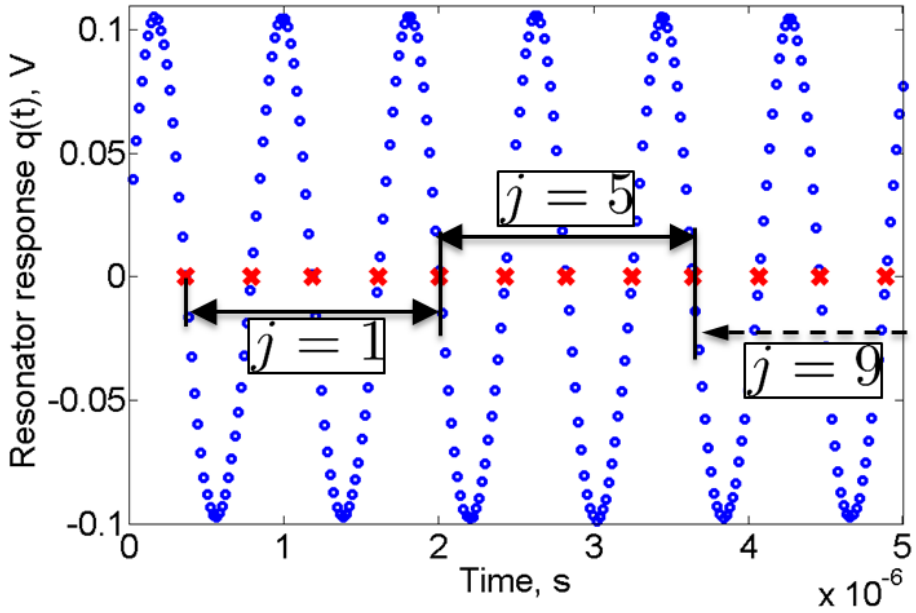

Figure 3.11: Time intervals $\mathcal{T}(1, j, 4)$ calculated within the 1^{st} ringdown segment. Due to the presence of measurement, thermal, and frequency noises, these time intervals slightly differ in length, which, when analyzed statistically, allows one to reveal these noise sources and estimate their intensities.

is calculated. Here it is important to note that the ringdown partitioning should be done in a way that ensures statistical sufficiency for $\mathcal{T}(i, j, k)$ with different values of k. For instance, the DA-DETF resonator used in this study has a quality factor $Q \approx 10^4$. Partitioning the ringdown into $N = 50$ segments results in each segment having ≈ 200 full cycles, or ≈ 400 zero-crossing points. From a statistical point of view, this means that we have enough zero-crossing points to calculate time intervals $\mathcal{T}(i, j, k)$ for $k = \overline{1:40}$ and reconstruct the $\langle \delta\mathcal{T}^2(i, j, k) \rangle_j$ function. This function, as follows from Eq. (3.56), has a constant contribution due to the measurement noise, and a $k-$dependent part that is due to the thermal and frequency noises; see Fig. 3.12. The non-vanishing contribution to the jitter in the zero-crossing points is the signature of measurement noise and can therefore be used for separating out the effects of measurement noise and estimating its intensity $\mathcal{M}$. In particular, the measurement noise intensity can be estimated by plotting the constant

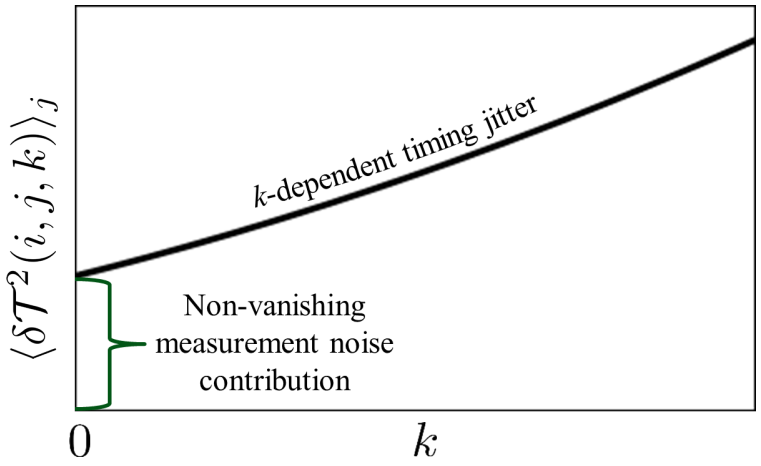

Figure 3.12: Qualitative behavior of $\langle \delta \mathcal{T}^2(i,j,k) \rangle_j$ as a function of k within the i^{th} ringdown segment. Importantly, the measurement noise contribution to the timing jitter does not vanish as $k \to 0$, which is used for estimating the measurement noise intensity $\mathcal{M}$. In contrast, the corresponding contributions of thermal and frequency noise sources to the timing jitter are both $k-$dependent, but have different magnitudes in different ringdown regimes due to their differing amplitude dependence.

term in $\langle \delta \mathcal{T}^2(i,j,k) \rangle_j$, extracted from the ringdown segments, as a function of the resonator amplitude, and fitting the resulting curve with the power law form given in Eq. (3.56); see Fig. 3.13a.

Next, by fitting the $k-$dependent part of $\langle \delta \mathcal{T}^2(i,j,k) \rangle_j$ with a polynomial of 3^{rd} order, for sufficiently small k, and isolating the term $\propto k$, we can extract the resonator phase diffusion constant determined by the intensities of thermal and frequency noise sources. As mentioned above, the thermal noise contribution to the resonator phase fluctuations and, consequently, the timing jitter, are both amplitude-dependent, while the associated contribution of frequency noise is independent of the resonator amplitude. This difference between thermal and frequency noise sources allows us to independently estimate the intensities of additive, D_f, and multiplicative, D_η, noise sources by comparing the phase diffusion constant, extracted from multiple ringdown segments, against the analytical prediction from Eq. (3.56); see Fig. 3.13b. Following this noise measurement protocol, we have estimated

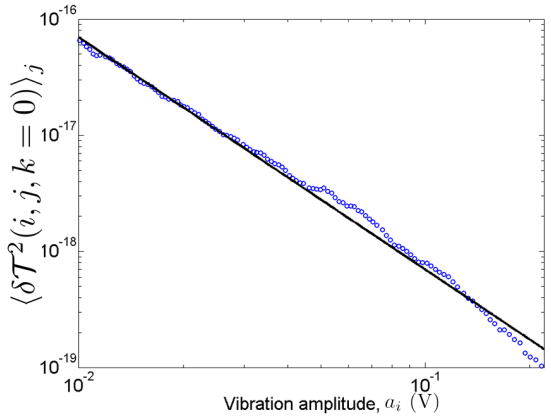

(a) Extracted non-vanishing contribution of measurement noise to the timing jitter as a function of the resonator amplitude (from different ringdown segments). Discrete dots represent extracted contributions of measurement noise to the timing jitter, while the solid line is the least-squares fit with the model in Eq. (3.56).

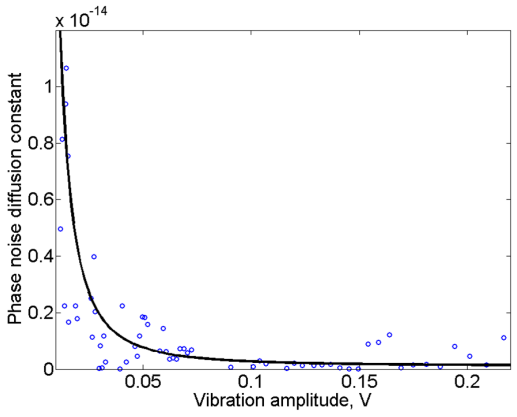

(b) Behavior of the leading-order $k-$dependent part of $\langle \delta \mathcal{T}^2(i,j,k) \rangle_j$ as a function of the resonator amplitude along the measured ringdown response. Discrete dots represent extracted contribution of measurement noise to the timing jitter, while th solid line is the least-square fit with the model in Eq. (3.56).

Figure 3.13: Characterization of measurement, thermal and frequency noise sources.

the intensities of measurement, additive, and multiplicative noise sources for the DA-DETF resonator under study, and the results are presented in Table 3.3.

Fig. 3.13a illustrates both qualitative and quantitative agreement of the model with the experimentally obtained data, and there is a good qualitative agreement between the theoretical and experimental results in Fig. 3.13b. There does exist a quite noticeable spread of experimental results around the fitted curve in Fig. 3.13b, which is believed to be due to two factors: First, measurement noise, if it is not weak, can contribute to the term $\propto k$ in Eq. (3.56), and this effect has not been accounted in the present work. Second, the effects of thermal and frequency noise is of higher-order, as compared with the measurement noise contribution, which makes the characterization procedure for these noise sources more sensitive to the ringdown partitioning, thereby affecting the the accuracy of extracting the coefficient of the term $\propto k$.

Table 3.3: Extracted intensities of the measurement, frequency, and thermal noise sources. Thermal noise intensity D_f is expressed in terms of the root-mean-square of the resonator vibration amplitude in thermal equilibrium: $D_f = 4\Gamma_1\omega_0^2\langle\delta a^2\rangle_{th}$. Noise characterization was performed in five independent ringdown measurements at $V_{DC} = 30\ V$ and $T = -40^\circ\ C$ with initial amplitude $a_0 = 265\ mV$.

Ringdown	$\sqrt{\mathcal{M}},\ mV$	$D_\eta,\ Hz$	$\sqrt{\langle\delta a^2\rangle_{th}},\ mV$
1	0.64	6×10^{-3}	0.68
2	0.63	12×10^{-3}	0.58
3	0.64	5.1×10^{-3}	0.58
4	0.63	6.7×10^{-3}	0.65
5	0.63	5.4×10^{-3}	0.75

3.5 Outlook

In this chapter we have introduced a comprehensive method that allows one to characterize many important model parameters for MEMS resonantors using transient ringdown measurements. A very important advantage of this characterization method is that the electronics that are responsible for the resonator drive do not affect the ringdown process and, as a result, do not contribute uncertainties to the characterization process.

In terms of deterministic model parameters, we have illustrated how to extract deterministic stiffness and damping parameters for the symmetric vibrational mode of a MEMS using a single ringdown measurement. These include values of linear and nonlinear (cubic) friction coefficients, obtained from the shape of the vibration amplitude envelope, as well as the modal natural frequency and conservative Duffing and quintic stiffness nonlinearities, obtained using the zero-crossing times in the ringdown. A key to the method is that the vibrational amplitude is affected only by the dissipation parameters, while the frequency and phase are affected by the resonator conservative parameters, thereby uncoupling this part of the characterization process. Furthermore, we have developed a novel technique for direct

revelation of measurement, thermal, and frequency noise sources by performing a statistical analysis on the zero-crossing points. We showed that these noise sources have qualitatively different signatures on the resonator timing jitter and that by considering specific features of the jitter, one is able to estimate the intensities of these noise sources.

The methods for determining both deterministic and noise parameters were successfully tested on resonator data provided by collaborators at Stanford. The estimation of deterministic parameters was very successful. The estimation of noise intensities was very promising, but corrupted by relatively strong measurement noise.

Future work in this area includes development of techniques for systems with asymmetric nonlinearities, further testing of the technique on data with less measurement noise, and extension of the method to account for more information about the noise sources.

Chapter 4

Improving the sensitivity of MEMS ring/disk resonating gyroscopes

In this chapter we examine the self-induced parametric amplification in MEMS ring and disk resonating gyroscopes and describe how this nonlinear phenomenon affects the performance of these gyroscopes when employed as angular rate sensors. Studies of the linear and nonlinear vibrations of systems with circular symmetry has a long history relevant to this problem, and it includes papers on the transverse vibration of plates, shells, membranes, rods, and tubes as well as the in-plane vibrations of plates and rings; see [100–103] and the research cited therein for a sampling of these works. This class of systems has applications in a number of areas including vibrations of antennae, pipes, and, most relevant to the present work, wine glass vibratory gyroscopes that use Coriolis effects to measure spin rates [104, 105].

In recent decades there has been a desire to develop smaller versions of these rate sensors, spurred by technological advancements in fabrication techniques and by increasing demands in commercial and military applications, and this has led to a number of important advances in this technology [100, 106, 107]. Prominent among these are developments in MEMS vibratory gyroscopes, which have shown great potential due to their small dimensions, favorable power consumption, and high quality factors [108, 109]. Generally, such devices are based on a micro-mechanical resonator with at least two matched resonant modes that interact via

Coriolis effects [105], as follows: the resonator is forced to oscillate in one of its vibrational modes, called *the drive mode*, and an external rotation at Ω gives rise to Coriolis coupling between this mode and its symmetric partner, *the sense mode*, which is not driven by an external input. The response of the sense mode thus has an amplitude proportional to Ω (at least when it is small compared to the vibration frequency), so that by calibrating and measuring the amplitude of the readout signal from the sense mode, one can estimate Ω.

Improving the precision and accuracy of MEMS vibratory gyroscopes involves several challenging tasks including the precise matching of high-Q modal frequencies [38, 110, 111], compensation of quadrature errors that arise from coupling of the drive and sense modes [112–114], and optimizing the geometry of the resonator in order to achieve high Q factors [115, 116], to name a few. Also, all such devices are generally operated in the linear operating regime, so as to avoid frequency shifts associated with nonlinearity. In this light, flexural-mode ring [19, 112] and disk [117–119] vibratory gyroscopes offer significant advantages due to the inherent symmetry in their geometries and, consequently, symmetry of their drive and sense modes. Recent work on disk resonating gyroscopes (DRGs) has experimentally demonstrated that the gyroscope sensitivity to the external angular rate can increase significantly when the gyroscope is driven into a nonlinear operating regime [27]. The authors hypothesized that the observed phenomenon is due to parametric amplification [120–122] arising from nonlinear elastic coupling between the drive and sense modes of the device, which have nearly equal frequencies. In classical nonlinear vibrations, this is an example of *autoparametric resonance* [123–125].

The sensitivity S of a rate gyroscope, that is, the ratio of the amplitude of the sense signal to the angular rate Ω, is one the most important characteristics of sensor performance, since it, and the noise levels of the device, quantify the resolution of the sensor in terms of

the lower end of the angular velocities that can be detected [105]. Thus, there is strong motivation to understand, from a fundamental point of view, the advantageous effects of the self-induced amplification of the sense signal observed in [27], especially since it appears to be the fortuitous result of passive nonlinear behavior, requiring no additional sensing or energy source. Understanding and taking full advantage of this and other nonlinear effects are the main goals of the investigation described in this chapter.

Nonlinear modal coupling is a well-known phenomenon in the theory of nonlinear vibrations and it has been thoroughly studied in a wide variety of systems [65], including micromechanical systems [76, 126–128]. It generally occurs in resonators experiencing vibration amplitudes at which nonlinear strain-displacement relationships, or other nonlinear effects, couple two or more vibrational modes. This coupling has its most dramatic effects when the coupled modes have commensurate frequencies and are lightly damped, which promotes resonant interactions between the modes.

Specific research on the nonlinear vibrations of spinning ring-like geometries has illustrated the rich dynamics associated with the in-plane flexural modes of these structures [129–132]. Here we analyze the dynamic behavior of the elliptical modes in ring/disk resonating gyroscopes to explain and explore self-induced parametric amplification that has been experimentally observed in these systems [27]. In particular, we use a model of the resonator consisting of a thin ring spinning about its axis of radial symmetry, considering both mechanical effects as well as electrostatic forces arising from capacitive actuation/sensing schemes. Using finite deformation kinematics, we show that the elliptical drive and sense modes are nonlinearly coupled through both stiffness (including electrostatic contributions) and inertial terms. Next, we show that the general case of mode-coupled dynamics can be simplified by neglecting the back-action of the sense mode motion on the drive mode (due

to their differing amplitudes), and provide conditions for which this approximation holds. In this simplified picture, we discuss the effects of inertial nonlinearities on the drive mode dynamics and show how nonlinear modal interactions lead to parametric amplification of the sense mode, and thus to an increase in the gyroscope sensitivity. Additionally, we examine several methods one can utilize in order to manipulate gyroscope nonlinearities, including the important intermodal coupling strength and the modal Duffing constant, for improving the rate sensor performance. Modal coupling strength determines the level of parametric amplification one can expect for a given operating amplitude of the drive mode, while the Duffing nonlinearity is the key parameter determining the upper limit of the gyroscope dynamic range, specifically for the drive mode in this application. In this light, using our model of a thin spinning ring, we illustrate how clever design of the gyroscope and electrostatic tuning can be used for maximizing the strength of the nonlinear modal coupling, or minimizing individual modal Duffing nonlinearities, and optimizing their combined effects.

The remainder of the chapter is organized as follows. In Section 4.1, we formulate a model for resonator geometries that support a pair of degenerate (equal frequency) $n = 2$ (n is the modal wave number) radial modes and provide main theoretical concepts used in the subsequent analysis. In Section 4.2 we consider the nonlinear in-plane flexural vibrations of a thin spinning ring in the presence of electrostatic actuation. Specifically, Section 4.2.1 contains a step-by-step derivation of governing equations of motion for the gyroscopic drive and sense modes. A detailed analysis of the dynamic behavior of the drive and sense modes is given in Sections 4.2.2 and 4.2.3, respectively. In Section 4.2.4 we illustrate the applicability of our results to a model of the representative ring resonating gyroscope reported in [19]. Finally, in Section 4.3 we consider shape optimization techniques and electrostatic tuning methods that can be used to manipulate the modal coupling strength and the Duffing

nonlinearity and, as a result, opitmize its dynamic behavior. Concluding remarks for the chapter are given in Section 4.4.

4.1 General dynamical model

In this section we present an analytical framework which can be used to derive equations of motion for the in-plane vibration modes of interest for ring/disk resonating gyroscopes. Such a formulation is advantageous since it can be applied to systems with relatively simple geometries, such as a thin ring or a solid circular plate, as well as to MEMS gyroscopes with less trivial geometries; see, for example, [133]. We start our analysis by introducing a cylindrical coordinate system (r, θ, z) and consider a gyroscope with generic geometry that supports a pair of degenerate elliptical modes each of which has two nodal diameters, which we denote with modal coordinates A and B and mode shapes described by $\Xi_A(r,\theta) = \xi(r)\cos 2\theta$ and $\Xi_B(r,\theta) = \xi(r)\sin 2\theta$, so that their nodal diameters are separated by $\pi/4$ [27]. Without loss of generality, we designate these as the drive (A) and sense (B) modes, respectively.

During gyroscope operation, the resonator configuration is described by displacements in the radial, $u = u(r,\theta,t)$, and circumferential, $v = v(r,\theta,t)$, directions, which we assume to be independent of the out-of-plane coordinate z. These displacements can be expressed in terms of the modal coordinates $A(t)$ and $B(t)$ in a manner that depends on the gyroscope geometry, as $u = u(r,\theta,A(t),B(t))$ and $v = v(r,\theta,A(t),B(t))$. Generally, both u and v can be nonlinear in $A(t)$ and $B(t)$. Explicit expressions for $u(r,\theta,A(t),B(t))$ and $v(r,\theta,A(t),B(t))$ can be obtained with certain assumptions for relatively simple structures like a thin ring, see Section 4.2, or a solid circular plate [101,134,135], while in the case of non-trivial geometries,

computing similar expressions generally requires the use of finite element methods.

In this work we utilize Lagrange's method to derive the equations that govern the drive and sense modes of the gyroscope, using generalized coordinates $q_{1,2} = A, B$ to express the nonlinear equations of motion for the gyroscopic elliptical modes. The kinetic energy of the system is computed using standard methods [95, 134] and is given by

$$T = \frac{1}{2}\iiint_V \rho[(\dot{u} - v\Omega)^2 + (\dot{v} + (r+u)\Omega)^2] r dr d\theta dz, \tag{4.1}$$

where Ω is the external angular rate about the $z-$axis, $\rho = \rho(r, \theta)$ is the resonator material mass density, which is assumed to be uniform in z, and V is the volume of the resonator body. The potential energy of the gyroscope consists of elastic U_d and electrostatic U_e components. The electrostatic part results from electrostatic interaction of the resonator body with the drive/sense electrodes. Generally, the electrode gap size Δ is much smaller that the outer radius of the resonator R_o and the z thickness of the resonator, so that one can neglect the curvature of the electrodes and apply a local parallel-plate approximation. We also assume that Δ is uniform along the gyroscope circumference. In this case, the electrostatic potential energy becomes

$$U_e = -\frac{\epsilon_0}{2}\int_0^{2\pi} d\theta b(R_o, \theta) R_o \frac{(V_{DC} + V_{AC}(\theta))^2}{\Delta - u(R_o, \theta)}, \tag{4.2}$$

where $b(R_o, \theta)$ is the z thickness profile of the gyroscope body along its circumference, V_{DC} and V_{AC} represent magnitudes of the bias and periodic voltages used for the electrostatic actuation and sensing and $\epsilon_0 = 8.85 \times 10^{-12}\ F/m$ is the vacuum permittivity.

Mechanical deformations of the resonator body and the associated stresses contribute to the elastic potential energy in the form of a deformation potential U_d. For in-plane

vibrations, U_d can be expressed, [134],

$$U_d = \frac{1}{2}\iiint_V (\sigma_{rr}\epsilon_{rr} + \sigma_{\theta\theta}\epsilon_{\theta\theta} + \sigma_{r\theta}\epsilon_{r\theta}) r dr d\theta dz, \tag{4.3}$$

where $\epsilon_{ij} = \epsilon_{ij}(u, v)$ and $\sigma_{ij} = \sigma_{ij}(u, v)$ are the strain and stress in the body. Hooke's law establishes the well-known relationships between these quantities,

$$\begin{aligned} \sigma_{rr} &= E^*(\epsilon_{rr} + \nu\epsilon_{\theta\theta}), \\ \sigma_{\theta\theta} &= E^*(\epsilon_{\theta\theta} + \nu\epsilon_{rr}), \\ \sigma_{r\theta} &= G\epsilon_{r\theta}, \end{aligned} \tag{4.4}$$

where $E^* = E(1-\nu^2)^{-1}$ and G are the effective normal and shear moduli, respectively. In order to analyze the nonlinear dynamic behavior of the gyroscopic radial modes, one necessarily has to account for higher-order terms in the strain tensor $\epsilon_{ij}(u, v)$. Using finite deformation theory (see Appendix C) one can show that the nonlinear strain-displacement relationships, up to second order in u and v, are given by

$$\epsilon_{rr} = \frac{\partial u}{\partial r} + \frac{1}{2} r^2 \left(\frac{\partial}{\partial r} \frac{v}{r} \right)^2, \tag{4.5a}$$

$$\epsilon_{\theta\theta} = \frac{u}{r} + \frac{\partial v}{r\partial\theta} + \frac{1}{2}\left(\frac{\partial u}{r\partial\theta} \right)^2 + \frac{u}{r}\frac{\partial v}{r\partial\theta}, \tag{4.5b}$$

$$\epsilon_{r\theta} = \frac{\partial v}{\partial r} + \frac{\partial u}{r\partial\theta} - \frac{v}{r} - \frac{uv}{r^2} - \frac{u}{r}\frac{\partial u}{r\partial\theta} - \frac{\partial u}{r\partial\theta}\frac{\partial v}{r\partial\theta} + \frac{v}{r}\frac{\partial u}{\partial r} + \frac{u}{r}\frac{\partial v}{\partial r} - \frac{\partial u}{\partial r}\frac{\partial v}{\partial r}. \tag{4.5c}$$

Since the resonator displacements u and v are functions of the modal coordinates A and B, the Lagrangian for the system becomes, after integration over the resonator volume, $L = L(A, B, \dot{A}, \dot{B})$. By substituting this form of L into Lagrange's equations, one can

immediately obtain equations of motion for the gyroscopic elliptic modes of interest. In Section 4.2 we apply this procedure to a simple model of a thin inextensible ring, which, as we show, is sufficient to demonstrate the self-induced amplification phenomenon, and, fortunately, is amenable to detailed analysis. As noted above, this analytical approach is sufficiently general to be used for analyzing gyroscopes with different geometries, such as rings with supporting spring elements [19], circular plates of non-uniform thickness in the $z-$direction, and other complex geometries, so long as they have similar circular symmetry [27, 133].

4.2 Non-linear forced vibrations of a thin spinning ring

4.2.1 Gyroscope dynamics with fully-coupled modes

We apply the general formulation of Section 4.1 for analysis of the nonlinear in-plane vibrations of the elliptical modes of a uniform (ρ, b, h, and Δ are constants) circular ring rotating at a constant speed Ω about the $z-$axis in the presence of electrostatic forces from electrodes, as depicted in Fig. 4.1. Hereafter, we employ a thin ring approximation, i.e., $h \ll R$, where h and R are the ring radial thickness and its mid-line radius, respectively. In this case we can apply results for the vibrations of shallow shells [134], and neglect the stress in the radial direction, $\sigma_{rr} = 0$, as well as the shear stress, $\sigma_{r\theta} = 0$. The application of these assumptions in Eq. (4.4) yields $\sigma_{\theta\theta} = E\epsilon_{\theta\theta}$, which is the same expression as that for the longitudinal stress/strain relationship for the transverse bending of an Euler-Bernoulli beam. Following the bending theory for thin shells, we express the radial and circumferential

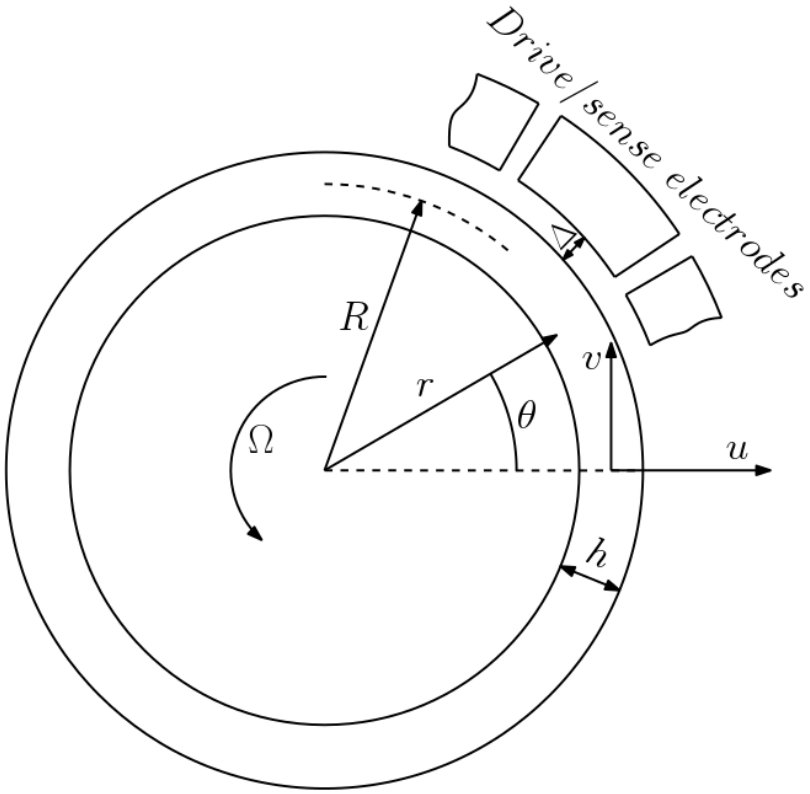

Figure 4.1: Schematic representation of the system under study: a uniform circular ring rotating at a constant angular rate Ω about the $z-$axis with segmented electrodes representing the means for electrostatic actuation and readout. Segmentation of electrodes is an essential feature of the device, necessary for producing spatially-dependent driving forces through $V_{AC}(\theta, t)$, and for tuning the gyroscopic drive and sense modes via a non-uniform distribution of the bias voltages $V_{DC}(\theta)$ [27].

displacements of any point of the ring as

$$\begin{aligned} u(r, \theta, t) &= u(\theta, t), \\ v(r, \theta, t) &= v_0(\theta, t) + \delta v_1(\theta, t), \end{aligned} \tag{4.6}$$

where $\delta = r - R$ is the radial coordinate relative to the ring mid-line, v_0 is the circumferential displacement of a point on the ring mid-line, and v_1 is the slope of the tangential displacement profile across h. Similar to v, we approximate the strain field in the θ direction as a linear function of δ, i.e., $\epsilon_{\theta\theta} = \epsilon_{\theta\theta}^{(0)} + \delta\epsilon_{\theta\theta}^{(1)}$, where $\epsilon_{\theta\theta}^{(0)}$ represents the mid-line stretching of the

ring, while $\epsilon_{\theta\theta}^{(1)}$ represents the strain due to ring bending. It is known that the ring mid-line stretching has a negligible effect on the ring dynamics, so long as the wavelength of the vibration mode is large as compared with its thickness h [129, 134, 136]. Since we are interested in the dynamic behavior of elliptical ($n = 2$) gyroscopic modes, this condition is satisfied for a thin ring. Therefore, to simplify the analysis, we make the reasonable assumption that the ring is inextensible along its mid-line, so that $\epsilon_{\theta\theta}^{(0)} = 0$.

Applying these assumptions, we can write the elastic potential energy of the resonator body as,

$$U_d = \frac{EI}{2R^3} \int_0^{2\pi} d\theta \left[u + \frac{\partial^2 u}{\partial \theta^2} - \frac{1}{2R} \left(\frac{\partial u}{\partial \theta} \right)^2 \right]^2, \tag{4.7}$$

where $I = bh^3/12$ is the second moment of area of the ring cross-section [95].

Considering U_e for this geometry, we assume that radial ring deflections are small compared to the gap size, $u \ll \Delta$, which is frequently the case for capacitively-driven MEMS resonators. Using this assumption we obtain the approximate expression for the electrostatic contribution to the system potential energy

$$U_e \approx -\frac{\epsilon_0 bR}{2\Delta} \sum_{n=0}^{4} \int_0^{2\pi} d\theta (V_{DC} + V_{AC}(\theta, t))^2 \frac{u^n(\theta, t)}{\Delta^n}, \tag{4.8}$$

where we have expanded the denominator up to the fourth order in u/Δ in order to consistently include nonlinear terms in U_e and U_d. Note that in practice the electrodes are only on the outside of the ring, which results in a slight expansion of the ring in its radial direction. However, in light of our assumption that the ring is inextensible, we neglect this correction in our analysis.

In the case of the thin ring, the mode shapes for the elliptical modes become independent

of r and are given by $\Phi_A(\theta) = \cos 2\theta$ and $\Phi_B(\theta) = \sin 2\theta$, Fig. 4.2. Using these mode shapes,

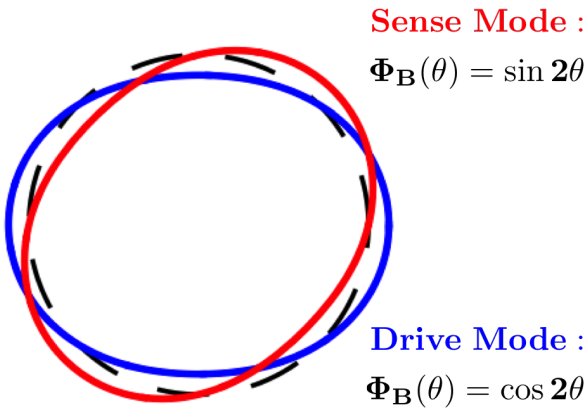

Figure 4.2: Degenerate elliptical modes of the uniform circular ring under study.

we can express the radial deflection of the ring body as

$$u(\theta, t) = A(t) \cos 2\theta + B(t) \sin 2\theta + C(t), \tag{4.9}$$

where the time-dependent function $C(t)$ is included in order to ensure periodicity of $v(\theta, t)$ in θ under the inextensibility condition [129, 131]. Note that the expression for $C(t)$ is obtained by solving $\epsilon^{(0)}_{\theta\theta} = 0$, see Eq. (4.5b), and has the form $C(t) \approx -(A^2 + B^2)/R$. We use this form for the radial displacement, and assume that the spatial distribution of the oscillating actuation voltage across the electrodes is the same as that of the drive mode, that is, $V_{AC}(\theta, t) = V_{AC}(t) \cos 2\theta$, with $|V_{AC}(t)| \ll V_{DC}$. [1] We also assume that the electrode gap is small compare to the size of the device, $\Delta \ll R$. Under these assumptions, Lagrange's method is applied using the kinetic energy in Eq. (4.1) and the potential energy $U = U_e + U_d$, resulting in nonlinear equations of motion governing the $n = 2$ elliptical modes of the ring. After dividing through by the modal mass for the thin ring, $m_{A,B} = (5/4)\pi\rho bhR$, these

[1] This assumption is convenient but not necessary, since a general distribution can be projected onto the modes of interest.

equations take the form

$$\begin{aligned}
&\ddot{A}\left[1+\frac{3}{5R^2}(11A^2+B^2)\right]+\dot{A}\left[2\Gamma_A+\frac{6}{5}\frac{B\dot{B}}{R^2}\right]\\
&+A\left[\omega_0^2+\Omega^2\left(\frac{11}{5}-\frac{37}{10}\frac{B^2}{R^2}\right)+\kappa\frac{B^2}{R^2}+\frac{33}{5}\frac{\dot{A}^2}{R^2}+\frac{31}{5}\frac{\dot{B}^2}{R^2}+\frac{34}{5}\frac{B\ddot{B}}{R^2}\right] \qquad (4.10a)\\
&+\frac{A^3}{R^2}\left[\gamma-\frac{33}{10}\Omega^2\right]-\frac{16}{5}\frac{\dot{B}}{R^2}\Omega A^2=\frac{8}{5}\Omega\dot{B}\left(1-2\frac{B^2}{R^2}\right)+F_A(A,B,t),\\
&\ddot{B}\left[1+\frac{3}{5R^2}(11B^2+A^2)\right]+\dot{B}\left[2\Gamma_B+\frac{6}{5}\frac{A\dot{A}}{R^2}\right]\\
&+B\left[\omega_0^2+\Omega^2\left(\frac{11}{5}-\frac{37}{10}\frac{A^2}{R^2}\right)+\kappa\frac{A^2}{R^2}+\frac{33}{5}\frac{\dot{B}^2}{R^2}+\frac{31}{5}\frac{\dot{A}^2}{R^2}+\frac{34}{5}\frac{A\ddot{A}}{R^2}\right] \qquad (4.10b)\\
&+\frac{B^3}{R^2}\left[\gamma-\frac{33}{10}\Omega^2\right]-\frac{16}{5}\frac{\dot{A}}{R^2}\Omega B^2=-\frac{8}{5}\Omega\dot{A}\left(1-2\frac{A^2}{R^2}\right)+F_B(A,B,t),
\end{aligned}$$

where

$$\begin{aligned}
\omega_0^2=\frac{1}{5\rho}\left(3\frac{Eh^2}{R^4}-4\frac{\epsilon_0V_{DC}^2}{h\Delta^3}\right),\quad \gamma=\kappa=\frac{6R^2}{5\rho}\left(\frac{Eh^2}{R^6}-\frac{\epsilon_0V_{DC}^2}{h\Delta^5}\right),\\
F_A(A,B,t)=\frac{\epsilon_0V_{AC}(t)V_{DC}}{5\rho h\Delta^2}\left(4+\frac{3B^2}{\Delta^2}+\frac{9A^2}{\Delta^2}\right), \qquad (4.11)\\
F_B(A,B,t)=\frac{\epsilon_0V_{AC}(t)V_{DC}}{5\rho h\Delta^4}AB.
\end{aligned}$$

Here ω_0 is the natural frequency of the modes, γ is the effective modal Duffing coefficient, and κ is the strength of the intermodal dispersive coupling, all of which account for both elastic and electrostatic stiffnesses and are normalized by the modal mass. Note that coefficients κ and γ are equal for the thin ring, but we keep their designation distinct since they have different effects on the system response and may differ for other geometries. Terms F_A and F_B represent the time-periodic excitation acting on the drive and sense modes, respectively, and note that the drive mode has both direct and (nonlinear) parametric components, while the sense mode is driven in a purely nonlinear parametric manner, since the excitation is taken to be perfectly aligned with the (linear) drive mode. The nonlinear terms in the modal forces $F_{A,B}$ result from the nonlinear treatment of the electrostatic potential energy. In order

to complete the model, we have introduced phenomenological linear dissipation coefficients Γ_A and Γ_B for the modes. The analysis of Eqs. (4.10a) and (4.10b) in their full form is quite challenging, due to the fact that the equations are nonlinear and coupled through multiple terms, including elastic, inertial, and even the external driving terms; see Eq. (4.11).

In order to obtain further insight into the gyroscope dynamics and obtain a better understanding of the self-induced amplification phenomenon, we use the fact that the drive mode is directly driven to an amplitude that is much larger than the amplitude that will be experienced by the sense mode. In fact, the sense mode is driven by the vibrations of the drive mode through the Coriolis term proportional to $\Omega\dot{A}$ (the first term on the right hand side of Eq. (4.10b)), and also parametrically through coupling terms like $\kappa BA^2/R^2$.In this case the relative phase between these two terms is $\pi/4$, which indicates, following the analysis in [120], that the sense mode response will be amplified by the drive mode vibrations regardless of their amplitude. When the parametric drive is weak enough, meaning that A is sufficiently small, the response of the sense mode due to the Coriolis effect remains stable and these parametric terms can amplify or attenuate the sense mode response, depending on the relative phase between the direct and parametric drives [121, 122, 137]. Consequently, if the gyroscope is exposed to angular rates that satisfy $\Omega \lll \omega_0$ (all rate gyros are so designed), we can assume that the sense mode operates in its linear range well below the onset of nonlinearity. Note that $\Omega \lll \omega_0$ also allows us to neglect terms proportional to Ω^2 in Eqs. (4.10a) and (4.10b). In contrast, the gyroscopic drive mode can operate at amplitudes where nonlinear effects come into play. In fact, this must be the case in order to achieve the desired amplification of the sense mode. Under these conditions, the back action of the sense mode on the drive mode can be neglected, and we can analyze the dynamics of the drive mode independently. After obtaining the (nonlinear) solution for the drive mode, we can

analyze the response of the gyroscopic sense mode and study the self-induced amplification and associated increase of the gyroscope sensitivity. In essence, we can employ a model with one-way coupling for sufficiently low Ω.

4.2.2 Dynamics of the Drive Mode

Here we study the dynamic behavior of the drive mode of the ring and analyze the effects of inertial nonlinearities and nonlinear forcing terms on its behavior. Using the assumptions derived above, we neglect coupling to the sense mode in Eq. (4.10a) and assume relatively slow external rotation, $\Omega \lll \omega_0$, to obtain the following nonlinear model for the drive mode behavior

$$\ddot{A}\left(1+\mu\frac{A^2}{R^2}\right)+2\Gamma_A\dot{A}+A\left(\omega_A^2+\mu\frac{\dot{A}^2}{R^2}+\gamma\frac{A^2}{R^2}\right)=F\cos(\omega t+\phi_F)\left(1+C_{FA}\frac{A^2}{\Delta^2}\right), \quad (4.12)$$

where μ is the strength of the inertial nonlinearity and C_{FA} represents the nonlinear correction to the modal forcing. Additionally, the drive frequency is near the modal natural frequency, that is, $\omega = \omega_A + \delta\omega$ with $\delta\omega \ll \omega_A$. Note that in Eq. (4.12) we keep all coefficients in a generic form to keep the formulation general, but apply the results for the ring geometry below.

In order to analyze Eq. (4.12), we note that the system is lightly damped (typical damping ratios are in the range $10^{-5} - 10^{-4}$), resonantly driven, and has cubic stiffness and inertial nonlinearities, so the problem is treated in the standard way. We start by representing the modal displacement in the form $A(t) = a(t)R\cos(\omega t + \phi_A(t))$, where $(a(t), \phi_A(t))$ are the non-dimensional vibration amplitude and the phase of the drive mode response. By employing the method of averaging [89], we assume that $(a(t), \phi_A(t))$ change slowly over

times $\sim \omega_A^{-1}$ and let $\dot{A}(t) \approx -\omega a(t) R \sin(\omega t + \phi_A(t))$. By using these expressions for $A(t)$ and $\dot{A}(t)$ in Eq. (4.12) and disregarding fast-oscillating terms, we obtain equations governing (a, ϕ_A) on the slow time scale $\sim \Gamma_A^{-1}$. The steady-state responses found from these equations can be solved to obtain the following expression that relates drive mode response amplitude to the system and input parameters,

$$\delta\omega(a) \approx \frac{\frac{3a^2}{8\omega_A}\left(\gamma - \frac{2}{3}\mu\omega_A^2\right)}{1 - \frac{1}{4}\mu a^2} \pm \frac{\left|\frac{4\Delta^2 + 3C_{FA}a^2R^2}{4\Delta^2 + 1C_{FA}a^2R^2}\right| \sqrt{\frac{F^2(4\Delta^2 + C_{FA}a^2R^2)^2}{8a^2R^2\Delta^4\omega_A^2} - \Gamma_A^2}}{1 - \frac{1}{4}\mu a^2}. \tag{4.13}$$

As expected, the nonlinear forcing term does not affect the shape of the modal backbone curve, represented by the first term in Eq. (4.13), but alters the shape of the frequency response branches and renormalizes the effective modal forcing amplitude. Simplification of Eq. (4.13) can be made when the modal amplitude is small compared with the electrode gap size, that is, when $a \ll \Delta/R$, as is common in applications (to avoid pull-in [97,138]). In this case, the nonlinear correction to the drive mode forcing can be safely neglected, $C_{FA} = 0$, an assumption we employ in the following development.

It is important to recognize that the amplitude-dependent shift of the free vibration frequency of the modes has the following sources: the stiffness Duffing nonlinearity $\gamma = \gamma_d + \gamma_e$, where γ_d and γ_e are the contributions from elastic and electrostatic stiffness effects, respectively (see Eq. (4.11)), and inertial nonlinearities which have an effective Duffing nonlinearity $\gamma_i = -\frac{2}{3}\mu\omega_A^2$ (see Eq. (4.13)). The inertial nonlinear effects have the same origin (finite deformation kinematics) as the nonlinearities in the elastic deformation potential, and we combine these effects into a single *mechanical* contribution to the modal Duffing constant, denoted $\gamma_m = \gamma_d + \gamma_i$. For moderate vibration amplitudes, the steady-state amplitude response is

that of an equivalent Duffing system and can be expressed as

$$\omega(a) \approx \omega_A + \frac{3a^2}{8\omega_A}(\gamma_m + \gamma_e) \pm \sqrt{\left(\frac{F}{2aR\omega_A}\right)^2 - \Gamma_A^2}, \tag{4.14}$$

examples of which are shown in Fig. 4.3.

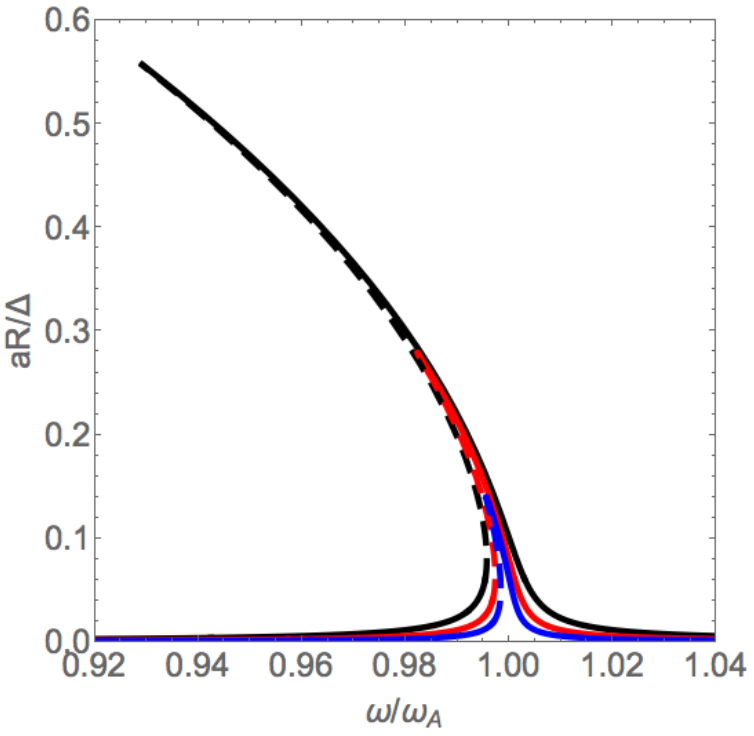

Figure 4.3: Representative steady-state frequency response curves of the ring drive mode described by Eq. (4.14) for different values of the forcing amplitude F. The blue, red, and black curves correspond to forcing magnitudes $F_0, 2F_0, 4F_0$. Responses are obtained under the assumption that electrostatic forces dominate the Duffing nonlinearity, i.e., $|\gamma_e| \gg |\gamma_m|$. Solid and dashed curves represent stable and unstable response amplitudes.

Analysis shows that inertial nonlinearities must be taken into account when $|\gamma_e| \lesssim |\gamma_m|$, which can be the case in resonators with large mechanical stiffness, like circular plates. Interestingly, when the electrostatic potential provides only small corrections to both linear and nonlinear stiffness constants, inertial nonlinearities have a dominant effect on the modal frequency response and cause substantial softening of the resonator frequency. Specifically, for the thin ring $\gamma_d = 2\omega_A^2$ and $\gamma_m = -\frac{12}{5}\omega_A^2$. Note that a similar situation occurs in

cantilever type resonators where inertial nonlinearities essentially dominate the dynamic behavior of the fundamental mode and cause the vibration frequency to soften as a function of vibration amplitude [139,140][2]. On the other hand, when $|\gamma_e| \gg |\gamma_m|$, electrostatic effects dominate the nonlinear dynamics of the system, so that the nonlinear terms arising from mechanics, both inertial and elastic stiffness, can be neglected, in which case we use the approximation $\gamma_m \approx 0$, which we will use in Section 4.2.4.

4.2.3 Dynamics of the Sense Mode: Parametric Amplification

In this section we analyze the response of the gyroscopic sense mode B, using the drive response as an effective excitation. This excitation has components from Coriolis coupling from the external angular rate Ω, and from nonlinear dispersive coupling from elastic, inertial, and electrostatic effects. In what follows, we assume that the drive mode motion can be represented as, $A(t) = aR\cos(\omega t + \phi_A)$, where a and ϕ_A are the drive mode steady-state amplitude and phase, respectively. When Ω is small as compared with the gyroscope operation frequency, i.e., $\Omega \lll \omega$, and the parametric pumping does not destabilize the sense response, the dynamic behavior of the sense mode is governed by the following equation of motion, obtained from Eq. (4.10b),

$$\ddot{B} + \dot{B}\left(2\Gamma_B + C_\Gamma \frac{A\dot{A}}{R^2}\right) + B\left(\omega_B^2 + C_d\frac{A^2}{R^2} + C_1\frac{\dot{A}^2}{R^2} + C_2\frac{A\ddot{A}}{R^2}\right) = C_\Omega \Omega \dot{A}, \tag{4.15}$$

where we have employed linearized dynamics for B (justified in Section 4.2.1). This model has direct (Coriolis) excitation from $\dot{A}$ and parametric excitation from nonlinear combinations of $(A, \dot{A}, \ddot{A})$. The C_j are constants that depend on the geometry of the gyroscope body. Since

[2]The cantilever is another system modeled using an inextensibility assumption.

Eq. (4.15) contains both direct and parametric resonant driving terms, it is convenient to represent the sense mode response in the form $B = R(b\exp[i\omega t] + c.c.)$ and apply method of averaging in the manner in [120]. After averaging and some manipulations we obtain the following expression for the steady-state amplitude of the sense mode

$$|b| = |C_\Omega|\Omega a\frac{\omega}{2}\frac{\sqrt{4\omega^2\Gamma_B^2 + (\omega_n^2 - \omega^2 + \lambda)^2}}{|4\omega^2\Gamma_B^2 + (\omega_n^2 - \omega^2)^2 - \lambda^2|} \tag{4.16}$$

where

$$\omega_n^2 = \omega_B^2 + \frac{1}{2}a^2(C_d + \omega^2(C_1 - C_2)) \tag{4.17}$$

is the effective vibration frequency of the sense mode, which is modified by nonlinear coupling to the drive mode at amplitude a, which stems from the DC components of the drive mode nonlinear coupling terms terms. Similarly, the AC components of these terms produce the coefficient

$$\lambda = \frac{1}{4}a^2(C_d + \omega^2(C_\Gamma - C_1 - C_2)) \tag{4.18}$$

which represents the strength of the parametric pumping arising from the drive mode. Note that both ω_n^2 and λ are determined by the system nonlinearities, the drive vibration amplitude a, and the gyroscope operation frequency ω.

The expression in Eq. (4.16) describes the amplitude of the sense mode and captures the interaction of the effects of the direct (Coriolis) drive and the parametric pumping from nonlinear coupling, and it reveals some important features. First, when the drive mode vibration amplitude is sufficiently small, such that one can neglect the effect of the parametric

pumping, that is, λ can be neglected, the expression for the sense mode amplitude becomes

$$|b|_l = \frac{a\omega|C_\Omega|\Omega}{2\sqrt{(\omega_B^2 - \omega^2)^2 + 4\omega^2\Gamma_B^2}}, \tag{4.19}$$

which represents the case when both modes behave like linear resonators. In this light, it is convenient to express the gyroscopic sense mode amplitude in the more general case as follows

$$|b|_{par} = G|b|_l, \quad G = \frac{\sqrt{[4\omega^2\Gamma_B^2 + (\omega_n^2 - \omega^2 + \lambda)^2][(\omega_B^2 - \omega^2)^2 + 4\omega^2\Gamma_B^2]}}{|4\omega^2\Gamma_B^2 + (\omega_n^2 - \omega^2)^2 - \lambda^2|}, \tag{4.20}$$

where G is the amplification of the sense mode, i.e., the gain, that arises from the parametric coupling to the drive mode. This gain from the coupling is illustrated in Fig. 4.4, which shows the sense mode response amplitude for the case where the coupling is ignored (black dashed lines) and for two levels of coupling (red and blue lines). Here the parametric amplification is evident, as is the frequency shift (softening due to the presence of electrostatic coupling forces) that arises from the coupling; see Eq. (4.15). A more complete representation of the gain is considered below.

Another feature associated with Eq. (4.16) is that the system gain G or, equivalently, the sense mode amplitude $|b|_{par}$ diverges when the denominator in Eq. (4.20) vanishes, i.e., $\left(4\omega^2\Gamma_B^2 + (\omega_n^2 - \omega^2)^2 - \lambda^2\right) \rightarrow 0$. By solving this equation, one obtains the parametric instability condition expressed in terms of the drive parameters as (a^*, ω^*), corresponding to $G \rightarrow \infty$. This (a^*, ω^*) condition corresponds to the case where the parametric coupling terms in Eq. (4.15) result in instability of the sense mode [65]. As this instability is approached, the linearized version of the sense mode model, given by linearizing Eq. (4.15), is insufficient

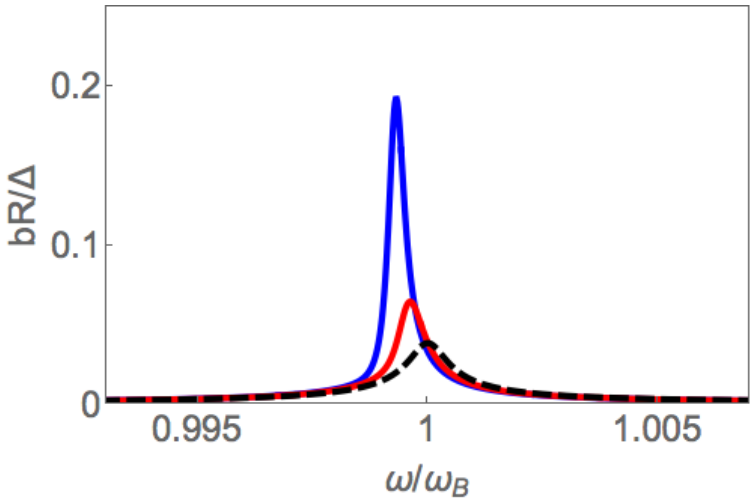

Figure 4.4: Effect of self-induced parametric amplification on frequency responses of the ring sense mode described by Eq. (4.16) for different values of the dispersive modal coupling coefficient C_d, where we consider the case $C_d/\omega_B^2 \gg C_1, C_2, C_\Gamma$, so that the parametric pumping coefficient λ is essentially proportional to C_d. Frequency responses are obtained for $aR/\Delta = 0.2$ and $\Omega/\omega_B = 2 \times 10^{-4}$. The dashed curve is the non-amplified response ($C_d = 0$), while the red and blue curves correspond to the sense mode frequency responses with $C_d/\omega_B^2 = -0.5 \times 10^4, -1.1 \times 10^4$ respectively; these numbers are chosen such that the analytical results of Section 4.2.3 remain valid, that is, so that the stated approximations hold. Signal amplification from the intermodal coupling is evident.

to describe the sense mode dynamics and the full coupled form of the equations of motion Eqs. (4.10a) and (4.10b) must be used. In this work, however, we restrict our analysis to the case where the response of the sense mode remains in its linear range and its vibration amplitude remains proportional to Ω. In fact, this is the range of practical interest.

4.2.4 Example

Generally speaking, one can adapt the approach developed here to a variety of gyroscope configurations that exploit circular symmetry. Here we illustrate the applicability of the results by using parameters derived for the polysilicon ring gyroscope reported in [19]. First, we consider the idealized case of a free (no suspension) gyroscope ring. The gyroscope parameters are as follows: the mid-line radius of the ring is $R = 550\ \mu$m, the radial thickness

is $h = 4\,\mu$m, the electrode gap size is $\Delta = 1.4\,\mu$m, the estimated quality factor is $Q = 1200$, and the bias voltage is taken to be $V_{DC} = 3\,\text{V}$ (we intentionally take this value of V_{DC}, as compared to 7 V in [19], to avoid the electrostatic pull-in effect). As a result, the gyroscope dynamic parameters become $\omega_B/2\pi = 12.5$ kHz, $\Gamma_B/\omega_B = 1/2400$ and the electrostatic potential strongly dominates the strength of the dispersive modal coupling, $C_d/\omega_B^2 \sim -10^5$, while the other constants defined in Eq. (4.10b) satisfy $C_\Gamma, C_1, C_2 \ll C_d/\omega_B^2$.

Figures 4.5a and 4.5b show the self-induced parametric gain G as a function of the normalized drive frequency ω/ω_B and the normalized vibration amplitude of the drive mode aR/Δ (left panel) and the normalized strength of the stiffness coupling C_d/ω_B^2 (right panel). The solid red curve depicts the instability condition, (a^*, ω^*) in both panels, where the value of the gain approaches infinity, that is, it is the Arnold tongue for the sense mode [141, 142]. The meshed region on both panels corresponds to the set of operating conditions where the solution found in Eq. (4.16) is unstable. In order to describe the gyroscope dynamics in these regions, one must analyze the full form of Eqs. (4.10a) and (4.10b), since in this region nonlinear effects that have been ignored will come into play.

As follows from considering the results of Fig. 4.5a, in order to achieve significant gain G, the drive mode should be operated at frequencies slightly less than ω_B. This can be easily satisfied since the electrostatic forces dominate the nonlinearities of the gyroscopic drive mode and its frequency response exhibits softening behavior. Figure 4.5b, on the other hand, illustrates the behavior of the gain G as a function of the operating frequency and the strength of the intermodal dispersive coupling. Importantly, the magnitude of the intermodal coupling can be controlled by adjusting the bias voltage V_{DC} applied to the resonator body or attendant electrodes, thus allowing one to tune the amount of self-induced parametric amplification, which increases gyroscope sensitivity S in the vicinity of the instability region.

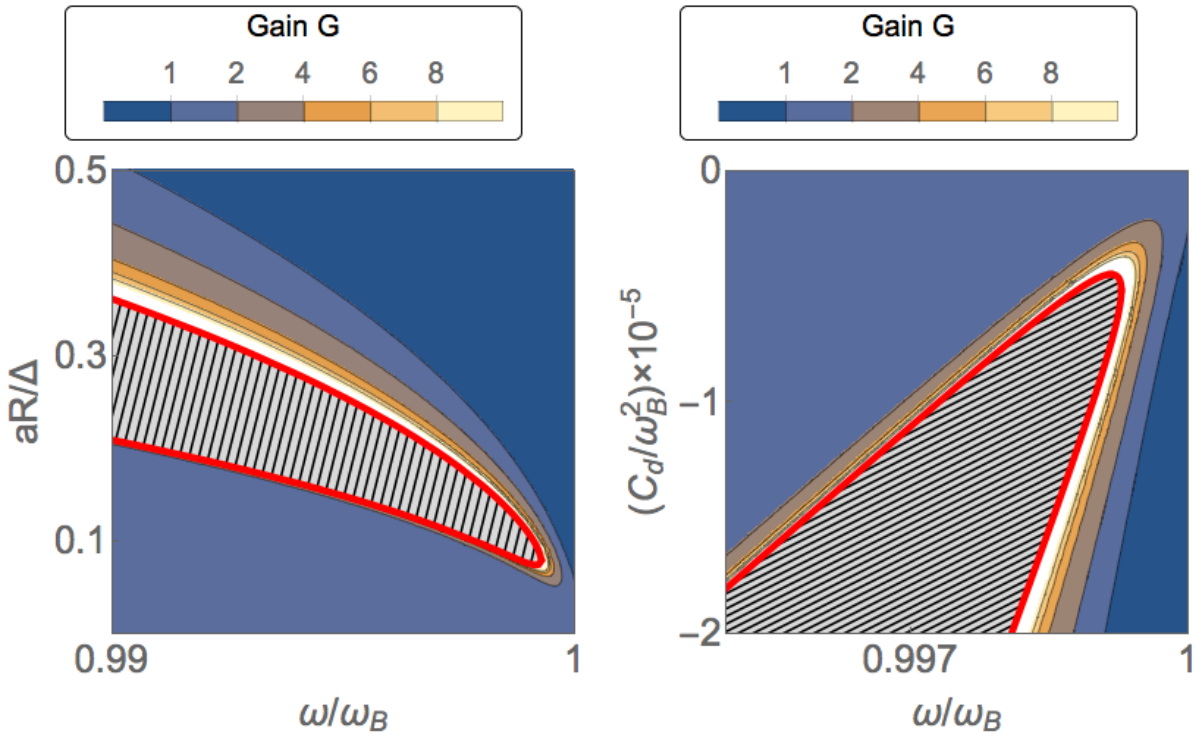

(a) Dependence of the strength of the self-induced parametric amplification G on the scaled operation frequency ω/ω_B and the vibration amplitude of the drive mode aR/Δ. The stiffness coupling strength is $C_d/\omega_B^2 = -95 \times 10^3$.

(b) Dependence of the strength of the self-induced parametric amplification on the scaled operation frequency ω/ω_B and the nonlinear dispersive coupling strength C_d/ω_B^2. The drive mode vibration amplitude is chosen to be $aR/\Delta = 0.1$.

Figure 4.5: Increase of the sensitivity of the gyroscope ring (without suspension) due to nonlinear modal coupling as a function of system and drive parameters. The solid red line represents the $a^*-\omega^*$ curve where the gain G diverges according to the linear model described by Eq. (4.15); this is the primary Arnold tongue for the sense mode [141]. The meshed region is the set of operating conditions where the solution found in Eq. (4.16) is unstable.

Furthermore, the critical value of the drive mode amplitude, where $G \to \infty$, decreases as $C_d^{-1/2}$. Physically, as expected, this implies that for stronger dispersive intermodal coupling, smaller drive vibration amplitudes are required to achieve the same level of gain.

The results obtained for the case of the unsuspended gyroscope ring can be easily extended to account for supporting springs in the form of semicircles with the mid-line radius $R_s = 235\ \mu m$ and radial thickness $h = 4\ \mu m$; see [19] for details. Numerical analysis shows that for the polarization voltage $V_{DC} = 7\ V$ (the voltage used by Ayazi et al. in their exper-

iments), electrostatic forces still dominate the system nonlinearities, including the dispersive modal coupling strength, $C_d/\omega_B^2 \sim -10^4$. As a result, the dependence of the gyroscope sensitivity on the system parameters is qualitatively the same as in the case of the free ring; see Figs. 4.5a and 4.5b.

Our analysis of a gyroscope with a suspension shows that the inclusion of the semi-circular suspending springs in the model change the resonator kinetic and potential energies, where the latter is affected through its elastic component only, since there is no interaction of the springs with the electrodes. Due to the symmetry of the gyroscope elliptical modes, the suspension springs are equivalent to four additional rings of radius R_s, where one pair belongs to the drive mode and the other to the sense mode. In this case, however, when calculating the kinetic energy we also have to account for the motion of the spring mass, which contributes to the effective modal mass. Furthermore, analysis shows that the gyroscope suspension has considerable effect on the individual modal stiffness parameters, affecting both the linear natural frequency and the Duffing nonlinearity. These contributions can be calculated in a straightforward way following the method described in Section 4.2.1. In particular, the mechanical contributions to the modal natural frequency and the Duffing modal nonlinearity increase by factors of 5 and 12, respectively. Additionally, the suspension springs also affect the dispersive modal coupling strength; in fact, the mechanical component of κ increases by nearly a factor of two. This contribution to the modal coupling strength is the result of the nonlinear nature of the strain-displacement relationships in Eqs. (4.5a) to (4.5c). Similar results for more complicated geometries, such as the DRG in [27], can be obtained using finite element methods adapted for computing nonlinear coefficients for mechanics [43,143], although doing such calculations for nonlinear electrostatic effects is still being developed.

4.3 Manipulating gyroscope nonlinearities: geometric and electrostatic optimization methods

In this section we analyze three different methods for manipulating the magnitude of nonlinear dispersive coupling $|\kappa|$ and the modal Duffing nonlinearity γ in order to maximize the sensitivity of the micromechanical gyroscope with respect to the external angular rate Ω and increase the gyroscope dynamic range. Specifically, in the following subsections we consider tailoring of the aforementioned gyroscope nonlinearities via a non-uniform distribution of the bias voltage V_{DC} among the gyroscope electrodes, an angle-dependent electrode gap size $\Delta = \Delta(\theta)$, and an angle-dependent thickness of the gyroscope ring $h = h(\theta)$, respectively. Note that in all these methods we consider only such modifications of the gyroscope bias voltage, the electrode gap size, and the radial thickness of the resonator ring that have at least 8-fold rotation symmetry relative to the $z-$axis of the gyroscope. Importantly, this constraint on the gyroscope parameters maintains the inherent symmetry of the gyroscopic vibrational modes, which allows one to avoid additional problems associated with matching the modal natural frequencies.

Due to the dispersive nature of the intermodal coupling between the gyroscopic drive and sense modes, the gyroscope sense mode response depends on both κ and γ, and this dependence is generally complicated. Given our goals of maximizing the gyroscope angular rate sensitivity and the gyroscope dynamic range at the same time, it is convenient to choose the objective function for our optimization problem to be the strength of the parametric pumping when the gyroscope drive mode is operating at the inflection point on its frequency response (onset of nonlinearity). The objective function is formulated as follows: We note that the drive mode critical amplitude $a_{cr} \propto \gamma^{-1/2}$ and the pumping strength is κa_{cr}^2,

suggesting an objective function of $K = |\kappa/\gamma|$. We will assume that the modal natural frequencies are still matched and that the damping constants depend weakly on the changes employed for the gyroscope geometry and DC bias.

Before we proceed to specific optimization methods, it is useful to understand the effect of the chosen objective function K on the gyroscope performance. In order to do this, we first rewrite Eq. (4.16) as follows

$$|b|_{a=a_{cr}} = |C_\Omega|\Omega' a_{cr}\frac{\omega'}{2}\frac{\sqrt{\frac{\omega'^2}{Q_B^2}+\left(1-\frac{2K}{Q_B\sqrt{3}}-\omega'^2\right)^2}}{\left|\frac{\omega'^2}{Q_B^2}+\left(1-\frac{4K}{3Q_B\sqrt{3}}-\omega'^2\right)^2-\frac{4}{27Q_B^2}K^2\right|}, \tag{4.21}$$

where $\omega' = \omega_{cr}/\omega_B = 1-\frac{\sqrt{3}}{2Q_B}$ is the gyroscope operating frequency (which, of course, coincides with the critical vibration frequency of the drive mode), $\Omega' = \Omega/\omega_B$ is the scaled external angular rate, and we have assumed, given our example in Section 4.2.4, that $|C_d|/\omega_B^2 \gg |C_1|, |C_2|, |C_\Gamma|$. From Eq. (4.21) it follows that the gyroscope performance depends on both a_{cr} and, consequently, γ and K, where the latter effect of our objective function K on the sense mode amplitude $|b|$ can be conveniently expressed using the following *figure of merit*,

$$F.O.M. = \frac{\sqrt{\frac{\omega'^2}{Q_B^2}+\left(1-\frac{2K}{Q_B\sqrt{3}}-\omega'^2\right)^2}}{\left|\frac{\omega'^2}{Q_B^2}+\left(1-\frac{4K}{3Q_B\sqrt{3}}-\omega'^2\right)^2-\frac{4}{27Q_B^2}K^2\right|}. \tag{4.22}$$

Figure 4.6 illustrates the dependence of the figure of merit on the value of the objective function. As follows from this figure, in order to increase the gyroscope sensitivity, it is desirable to implement such modifications to the gyroscope geometry and electrostatic setup

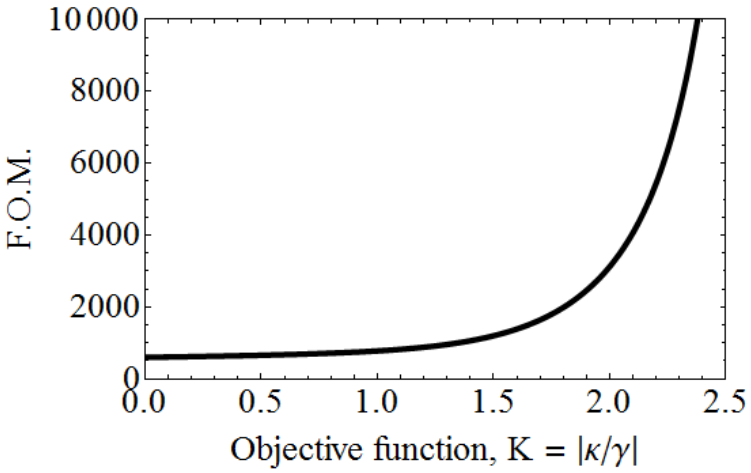

Figure 4.6: Dependence of the figure of merit in Eq. (4.22) on the value of the objective function K. Quality factors of the gyroscope drive and sense modes are assumed to be $Q_A = Q_B = 1200$ [19].

that will maximize K while keeping $|\gamma|$ low due to the dependence of the gyroscope sense mode response on a_{cr}. This forms the baseline for our subsequent development of the optimization methods in following sections of this dissertation.

4.3.1 Nonlinear electrostatic tuning by a non-uniform bias voltage

We start with the relatively simple method of electrostatic tuning, which is frequently used for modifying the vibration frequency of MEMS resonators by altering the bias voltage. In the present case, however, we are interested in modifying the gyroscope *nonlinear* parameters κ and γ. Without any alterations of the gyroscope electrostatic actuation/sensing setup, κ and γ, are defined in Eq. (4.11),

$$\kappa = \gamma = \frac{6R^2}{5\rho}\left(\frac{Eh^2}{R^6} - \frac{\epsilon_0 V_{DC}^2}{h\Delta^5}\right),$$

from where it follows that a uniform increase/decrease of the bias voltage changes both coefficients simultaneously. Our goal, however, is to maximize $|\kappa|$ while minimizing $|\gamma|$.

In order to achieve this, below we consider the case of a non-uniform bias voltage, i.e. $V_{DC} = V_{DC}(\theta)$.

Frequently, MEMS ring/disk resonating gyroscopes are designed to have $4N$ electrodes ($N \geq 2$) along the circumference in order to be able to support $\sin 2\theta$ and $\cos 2\theta$ in-plane elliptical vibrational modes. In this case, the nonlinear electrostatic tuning method results in different values of the bias voltage applied to different electrodes, i.e. $V_{DC} = V_{DC}(k)$, where k is the electrode number. Keeping in mind the symmetry of the gyroscopic modes, it becomes clear that the 8-electrode configuration can support only uniform distribution of the bias voltage V_{DC}, which, as we discussed above, is of limited interest. As a result, in order to show the effect of $V_{DC}(k)$ on the resonator nonlinearities, we further assume that the gyroscope design has $8N$ electrodes ($N \geq 2$). In this case the electrostatic potential energy becomes

$$U_e \approx -\frac{\epsilon_0 bR}{2} \sum_{k=1}^{8N} \sum_{n=0}^{4} \int_{\theta_k-\psi}^{\theta_k+\psi} d\theta (V_{DC}(k) + V_{AC}(k,t))^2 \frac{u^n(\theta)}{\Delta^{n+1}}, \tag{4.23}$$

where θ_k is the angular position of the k^{th} electrode center, 2ψ is the circumferential length of each electrode (in radians), and both V_{DC} and V_{AC} are now functions of the electrode number.

Since the gyroscope kinetic energy in Eq. (4.1) is independent of V_{DC}, a non-uniform bias voltage distribution only affects κ and γ through their electrostatic contributions, κ_e and γ_e, determined by the coefficients of the terms $\propto A^2B^2$ and $\propto A^4$ in Eq. (4.23). In order to illustrate the nonlinear electrostatic tuning method, we consider the specific case when $N = 2$, as in [38], and assume the following distribution of the bias voltage $V_{DC}(k) = V_{DC}(1 + (-1)^k r_{DC})$, $k = 1, \ldots, 16$. Restricting ourselves to the case of the commonly used

uniform electrode gap size, we obtain

$$\frac{\kappa_e^{(DC)}}{\kappa_e^{(0)}} = 1 - r_{DC}\frac{12R^2}{\pi(3R^2 - 12R\Delta + 8\Delta^2)} + r_{DC}^2 \approx 1 - \frac{4}{\pi}r_{DC} + r_{DC}^2, \tag{4.24a}$$

$$\frac{\gamma_e^{(DC)}}{\gamma_e^{(0)}} = 1 + r_{DC}\frac{4R^2}{\pi(3R^2 - 12R\Delta + 8\Delta^2)} + r_{DC}^2 \approx 1 + \frac{4}{3\pi}r_{DC} + r_{DC}^2, \tag{4.24b}$$

where $\kappa_e^{(0)} = \gamma_e^{(0)}$ are the values of the coupling strength and Duffing nonlinearity in the absence of the nonlinear electrostatic tuning , i.e., when $r_{DC} = 0$. The dependence of κ_e, γ_e, and K_e on the variation in the gyroscope bias voltage r_{DC} presented in Eq. (4.24a) and Eq. (4.24b) is shown in Fig. 4.7.

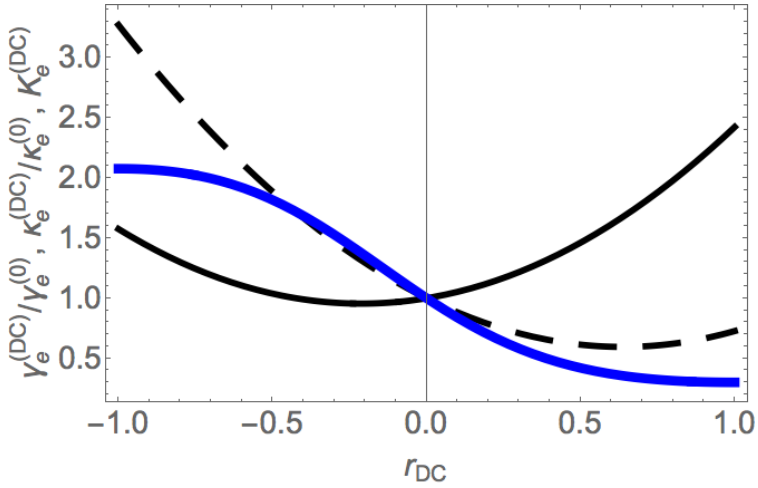

Figure 4.7: Behavior of the electrostatic components of the dispersive coupling strength (black dashed curve), the Duffing nonlinearity (black solid curve), and the objective function (blue solid curve) as a function of the variation in the bias voltage r_{DC}.

In ring/disk resonating gyroscopes, the electrostatic forces from the actuation/sensing scheme frequently dominate the nonlinear dynamic behavior of the gyroscopic vibrational modes, i.e., $\kappa \approx \kappa_e$ and $\gamma \approx \gamma_e$. In this case, Fig. 4.7 clearly shows that when $r_{DC} < 0$, one can achieve up to 3-fold increase in $|\kappa|$. At the same time, $|\gamma|$ decreases for $r_{DC} \in (-4/3\pi, 0)$, but increases, although slower than $|\kappa|$, for $r_{DC} \in (-1, -4/3\pi)$. Assuming, for instance,

that we would like to not decrease the gyroscope dynamic range, we then have to choose $r_{DC} = -4/3\pi$, which corresponds to $\approx 72\%$ increase of the modal coupling strength and, as a result, the objective function K. Such an increase of $|\kappa|$ should result in approximately 2-fold increase of the figure of merit, see Fig. 4.6. Note that the nonlinear electrostatic tuning method described here also shifts the natural frequencies of the gyroscopic vibrational modes. However, since the gyroscope linear stiffness is dominated by the mechanical elastic effects, this correction to the modal frequencies is rather small, seen by considering, for example, that the coefficient of the term $\propto A^2$ in Eq. (4.23), and following the same line of thought that the electrostatic correction to the modal linear stiffness is $\propto r_{DC}^2$.

4.3.2 Effect of a non-uniform electrode gap size

Now we assume that $V_{DC} = const$ and consider the effect of a non-uniform electrode gap size on the magnitude of the dispersive modal coupling strength and modal Duffing nonlinearity. Unlike in the previous method, the electrode gap size can be varied in a continuous fashion along the gyroscope circumference, i.e., $\Delta = \Delta(\theta)$ and the gyroscope electrostatic potential energy determining the system stiffness parameters becomes

$$U_{el} \approx -\frac{\epsilon_0 bR}{2} V_{DC}^2 \sum_{n=0}^{4} \int_0^{2\pi} d\theta \frac{u^n(\theta)}{\Delta^{n+1}(\theta)}. \tag{4.25}$$

As we mentioned before, the variation in the electrode gap size should possess at least 8-fold rotation symmetry in θ in order to ensure that the gyroscopic modes remain degenerate

$$\Delta(\theta) = \sum_{k=0}^{\infty} \Delta_k \cos 8k\theta, \tag{4.26}$$

where Δ_k are some constants. In this work, we consider the simplest case yielding a non-trivial result: $\Delta(\theta) = \Delta_0(1 + r_\Delta \cos 8\theta)$. From the physical standpoint, the variation r_Δ must satisfy $|r_\Delta| < 1$; in practice, however, this condition for $|r_\Delta|$ becomes even stronger due to additional constraints of the chosen fabrication process. Assuming that the gaps between individual electrodes are small, we expand the denominator in Eq. (4.25) in Taylor series up to the second order in r_Δ and obtain the electrostatic corrections to the coefficients of the dispersive coupling and the Duffing nonlinearity in the form

$$\frac{\kappa_e^{(\Delta)}}{\kappa_e^{(0)}} \approx 1 + \frac{5}{2} r_\Delta + \frac{15}{2} r_\Delta^2, \tag{4.27a}$$

$$\frac{\gamma_e^{(\Delta)}}{\gamma_e^{(0)}} \approx 1 - \frac{5}{6} r_\Delta + \frac{15}{2} r_\Delta^2. \tag{4.27b}$$

The dependence of the electrostatic components to the gyroscope intermodal coupling strength, the individual modal Duffing nonlinearity and the objective function K on the variation in the electrode gap size r_Δ is shown in Fig. 4.8a. From this figure it immediately follows that the case with $r_\Delta > 0$ becomes of significant importance for the gyroscopes whose dynamic behavior in the nonlinear regime is dominated by electrostatic effects. Indeed, when $r_\Delta > 0$, the dispersive coupling strength $|\kappa_e|$ grows faster than the Duffing nonlinearity $|\gamma_e|$. Furthermore, $\gamma_e^{(\Delta)}/\gamma_e^{(0)} < 1$ for $r_\Delta \in (0, 1/9)$. Assuming, as before, that we would like not to supress the gyroscope dynamic range, we choose $r_\Delta = 1/9$ and achieve $\approx 37\%$ increase of $|\kappa_e|$ by a simple alteration of the shape of the gyroscope electrodes at the design stage; see Fig. 4.8b. As it follows from Fig. 4.6, this increase of the coupling strength and the objective function should lead to $\approx 32\%$ increase of the gyroscope sense mode response when the drive mode is driven on the onset of modal nonlinearity.

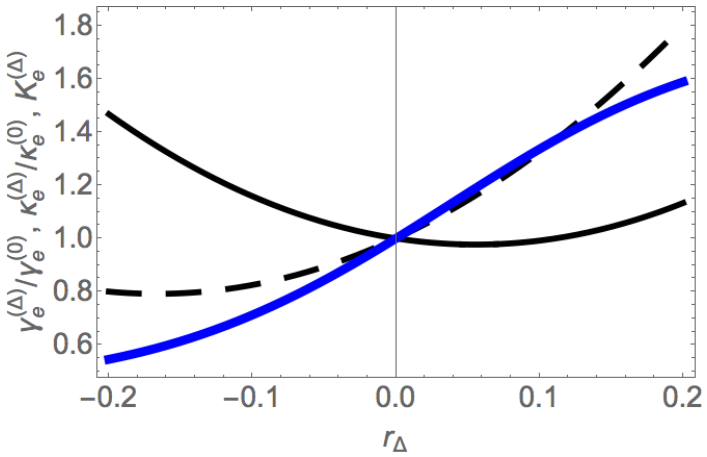

(a) Dependence of the electrostatic components of the dispersive coupling strength (black dashed curve), the Duffing nonlinearity (black solid curve), and the objective function (blue solid curve) as functions of the variation in the electrode gap size r_Δ.

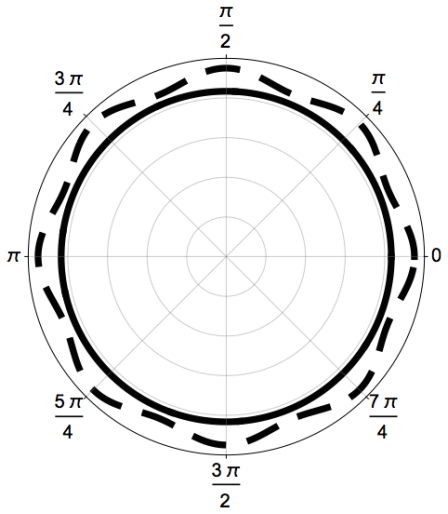

(b) Schematic representation of the ring resonating gyroscope with the non-uniform electrode gap size with $r_\Delta = 0.4$. The solid circle represents the outer boundary of the gyroscope body; the dashed wavy loop represents the inner boundary of the attendant electrodes.

Figure 4.8: Manipulating gyroscope nonlinearities via a non-uniform electrode gap size

4.3.3 Shape optimization of the gyroscope body

Lastly, we show how one can alter the mechanical contributions to the dispersive modal coupling strength and the individual modal Duffing nonlinearity in micromechanical ring/disk resonating gyroscopes by modifying the shape of the gyroscope body while keeping the electrode gap the same along the gyroscope circumference. Here we illustrate this technique by manipulating the nonlinear stiffness parameters of a thin spinning ring, discussed in Section 4.2, by modifying the ring radial thickness along the gyroscope circumference. Similar to the electrode gap size in Section 4.3.2, we enforce the ring radial thickness to be periodic in θ with the period being at most $\pi/4$ in order to preserve the symmetry of the drive and

sense modes. Mathematically we express $h(\theta)$ as

$$h(\theta) = \sum_{k=0}^{\infty} h_k \cos 8k\theta, \tag{4.28}$$

where h_k are some constants. Inclusion of $h(\theta)$ in the dynamic model for the ring resonating gyroscope modifies obtained earlier expressions for the gyroscope kinetic and mechanical potential energies as follows

$$T(u, v, \dot{u}, \dot{v}) = \frac{\rho b R}{2} \int_0^{2\pi} d\theta [(\dot{u} - v\Omega)^2 + (\dot{v} + (r + u)\Omega)^2] h(\theta), \tag{4.29a}$$

$$U_m = \frac{Eb}{24R^3} \int_0^{2\pi} d\theta \left[u + \frac{\partial^2 u}{\partial \theta^2} - \frac{1}{2R} \left(\frac{\partial u}{\partial \theta} \right)^2 \right]^2 h(\theta)^3. \tag{4.29b}$$

As we mentioned in Section 4.2, modifications in the resonator geometry effect the gyroscope intermodal coupling and Duffing nonlinearity in two ways. First, as it follows from Eq. (4.29a), the non-uniformity of the ring radial thickness affects the effective modal mass, the coefficient of the term $\propto \dot{A}^2$ in the gyroscope kinetic energy. Additionally, $h(\theta)$ changes stiffness coefficients of the terms $\propto A^2 B^2$ and $\propto A^4$ in the gyroscope potential energy due to elastic deformations of the ring. By accounting for these two effects, we express mechanical contributions to κ and γ as

$$\kappa_m = \frac{2E}{\rho R^6} \frac{\int_0^{2\pi} d\theta (1 + \sin^2 4\theta) h^3(\theta)}{\int_0^{2\pi} d\theta (1 + 3\cos^2 2\theta) h(\theta)}, \tag{4.30a}$$

$$\gamma_m = \frac{2E}{3\rho R^6} \frac{\int_0^{2\pi} d\theta (1 + 4\sin^2 2\theta + 4\sin^4 2\theta) h^3(\theta)}{\int_0^{2\pi} d\theta (1 + 3\cos^2 2\theta) h(\theta)}, \tag{4.30b}$$

from where it immediately follows that if the ring radial thickness is constant, i.e., $h(\theta) = h_0$, then $\kappa_m = \gamma_m$, as expected.

To demonstrate the effect of a non-uniform ring radial thickness, we consider a rather simple case when $h_k = 0$ for $k \geq 2$ in Eq. (4.28). In this case we have

$$\frac{\kappa_m^{(h)}}{\kappa_m^{(0)}} = 1 - \frac{1}{2} r_h + \frac{3}{2} r_h^2 - \frac{1}{8} r_h^3, \tag{4.31a}$$

$$\frac{\gamma_m^{(h)}}{\gamma_m^{(0)}} = 1 + \frac{1}{6} r_h + \frac{3}{2} r_h^2 + \frac{1}{24} r_h^3, \tag{4.31b}$$

where $r_h = h_1/h_0$. Figure 4.9a illustrates the dependence of κ_m and γ_m on r_h. Here we

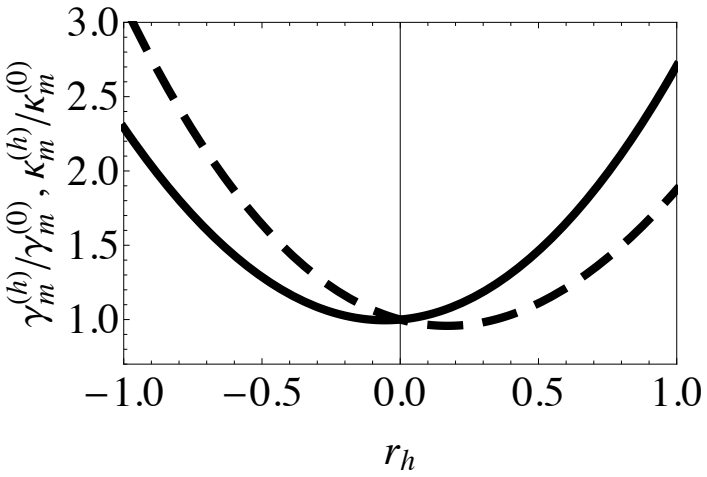

(a) Dependence of mechanical components of the dispersive coupling strength (black dashed curve) and the Duffing nonlinearity (black solid curve) on the ring thickness modifier r_h. Since the gyroscope dynamics is dominated by electrostatic forces, the objective function is essentially determined by κ_e and γ_e and, thus, not shown here.

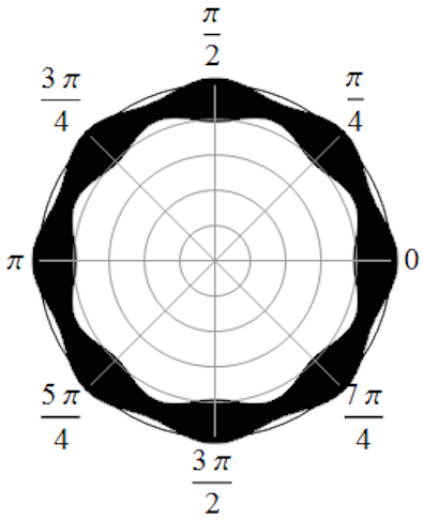

(b) Representative geometry of the ring resonating gyroscope with non-uniform radial thickness with $r_h > 0$. Electrodes are omitted for clarity.

Figure 4.9: Manipulating nonlinear parameters of a thin spinning ring by modifying the radial ring thickness $h(\theta)$

assume, as we did previously, that the gyroscope nonlinear dynamics is dominated by the electrostatic restoring forces, i.e., $|\kappa_e| > \kappa_m$ and $|\gamma_e| > \gamma_m$. Since $|\kappa| = |\kappa_e| - \kappa_m$ and $|\gamma| = |\gamma_e| - \gamma_m$, it is clear that in order to increase $|\kappa|$ and decrease $|\gamma|$, we need to minimize κ_m and maximize γ_m. From Fig. 4.9a it follows that both goals can be achieved if we

modify the ring radial thickness with $r_h > 0$, see Fig. 4.9b. Physically, the case when $r_h > 0$ corresponds to adding the mass to the areas of the ring that experience largest deflections in the radial direction as it vibrates in the drive and sense modes while removing the material in the other areas. In particular, $\kappa_m^{(h)} < \kappa_m^{(0)}$ when $r_h \in (0, 6 - 4\sqrt{2})$ with its minimum reached at $r_h^* = 4 - 2\sqrt{11/3}$. In this case $\kappa_m^{(h)}$ reduces by $\approx 5\%$ and $\gamma_m^{(h)}$ increases by $\approx 7\%$. While these results are obviously less impressive as compared to the ones we obtained using nonlinear electrostatic tuning methods, see Sections 4.3.1 and 4.3.2, this mechanical optimization method should not be overlooked when one attempts to optimize the performance of micromechanical ring resonating gyroscopes with relatively simple geometries of the resonator body [19].

4.4 Outlook

In this chapter we have analyzed the phenomenon of self-induced parametric amplification of in-plane flexural vibrations of degenerate elliptical modes in ring/disk resonating gyroscopes. The most important feature of this amplification is a gain in sensitivity that is achieved from the naturally occurring dynamics of the system. This is a prime example of where nonlinear behavior provides an opportunity for improved performance of a practical device. By utilizing the model of a thin spinning ring in the presence of electrostatic actuation/sensing, we have demonstrated that, in addition to the linear Coriolis coupling that is the basis for operation as an angular rate sensor, the drive and sense modes are coupled nonlinearly through elastic, inertial, and electrostatic effects. We have further illustrated that this modal coupling results in parametric pumping of the sense mode by the drive mode, which can lead to a significant improvement in the gyroscope sensitivity with respect to the external angular rate, as was

experimentally observed in [27]. We have also examined the effects of the drive conditions on the performance of the sensor, and illustrated these effects for two representative micromechanical ring resonating gyroscopes. In our analysis we have focused our attention on the case when $\Omega \ll \omega_0$ (a valid assumption for high precision gyroscopes), which allowed us to neglect the back-action effect of the sense mode vibrations on the drive mode dynamics, significantly simplifying the analysis. Our future efforts in this direction will be devoted to developing a better understanding of the internal resonance that naturally occurs in these systems, which have two vibrational modes with close natural frequencies. This leads to very rich dynamics, including high sensitivity to certain effects, such as linear modal coupling (quadrature error), which need to be better understood in order to fully exploit the nonlinear modal coupling.

Additionally, we have described three different methods one can use to manipulate nonlinear parameters of ring/disk resonating gyroscopes in a systematic way to improve the gyroscope performance as a rate sensor. In this study our main goal was to maximize the intermodal dispersive coupling strength between the drive and sense modes in order to enhance the self-induced parametric amplification and the gyroscope rate sensitivity, and to simultaneously suppress the individual modal Duffing nonlinearity of the drive mode in order to maximize the gyroscope linear range. Two out of three methods involve modifications in the gyroscope electrostatic setup, which are found to be highly effective for manipulating the response, and the third technique deals with geometry modifications of the gyroscope mass, which is found to be less effective. Specifically, we have shown that if the gyroscope actuation/sensing scheme has at least 16 electrodes, it is possible to modify the intermodal coupling strength and modal Duffing constant by applying a non-uniform distribution of the bias voltage. Additionally, we demonstrated that a non-uniform electrode gap size also

affects the magnitude of the gyroscope nonlinear coefficients and can be used to tailor the gyroscope nonlinear dynamic behavior. Finally, we illustrated the applicability of the shape optimization method in manipulating nonlinear stiffness parameters of a thin spinning ring by altering the ring radial thickness along the ring circumference.

These examples clearly illustrate the impact of optimization methods for improving the performance of MEMS gyroscopes and provides additional motivation for their further exploration for other types of MEMS resonators. An obvious extension to further improve the performance of the ring/disk resonating gyroscope is to combine the above approaches. For example, assuming that the nonlinear behavior of the gyroscope is primarily determined by electrostatic forces, i.e., $|\kappa_e| \gg |\kappa_m|$ and $|\gamma_e| \gg |\gamma_m|$, one can apply modifications of both the electrode gap size and the bias voltage along the gyroscope circumference. In this case, following the results of Sections 4.3.1 and 4.3.2, one should be able to preserve the gyroscope [19] dynamic range while achieving $K \approx 2.36$, where the latter results in nearly 12-fold increase of the gyroscope sensitivity, as seen from Fig. 4.6. Using obtained results as a starting point, we plan to continue our work on optimization of the performance of ring and disk resonating gyroscopes. Particular directions would include identifying the appropriate metric (objective function) that would characterize the overall performance of the gyroscope and analysis of the ways that would optimize the selected objective function. Additionally, we plan to test our hypotheses and verify analytical findings with our collaborators.

The analytical results presented here can be used for predicting the nonlinear behavior of existing gyroscopes and proposed gyroscope models, and, more importantly, for designing ring/disk resonating gyroscopes with optimized performance and maximized sensitivity using their inherent dynamics. However, to make full use of these ideas one must employ computational tools that allow for optimization using many more design variables. Such

methods can be applied to the restricted problems proposed here, combinations of them, or to entirely new configurations, possibly suggested by shape and topology optimization techniques.

Chapter 5

Conclusions

In this dissertation we have considered three topics related to nonlinear and noise-induced dynamics in micro-scale and, to a certain extent, in nano-scale electromechanical resonators. In general, our perspective on nonlinearities and noise in MEMS is to accept them as integral parts of virtually any MEMS resonator model, to find ways to understand their effects, to develop methods for characterizing them, and, where possible, to employ them for specific applications. The specific goals were: (i) to extend our understanding of Poisson noise in parametrically driven MEMS resonators; (ii) to develop comprehensive and robust methods for quantitative characterization of nonlinearities and noise in MEMS; and (iii) to develop models for the non-linear self-induced parametric amplification observed in MEMS ring and disk resonating gyroscopes and use these models to propose new designs that improve their performance as angular rate sensors.

In Chapter 2 we studied the probability distribution of a parametrically driven resonator driven by modulated Poisson pulses in the presence of weak thermal noise. The pulses are actually composed of short bursts of harmonic signal at one half of the driving frequency with the duration of each pulse much longer than the resonator vibration period but much smaller than the resonator typical relaxation time. In the rotating frame of reference these bursts appear as essentially instantaneous pulses that cause jumps in the location of the state in that frame. With the ability to tune the direction of these Poisson pulses, and to choose the measurement quadrature in the rotating frame, we have shown that, for suffi-

ciently small pulse rates, the probability distribution exhibits a power-law singularity near the resonator equilibrium in both the overdamped and underdamped regimes of the rotating frame. Additionally, we have described the dependence of the corresponding exponent on the Poisson mean pulse rate and the system decay rate in the rotating frame. We also found additional peak(s) in the distribution away from the origin and specified their positions and the conditions for their appearance. In particular, we demonstrated that the probability distribution is strongly asymmetric in the overdamped regime, while in the underdamped regime it has a self-similar structure. Weak thermal noise affects the system by smoothening the singular peaks in the distribution and by making the distribution Gaussian in the vicinity of these peaks. Our analytical results for the power-law exponents near the peaks of the probability distribution, and for the positions of peaks in the rotating frame, are in excellent agreement with experimental measurements from a micromechanical resonator taken by collaborators at the Hong Kong University of Science and Technology. Importantly, our results can be immediately extended to understand the dynamics of a MEMS/NEMS resonator subject to a multiplicative noise of Poisson type, which is frequently the case in mass sensing applications.

In Chapter 3 we introduced and developed a comprehensive method for characterizing model parameters for MEMS resonators whose vibration are governed by a single mode. The method relies entirely on measurements taken from a single ringdown signal of a lightly damped system. This approach has the advantage that the resonator response is not affected by any drive transduction, which reduces modeling uncertainty; one must only account for readout transduction to separate the underlying resonator dynamics. The model parameters of interest include coefficients of linear and nonlinear damping and stiffness terms, as well as the most important types of noise sources. In particular, we have illustrated how one

can estimate values for deterministic stiffness and damping parameters for the symmetric vibrational mode of a MEMS resonator. A key to the method is that the vibrational amplitude is affected only by the dissipation parameters, while the frequency and phase are affected by the resonator conservative parameters, thereby uncoupling the characterization process. First, the linear and nonlinear friction coefficients are obtained from the shape of the vibration envelope, fitted to a model for the slowly varying amplitude obtained from the method of averaging. Additionally, we have demonstrated how one can estimate the modal natural frequency and conservative cubic and quintic (stiffness) nonlinearities using a measured sequence of zero-crossing times in the ringdown response, which are affected by the instantaneous frequency of vibration, which is directly linked to the stiffness model. Note that this ringdown-based characterization method, unlike conventional frequency sweeping, is unique since allows *direct* revealation of the nonlinear dissipation in the system of interest. Furthermore, we have developed a novel technique for direct determination of the intensities of measurement, thermal, and frequency noise sources in the resonator and its readout signal, by performing a statistical analysis of the locations of zero-crossing points in the measured ringdown response. We have shown that these noise sources have qualitatively different signatures on the jitter of the resonator timing. Therefore, using these specific features of the jitter we are to estimate the intensities of these three important noise sources. Possible future directions include adaptation of the ringdown-based method for parameter characterization of systems with asymmetric restoring forces, e.g. beam resonators with one electrode, and coupled-mode systems. Additional efforts can be directed towards improving accuracy of the noise characterization in the systems with strong measurement noise and gaining more comprehensive understanding of the origin of different noise sources by studying high-order statistics of the resonator phase in the ringdown response.

In Chapter 4 we analyzed the phenomenon of self-induced parametric amplification of in-plane flexural vibrations of degenerate elliptical modes in ring/disk resonating gyroscopes. This study was motivated by experimental observations described in [27]. The most important feature of this amplification is a gain in sensitivity that is achieved from the naturally occurring dynamics of the system, which improves both device sensitivity and its signal-to-noise ratio (SNR). This is a prime example of where nonlinear behavior provides an opportunity for improved performance of a practical device. By utilizing the model of a thin spinning ring in the presence of electrostatic actuation/sensing, we have demonstrated that, in addition to the linear Coriolis coupling that is the basis for operation as an angular rate sensor, the drive and sense modes are coupled nonlinearly through elastic, inertial, and electrostatic effects. We have further illustrated that this modal coupling results in parametric pumping of the sense mode by the drive mode, which can lead to a significant improvement in the gyroscope sensitivity with respect to the external angular rate, as was experimentally observed in [27]. We have also examined the effects of the drive conditions on the performance of the sensor and illustrated these effects for two representative micro-mechanical ring resonating gyroscopes.

Additionally, we used our modeling results to develop methods one can use to manipulate the nonlinear stiffness parameters of these gyroscopes in a systematic way in order to improve their performance as rate sensors. Our main goal was to maximize the intermodal dispersive coupling strength between the drive and sense modes, in order to enhance the self-induced parametric amplification and the gyroscope rate sensitivity, while at the same time to reduce the individual modal Duffing nonlinearity terms in order to maximize the gyroscope linear range. This led to an objective function defined as the ratio of the dispersive modal coupling strength and the individual modal Duffing nonlinearity. Physically, this

objective function represents the amount of the parametric pumping that is induced by the drive mode on the sense mode, when the former is operated at the onset of its nonlinear regime. The optimization problem for these devices is easily formulated in terms of Fourier series, since the device must maintain its circular symmetry. The methods developed involve modifications in the gyroscope around its circumference. These include altering the electrostatic setup, both the gap distribution, which is typically uniform, and the use of different voltages in segmented electrodes, as well as the geometry of the resonator body, which alters its mechanical properties, both stiffness and inertial. Specifically, we have shown that if the gyroscope actuation/sensing scheme has at least 16 electrodes, it becomes possible to modify the intermodal coupling strength and the modal Duffing constant by applying a non-uniform distribution of the bias voltage. Additionally, we demonstrated that a non-uniform electrode gap size also affects the magnitude of the gyroscope nonlinear coefficients and can be used to tailor the gyroscope nonlinear dynamic behavior. Finally, we illustrated the applicability of the shape optimization method in manipulating nonlinear stiffness parameters of a thin spinning ring by altering the ring radial thickness along the ring circumference. Analysis shows that using proper modifications to the gyroscope/electrode geometry as well as the distribution of the bias voltage, one can significantly increase the value of the intermodal dispersive coupling strength while preserving the gyroscope dynamic range. In this case, the gyroscope rate sensitivity is expected to increase by more than an order of magnitude. Future work in this area includes experimental demonstration of the approach, as well as the use of more sophisticated optimization tools that allow for more general designs. The latter will be essential for complex geometries, such as those in disk resonating gyros (DRGs). The analytical results presented here can be used for predicting the nonlinear behavior of existing gyroscopes and proposed gyroscope models, and, more importantly, for designing

ring/disk resonating gyroscopes with optimized performance and maximized sensitivity using their inherent dynamics. Possible future directions include adapting the tuning methods presented here for application in real ring/disk resonating gyroscopes in attempt to improve their dynamic range and angular rate sensitivity.

In summary, the topics of this dissertation demonstrate the following point for MEMS resonators: (i) the utility of systematic modeling, (ii) the importance of nonlinear behavior, (iii) the importance of accounting for noise, and (iv) the utility of the previous items in characterization and design.

APPENDICES

Appendix A

Poisson noise in the resonator eigenfrequency

The analysis of the resonator quadrature probability distribution presented in Section 2.3 can be extended to account for the case when the resonator eigenfrequency fluctuations have Poisson statistics. This is of particular interest, for example, in systems where attachment/detachment of molecules to a resonator causes fluctuations of the resonator effective mass and, as a result, of the resonator eigenfrequency [51]. In this case the governing equation of motion for the resonator, Eq. (2.2), can be written as

$$\ddot{\theta} + 2\Gamma\dot{\theta} + (\omega_0^2 + \xi_\omega(t) + h\cos\omega t)\theta + \gamma\theta^3 = 0, \tag{A1}$$

where $\xi(t)$ is the regular Poisson noise of the form $\xi_\omega(t) = g\sum_j \delta(t - t_j)$ and we disregard thermal noise for simplicity. Of course, its effect can be accounted for in a similar way to that in Section 2.3.3. From Eq. (A1), it follows that the resonator dynamics in the rotating frame can now be described, similarly to Eq. (2.7), as

$$\dot{\boldsymbol{q}} = \boldsymbol{K}(\boldsymbol{q}) + \boldsymbol{l_q}\xi_\omega(\tau), \tag{A2}$$

where $\boldsymbol{l_q} = (Y, -X)^T$ is the pulse direction in the rotating frame as determined by the current state of the system and $\xi_\omega(\tau)$ is the Poisson noise with the mean pulse rate $\nu' = \nu/\Gamma$ and pulse area $g' = g/\omega_0$.

To study the quadrature probability distribution with weak multiplicative noise of Poisson type, one needs to linearize Eq. (A2) about its deterministic stationary solution $\boldsymbol{q}_0$. In this case $\boldsymbol{l_q} = (Y_0, -X_0)^T$ and in order to observe the effect of ξ_ω, one has to pump the system above its threshold to ensure that $\boldsymbol{q}_0 \neq 0$. The rest of the analysis is then similar to that presented in Section 2.3. The important feature of the resonator with multiplicative Poisson noise, as compared with the system described in detail in Chapter 2, is that the direction of the Poisson pulses in the rotating frame $\boldsymbol{l_q}$ is now predetermined by the location of the resonator operating point $\boldsymbol{q}_0$, which is generally more difficult to control in the experiment. Nevertheless, one still has freedom to choose different directions for the measurement quadrature q_m and to analyze the resonator quadrature probability distribution in both overdamped and underdamped regimes.

Appendix B

Mechanical and electrostatic effects in clamped-clamped beam resonators

In this section we formally derive mechanical and electrostatic contributions to the restoring force of MEMS resonators with "clamped-clamped beam" topology. By including both mechanical and electrostatic forces, discussed in Section 3.3.3 and acting on the resonator per unit length, we can obtain the following model for the unforced flexural vibrations of the DA-DETF resonator under study [45],

$$\rho S\ddot{y} + c(y,\dot{y})\dot{y} = -EIy^{(4)} + F_s(x,t) + F_e(x,t), \tag{B.1}$$

where $y = y(x,t)$ is the resonator physical displacement (x is the coordinate along the resonator length), ρ, E, and I are the resonator mass density, Young's modulus and the cross-sectional moment of inertia and $c(y,\dot{y})\dot{y}$ is the phenomenological resonator damping force, which can be linear or nonlinear [35]. The first term on the right-hand side of Eq. (B.1) represents the effect of beam bending, the term

$$F_s(x,t) = \frac{ES}{L}y'' \int_0^L dx\big(\sqrt{1+(y')^2} - 1\big) \tag{B.2}$$

accounts for the resonator mid-line stretching effect, and $F_e(x,t)$ is the electrostatic force due to the finite bias voltage between the resonator body and attendant electrodes. Since the electrode gap size $d \ll L$, where L is the resonator length, we can safely apply a local parallel plate assumption and write the electrostatic force acting on a symmetrically biased clamped-clamped beam micromechanical resonator as

$$F_e(x,t) = \kappa\big[(d-y)^{-2} - (d+y)^{-2}\big] = 4\kappa dy(d^2-y^2)^{-2}, \tag{B.3}$$

where $\kappa = \epsilon_0 w V_b^2/2$ is the strength of the electrostatic force, which depends on the resonator thickness w in the direction perpendicular to the resonator vibrations and the bias voltage V_b. Note that $\epsilon_0 = 8.85 \times 10^{-12}\ F/m$ is the vacuum permittivity.

In order to examine the mechanical and electrostatic effects on the dynamics of a particular vibrational mode, one has to perform the Galerkin projection of Eq. (B.1) onto the mode of interest. This is commonly done by separating temporal t and spatial x variables as $y(X,t) = q(t)\theta(X)$ with $X = x/L$, where $q(t)$ is the time-dependent modal coordinate and $\phi(X)$ is the mode shape. Finding an exact expression for $\theta(X)$ is generally a challenging problem, and it can be solved in the closed form only for certain systems in their linear range. In practice, however, modal nonlinearities as well as deviations of the device boundary conditions from an ideal clamped-clamped model result in the distortion of linear mode shapes. In this case we employ very practical method of assumed modes, and since here we focus on the primary flexural mode of the DA-DETF resonator, we choose $\theta(X) = \sin^2 \pi X$, which closely resembles the actual deformation profile of a clamped-clamped beam. Projecting

Eq. (B.1) on $\theta(X)$ yields

$$\ddot{q}+2\Gamma(q,\dot{q})\dot{q}+\omega_{0m}^2 q+C_m\left[\frac{2}{\pi}E\left(-\pi^2 q_L^2\right)-1\right]q+C_e\left[\frac{1}{(1+q_d)^{3/2}}-\frac{1}{(1-q_d)^{3/2}}\right]=0, \quad \text{(B.4)}$$

where $\omega_{0m}=4\pi^2\sqrt{EI/3\rho SL^4}$ is the linear mechanical modal frequency due to bending effects, $C_m=4\pi^2E/3\rho L^2$ is the strength of the mechanical potential due to the mid-line stretching, $C_e=2\epsilon_0 wV_b^2/3\rho Sd^2$ represents the strength of electrostatic contribution to the system restoring force and $q_\alpha=q/\alpha$ is the modal coordinate scaled with the appropriate length scale, d or L. For the sake of generality, we keep the modal decay rate $\Gamma(q,\dot{q})$ in its general form, since dissipation does not affect the modal vibration frequency in the resonator ringdown response [35].

The effect of the electrostatic actuation/sensing scheme represented in Eq. (B.4) by the term $\propto C_e$ contributes to both linear and nonlinear components of the resonator restoring force. In the lowest order, $\propto q$, the electrostatic forces affect the resonator vibration frequency as $\omega_0=\sqrt{\omega_{0m}^2-3C_e/d}$, the well-known phenomenon frequently used for tuning modal frequencies in MEMS resonant devices, e.g. for matching modal frequencies in MEMS vibratory gyroscopes. When the modal vibration amplitude exceeds the resonator linear range, its vibration frequency becomes amplitude-dependent due to the effect of the resonator mid-line stretching and anharmonic terms in the electrostatic potential. After the linear range, the resonator enters its Duffing range, where the system dynamic behavior is determined by quadratic and cubic terms in the resonator restoring force. In symmetrically biased resonators, however, the resonator restoring force does not contain quadratic terms, as well as higher-order nonlinear terms with even powers of q, which can be easily verified by expanding nonlinear terms in Eq. (B.4). As the resonator amplitude increases in the Duffing

range, the resonator frequency either increases, see Fig. 3.3, if the mechanical effect of the mid-line stretching dominates over electrostatic nonlinearities or decreases in the opposite scenario. From Fig. 3.3 it is clear, however, that the resonator frequency is a non-monotonic function of the modal amplitude, which cannot be explained by relatively simple Duffing model. In this case, higher-order quintic terms (we disregard quartic terms due to the symmetry reasons) in the modal restoring force must be taken into account in order to capture and explain the experimental observation.

Mechanical and electrostatic contributions to the resonator amplitude-frequency relationship can be demonstrated if we write the resonator modal displacement as in **??**. In the light of our previous discussion, we focus our attention on the dynamics of the slowly varying resonator phase $\phi(t)$; by applying the method of averaging [144] to Eq. (B.4), we obtain,

$$\dot{\phi} = \Delta\omega_m(a) + \Delta\omega_e(a), \tag{B.5a}$$

$$\begin{aligned}\Delta\omega_m(a_L) = \frac{C_m}{2\omega_0 a_L}\Bigg[\frac{8}{3\pi^4 a_L}\Bigg(E^2(Q)(4\pi^2 a_L^2 - 2) - K^2(Q)(1 - \pi^2 a_L^2 + \sqrt{1+\pi^2 a_L^2}) \\ +2E(Q)K(Q)(1 - 2\pi^2 a_L^2 + \sqrt{1+\pi^2 a_L^2}) - a_L\Bigg],\end{aligned} \tag{B.5b}$$

$$\begin{aligned}\Delta\omega_e(a_d) = -\frac{2C_e}{\pi\omega_0 d}\frac{1}{a_d^2(1-a_d^2)^{3/2}} \\ \times\Bigg[E\left(\frac{2a_d}{a_d-1}\right)\sqrt{1-a_d^2}(\sqrt{1-a_d} + \sqrt{1+a_d}) - K\left(\frac{2a_d}{a_d-1}\right)\sqrt{1+a_d}(1-a_d^2)\Bigg],\end{aligned} \tag{B.5c}$$

where $\Delta\omega_m(a)$ and $\Delta\omega_e(a)$ are the mechanical and electrostatic amplitude-dependent shifts of the modal vibration frequency due the resonator mid-line stretching and electrostatic interaction of the resonator with the attendant electrodes of the actuation/sensing scheme, respectively. In above expressions, $a_L = a/L$, $a_d = a/d$, $Q = \frac{1}{2} - \frac{1}{2}\sqrt{1+\pi^2 a_L^2}$, and $K(\dots)$ and $E(\dots)$ are complete elliptic integrals of the first and second kind, respectively. As it

follows from Eqs. (B.5b) and (B.5c), mechanical and electrostatic corrections to the resonator frequency, written in their closed from, have quite complicated form and, as a result, we use their Taylor expansions in Section 3.3.3 in order to apply the ringdown-based method for independent characterization of mechanical and electrostatic contributions to the resonator stiffness parameters. Nevertheless, Eqs. (B.5b) and (B.5c) are useful when one would like to study the resonator dynamic behavior within a large range of vibrational amplitudes.

Appendix C

Derivation of nonlinear strain-displacement relationships in a free ring

Here we derive the nonlinear strain-displacement relationships for $\epsilon_{ij}(u, v)$ presented in Eqs. (4.5a) to (4.5c). In order to do so, we consider an infinitesimal segment of the gyroscope body, designated by $KLMN$ in with coordinates r and θ and having radial thickness dr and angular length $rd\theta$; see Fig. C.1. This segment can be conveniently defined in terms of the coordinates of its corner points as

$$K = (r, \theta),\ L = (r + dr, \theta),\ M = (r + dr, \theta + d\theta),\ N = (r, \theta + d\theta). \tag{C.1}$$

During operation the body experiences elastic deformations and the segment deforms into

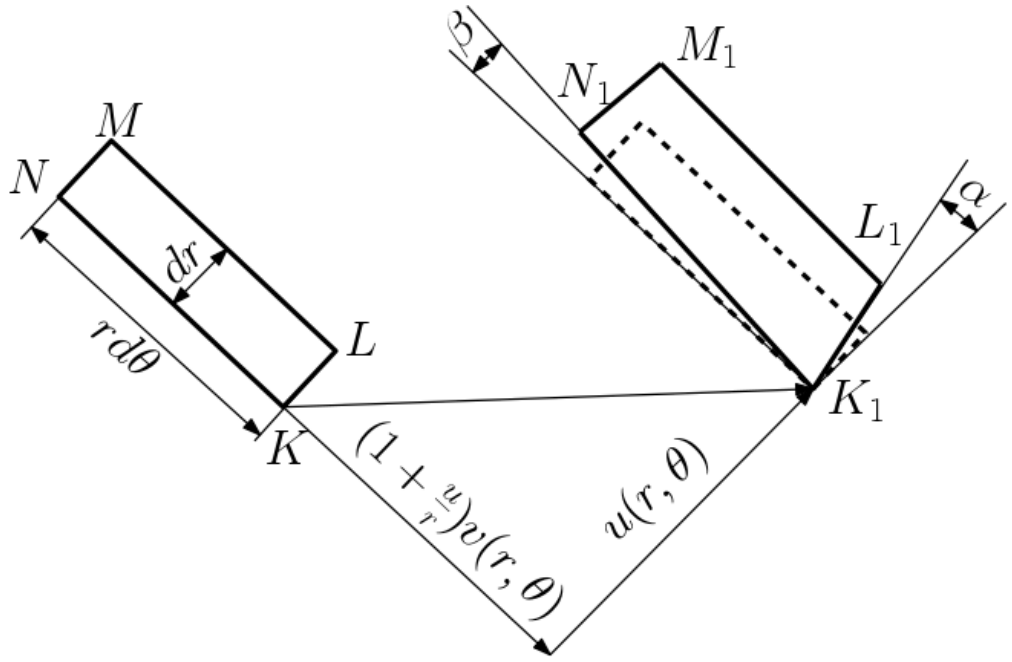

Figure C.1: Deformation of the gyroscope segment $KLMN$ into $K_1L_1M_1N_1$.

$K_1L_1M_1N_1$, which we, in turn, express as

$$\begin{aligned}
K_1 &= \left(r + u(r,\theta), \theta + \frac{v(r,\theta)}{r}\right), \\
L_1 &= \left(r + dr + u(r+dr,\theta), \theta + \frac{v(r+dr,\theta)}{r+dr}\right), \\
M_1 &= \left(r + dr + u(r+dr,\theta+d\theta), \theta + d\theta + \frac{v(r+dr,\theta+d\theta)}{r+dr}\right), \\
N_1 &= \left(r + u(r,\theta+d\theta), \theta + d\theta + \frac{v(r,\theta+d\theta)}{r}\right).
\end{aligned} \tag{C.2}$$

From Fig. C.1 it is clear that the strain-displacement relationships $\epsilon_{ij}(u,v)$ are given by

$$\epsilon_{rr} = \frac{K_1L_1 - KL}{KL},\ \epsilon_{\theta\theta} = \frac{K_1N_1 - KN}{KN},\ \epsilon_{r\theta} = \alpha + \beta. \tag{C.3}$$

Given the coordinate representations of the segment corner points in Eqs. (C.1) and (C.2),

we have

$$KL = dr,\ K_1L_1 \approx dr\sqrt{\left(1+\frac{\partial u}{\partial r}\right)^2+\left(1+\frac{u}{r}\right)^2\left(\frac{\partial v}{\partial r}\right)^2}, \tag{C.4a}$$

$$KN \approx rd\theta,\ K_1N_1 \approx rd\theta\sqrt{\left(1+\frac{u}{r}\right)^2\left(1+\frac{\partial v}{r\partial\theta}\right)^2+\frac{1}{r^2}\left(\frac{\partial u}{\partial\theta}\right)^2}, \tag{C.4b}$$

$$\alpha \approx \frac{r+u}{1+\partial u/\partial r}\frac{\partial}{\partial r}\left(\frac{v}{r}\right),\ \beta \approx \frac{\partial u/\partial\theta}{(r+u)(1+\partial v/r\partial\theta)}. \tag{C.4c}$$

Finally, by using Eqs. (C.4a) to (C.4c) in Eq. (C.3) and expanding the resulting expressions up to the second order in u and v, we obtain the nonlinear strain-displacement relationships given in Eqs. (4.5a) to (4.5c).

BIBLIOGRAPHY

BIBLIOGRAPHY

[1] Dario Antonio, Damián H Zanette, and Daniel López. Frequency stabilization in nonlinear micromechanical oscillators. *Nature communications*, 3:806, 2012.

[2] Eyal Kenig, MC Cross, LG Villanueva, RB Karabalin, MH Matheny, Ron Lifshitz, and ML Roukes. Optimal operating points of oscillators using nonlinear resonators. *Physical Review E*, 86(5):056207, 2012.

[3] Alexandra Nafari, David Karlen, Cristina Rusu, Krister Svensson, Håkan Olin, and Peter Enoksson. MEMS sensor for in situ TEM atomic force microscopy. *Microelectromechanical Systems, Journal of*, 17(2):328–333, 2008.

[4] G Prakash, S Hu, Arvind Raman, and R Reifenberger. Theoretical basis of parametric-resonance-based atomic force microscopy. *Physical Review B*, 79(9):094304, 2009.

[5] T Ouisse, M Stark, Frederico Rodrigues-Martins, B Bercu, S Huant, and J Chevrier. Theory of electric force microscopy in the parametric amplification regime. *Physical Review B*, 71(20):205404, 2005.

[6] B Scott Strachan, Steven W Shaw, and Oleg Kogan. Subharmonic resonance cascades in a class of coupled resonators. *Journal of Computational and Nonlinear Dynamics*, 8(4):041015, 2013.

[7] KR Qalandar, BS Strachan, B Gibson, M Sharma, A Ma, SW Shaw, and KL Turner. Frequency division using a micromechanical resonance cascade. *Applied Physics Letters*, 105(24):244103, 2014.

[8] AN Cleland and ML Roukes. Noise processes in nanomechanical resonators. *Journal of Applied Physics*, 92(5):2758–2769, 2002.

[9] Akihisa Ichiki, Yukihiro Tadokoro, and MI Dykman. Singular probability distribution of shot-noise driven systems. *Physical Review E*, 87(1):012119, 2013.

[10] JS Aldridge and AN Cleland. Noise-enabled precision measurements of a Duffing nanomechanical resonator. *Physical review letters*, 94(15):156403, 2005.

[11] Richard P Feynman. There's plenty of room at the bottom. *Engineering and science*, 23(5):22–36, 1960.

[12] Harvey C Nathanson, William E Newell, Robert Wickstrom, John Ransford Davis Jr, et al. The resonant gate transistor. *Electron Devices, IEEE Transactions on*, 14(3):117–133, 1967.

[13] Kurt E Petersen. Silicon as a mechanical material. *Proceedings of the IEEE*, 70(5):420–457, 1982.

[14] T Mattila, J Kiihamäki, T Lamminmäki, O Jaakkola, P Rantakari, A Oja, H Seppä, H Kattelus, and I Tittonen. A 12 MHz micromechanical bulk acoustic mode oscillator. *Sensors and Actuators A: Physical*, 101(1):1–9, 2002.

[15] Ville Kaajakari, Jukka K Koskinen, and Tomi Mattila. Phase noise in capacitively coupled micromechanical oscillators. *Ultrasonics, Ferroelectrics, and Frequency Control, IEEE Transactions on*, 52(12):2322–2331, 2005.

[16] Claude Audoin and Bernard Guinot. *The measurement of time: time, frequency and the atomic clock*. Cambridge University Press, 2001.

[17] Arkady Pikovsky, Michael Rosenblum, and Jürgen Kurths. *Synchronization: a universal concept in nonlinear sciences*. Cambridge university press, 2003.

[18] YT Yang, Carlo Callegari, XL Feng, KL Ekinci, and ML Roukes. Zeptogram-scale nanomechanical mass sensing. *Nano letters*, 6(4):583–586, 2006.

[19] Farrokh Ayazi and Khalil Najafi. A HARPSS polysilicon vibrating ring gyroscope. *Microelectromechanical Systems, Journal of*, 10(2):169–179, 2001.

[20] Liwei Lin, Roger T Howe, and Albert P Pisano. Microelectromechanical filters for signal processing. *Microelectromechanical Systems, Journal of*, 7(3):286–294, 1998.

[21] Mariateresa Napoli, Wenhua Zhang, Kimberly Turner, and Bassam Bamieh. Characterization of electrostatically coupled microcantilevers. *Microelectromechanical Systems, Journal of*, 14(2):295–304, 2005.

[22] RMC Mestrom. *Multiphysics modelling and experimental validation of microelectromechanical resonator dynamics*. PhD thesis, Technische Universiteit Eindhoven, 2009.

[23] Clark T-C Nguyen. MEMS technology for timing and frequency control. *Ultrasonics, Ferroelectrics, and Frequency Control, IEEE Transactions on*, 54(2):251–270, 2007.

[24] Sassan Tabatabaei and Aaron Partridge. Silicon MEMS oscillators for high-speed digital systems. *IEEE micro*, 30(2):80–89, 2010.

[25] JTM Van Beek and R Puers. A review of MEMS oscillators for frequency reference and timing applications. *Journal of Micromechanics and Microengineering*, 22(1):013001, 2012.

[26] Reza Abdolvand, Babak Vakili Amini, and Farrokh Ayazi. Sub-micro-gravity in-plane accelerometers with reduced capacitive gaps and extra seismic mass. *Microelectromechanical Systems, Journal of*, 16(5):1036–1043, 2007.

[27] Sarah H Nitzan, Valentina Zega, Mo Li, Chae H Ahn, Alberto Corigliano, Thomas W Kenny, and David A Horsley. Self-induced parametric amplification arising from nonlinear elastic coupling in a micromechanical resonating disk gyroscope. *Scientific reports*, 5, 2015.

[28] TD Stowe, K Yasumura, TW Kenny, D Botkin, K Wago, and D Rugar. Attonewton force detection using ultrathin silicon cantilevers. *Applied Physics Letters*, 71:288–290, 1997.

[29] Daniel Rugar, R Budakian, HJ Mamin, and BW Chui. Single spin detection by magnetic resonance force microscopy. *Nature*, 430(6997):329–332, 2004.

[30] Hyung Kyu Lee, Renata Melamud, Saurabh Chandorkar, James Salvia, Shingo Yoneoka, and Thomas W Kenny. Stable operation of MEMS oscillators far above the critical vibration amplitude in the nonlinear regime. *Journal of microelectromechanical systems*, 20(6):1228–1230, 2011.

[31] Ville Kaajakari, Tomi Mattila, Antti Lipsanen, and Aarne Oja. Nonlinear mechanical effects in silicon longitudinal mode beam resonators. *Sensors and Actuators A: Physical*, 120(1):64–70, 2005.

[32] A Eichler, Joel Moser, J Chaste, M Zdrojek, I Wilson-Rae, and Adrian Bachtold. Nonlinear damping in mechanical resonators made from carbon nanotubes and graphene. *Nature nanotechnology*, 6(6):339–342, 2011.

[33] MI Dykman and MA Krivoglaz. Spectral distribution of nonlinear oscillators with nonlinear friction due to a medium. *physica status solidi (b)*, 68(1):111–123, 1975.

[34] Stav Zaitsev, Oleg Shtempluck, Eyal Buks, and Oded Gottlieb. Nonlinear damping in a micromechanical oscillator. *Nonlinear Dynamics*, 67(1):859–883, 2012.

[35] Pavel M Polunin, Yushi Yang, Mark I Dykman, Thomas W Kenny, and Steven W Shaw. Characterization of MEMS resonator nonlinearities using the ringdown response. *Journal of Microelectromechanical Systems*, 25(2):297–303, 2016.

[36] Barry E DeMartini, Jeffrey F Rhoads, Kimberly L Turner, Steven W Shaw, and Jeff Moehlis. Linear and nonlinear tuning of parametrically excited MEMS oscillators. *Microelectromechanical Systems, Journal of*, 16(2):310–318, 2007.

[37] Mohammad I Younis. *MEMS linear and nonlinear statics and dynamics*, volume 20. Springer Science & Business Media, 2011.

[38] Chae Hyuck Ahn, Eldwin J Ng, Vu Hong, Yushi Yang, Brian J Lee, Ian Flader, Thomas W Kenny, et al. Mode-matching of wineglass mode disk resonator gyroscope in (100) single crystal silicon. *Microelectromechanical Systems, Journal of*, 24(2):343–350, 2015.

[39] M Saghafi, H Dankowicz, and W Lacarbonara. Nonlinear tuning of microresonators for dynamic range enhancement. In *Proc. R. Soc. A*, volume 471, page 20140969. The Royal Society, 2015.

[40] Congzhong Guo and Gary K Fedder. A quadratic-shaped-finger comb parametric resonator. *Journal of Micromechanics and Microengineering*, 23(9):095007, 2013.

[41] E Tatar, T Mukherjee, and GK Fedder. Nonlinearity tuning and its effects on the performance of a MEMS gyroscope. In *Solid-State Sensors, Actuators and Microsystems (TRANSDUCERS), 2015 Transducers-2015 18th International Conference on*, pages 1133–1136. IEEE, 2015.

[42] Wenjing Ye, Subrata Mukherjee, and Noel C MacDonald. Optimal shape design of an electrostatic comb drive in microelectromechanical systems. *Microelectromechanical Systems, Journal of*, 7(1):16–26, 1998.

[43] Suguang Dou, B Scott Strachan, Steven W Shaw, and Jakob S Jensen. Structural optimization for nonlinear dynamic response. *Phil. Trans. R. Soc. A*, 373(2051):20140408, 2015.

[44] Yushi Yang, Eldwin J Ng, Vu A Hong, Chae Hyuck Ahn, Yunhan Chen, Elia Ahadi, Mark Dykman, and Thomas W Kenny. Measurement of the nonlinear elasticity of doped bulk-mode MEMS resonators. 2014.

[45] Ron Lifshitz and MC Cross. Nonlinear dynamics of nanomechanical and micromechanical resonators. *Review of nonlinear dynamics and complexity*, 1:1–52, 2008.

[46] Steven W. Shaw, Oriel Shoshani, and Pavel M. Polunin. Modeling for non-linear vibrational response of mechanical systems. In Friedrich Pfeiffer and Hartmut Bremer, editors, *The Art of Modeling Mechanical Systems (in print)*. Springer, 2017.

[47] MRM Crespo da Silva and CC Glynn. Out-of-plane vibrations of a beam including non-linear inertia and non-linear curvature effects. *International Journal of Non-Linear Mechanics*, 13(5):261–271, 1978.

[48] LG Villanueva, RB Karabalin, MH Matheny, D Chi, JE Sader, and ML Roukes. Nonlinearity in nanomechanical cantilevers. *Physical Review B*, 87(2):024304, 2013.

[49] MI Dykman and MA Krivoglaz. Theory of nonlinear oscillator interacting with a medium. *Soviet Physics Reviews*, 5:265–442, 1984.

[50] Nicholas J. Miller. *Noise in nonlinear micro-resonators*. PhD thesis, Michigan State University, 2012.

[51] MI Dykman, M Khasin, J Portman, and SW Shaw. Spectrum of an oscillator with jumping frequency and the interference of partial susceptibilities. *Physical review letters*, 105(23):230601, 2010.

[52] Leonid S Levitov, Hyunwoo Lee, and Gordey B Lesovik. Electron counting statistics and coherent states of electric current. *Journal of Mathematical Physics*, 37(10):4845–4866, 1996.

[53] Yu Bomze, G Gershon, D Shovkun, LS Levitov, and M Reznikov. Measurement of counting statistics of electron transport in a tunnel junction. *Physical review letters*, 95(17):176601, 2005.

[54] Christian Fricke, Frank Hohls, Nandhavel Sethubalasubramanian, Lukas Fricke, and Rolf J Haug. High-order cumulants in the counting statistics of asymmetric quantum dots. *Applied Physics Letters*, 96(20):202103, 2010.

[55] Lora Billings, Mark I Dykman, and Ira B Schwartz. Thermally activated switching in the presence of non-Gaussian noise. *Physical Review E*, 78(5):051122, 2008.

[56] Nicholas J Miller, Pavel M Polunin, Mark I Dykman, and Steven W Shaw. The balanced dynamical bridge: Detection and sensitivity to parameter shifts and non-Gaussian noise. In *ASME 2012 International Design Engineering Technical Conferences and Computers and Information in Engineering Conference*, pages 487–496. American Society of Mechanical Engineers, 2012.

[57] Jie Zou, Sanal Buvaev, Mark Dykman, and Ho Bun Chan. Poisson noise induced switching in driven micromechanical resonators. *Physical Review B*, 86(15):155420, 2012.

[58] J Tobiska and Yu V Nazarov. Josephson junctions as threshold detectors for full counting statistics. *Physical review letters*, 93(10):106801, 2004.

[59] Jukka P Pekola. Josephson junction as a detector of Poissonian charge injection. *Physical review letters*, 93(20):206601, 2004.

[60] Joachim Ankerhold. Detecting charge noise with a Josephson junction: A problem of thermal escape in presence of non-Gaussian fluctuations. *Physical review letters*, 98(3):036601, 2007.

[61] C Van den Broeck and P Hänggi. Activation rates for nonlinear stochastic flows driven by non-Gaussian noise. *Physical Review A*, 30(5):2730, 1984.

[62] Adrian Baule and EGD Cohen. Fluctuation properties of an effective nonlinear system subject to Poisson noise. *Physical Review E*, 79(3):030103, 2009.

[63] Pawel Romanczuk, Markus Bär, Werner Ebeling, Benjamin Lindner, and Lutz Schimansky-Geier. Active brownian particles. *The European Physical Journal Special Topics*, 202(1):1–162, 2012.

[64] MI Dykman. Poisson-noise-induced escape from a metastable state. *Physical Review E*, 81(5):051124, 2010.

[65] Ali H Nayfeh and Dean T Mook. *Nonlinear oscillations*. John Wiley & Sons, 2008.

[66] Dennis Zill, Warren S Wright, and Michael R Cullen. *Advanced engineering mathematics*. Jones & Bartlett Learning, 2011.

[67] Hannes Risken. *Fokker-Planck equation*. Springer, 1984.

[68] Richard P Feynman, Albert R Hibbs, and Daniel Styer. *Quantum mechanics and path integrals*. Dover Publications, 2010.

[69] Milton Abramowitz and Irene A Stegun. *Handbook of mathematical functions: with formulas, graphs, and mathematical tables*, volume 55. Courier Corporation, 1964.

[70] Carl M Bender and Steven A Orszag. *Advanced mathematical methods for scientists and engineers*. Springer Science & Business Media, 1999.

[71] HSY Chan, Z Xu, and WL Huang. Estimation of nonlinear damping coefficients from large-amplitude ship rolling motions. *Applied ocean research*, 17(4):217–224, 1995.

[72] L Gaul and J Lenz. Nonlinear dynamics of structures assembled by bolted joints. *Acta Mechanica*, 125(1-4):169–181, 1997.

[73] Jose L Trueba, Joaquin Rams, and Miguel AF Sanjuan. Analytical estimates of the effect of nonlinear damping in some nonlinear oscillators. *International Journal of Bifurcation and Chaos*, 10(09):2257–2267, 2000.

[74] Jose P Baltanas, Jose L Trueba, and Miguel AF Sanjuan. Energy dissipation in a nonlinearly damped Duffing oscillator. *Physica D: Nonlinear Phenomena*, 159(1):22–34, 2001.

[75] Jeffrey F Rhoads, Steven W Shaw, and Kimberly L Turner. Nonlinear dynamics and its applications in micro-and nanoresonators. *Journal of Dynamic Systems, Measurement, and Control*, 132(3):034001, 2010.

[76] Yushi Yang, Eldwin Ng, Pavel Polunin, Yunhan Chen, Scott Strachan, Vu Hong, Chae Hyuck Ahn, Ori Shoshani, Steven Shaw, Mark Dykman, et al. Experimental investigation on mode coupling of bulk mode silicon MEMS resonators. In *Micro Electro Mechanical Systems (MEMS), 2015 28th IEEE International Conference on*, pages 1008–1011. IEEE, 2015.

[77] Alexander Croy, Daniel Midtvedt, Andreas Isacsson, and Jari M Kinaret. Nonlinear damping in graphene resonators. *Physical Review B*, 86(23):235435, 2012.

[78] Yaxing Zhang, J Moser, J Güttinger, A Bachtold, and MI Dykman. Interplay of driving and frequency noise in the spectra of vibrational systems. *Physical review letters*, 113(25):255502, 2014.

[79] Eyal Buks and Bernard Yurke. Mass detection with a nonlinear nanomechanical resonator. *Physical Review E*, 74(4):046619, 2006.

[80] Mahmood Bagheri, Menno Poot, Mo Li, Wolfram PH Pernice, and Hong X Tang. Dynamic manipulation of nanomechanical resonators in the high-amplitude regime and non-volatile mechanical memory operation. *Nature nanotechnology*, 6(11):726–732, 2011.

[81] Gaetan Kerschen, Keith Worden, Alexander F Vakakis, and Jean-Claude Golinval. Past, present and future of nonlinear system identification in structural dynamics. *Mechanical systems and signal processing*, 20(3):505–592, 2006.

[82] Bongsang Kim, Matthew A Hopcroft, Rob N Candler, Chandra Mohan Jha, Manu Agarwal, Renata Melamud, Saurabh A Chandorkar, Gary Yama, and Thomas W Kenny. Temperature dependence of quality factor in MEMS resonators. *Microelectromechanical Systems, Journal of*, 17(3):755–766, 2008.

[83] P Polunin, Y Yang, J Atalaya, E Ng, S Strachan, O Shoshani, M Dykman, S Shaw, and T Kenny. Characterizing MEMS nonlinearities directly: The ring-down measurements. In *Solid-State Sensors, Actuators and Microsystems (TRANSDUCERS), 2015 Transducers-2015 18th International Conference on*, pages 2176–2179. IEEE, 2015.

[84] Alper Demir, Amit Mehrotra, and Jaijeet Roychowdhury. Phase noise in oscillators: a unifying theory and numerical methods for characterization. *Circuits and Systems I: Fundamental Theory and Applications, IEEE Transactions on*, 47(5):655–674, 2000.

[85] Eyal Kenig, MC Cross, Jeff Moehlis, and Kurt Wiesenfeld. Phase noise of oscillators with unsaturated amplifiers. *Physical Review E*, 88(6):062922, 2013.

[86] B Yurke, DS Greywall, AN Pargellis, and PA Busch. Theory of amplifier-noise evasion in an oscillator employing a nonlinear resonator. *Physical Review A*, 51(5):4211, 1995.

[87] Rob N Candler, Matthew Hopcroft, Bongsang Kim, Woo-Tae Park, Renata Melamud, Manu Agarwal, Gary Yama, Aaron Partridge, Markus Lutz, Thomas W Kenny, et al. Long-term and accelerated life testing of a novel single-wafer vacuum encapsulation for MEMS resonators. *Microelectromechanical Systems, Journal of*, 15(6):1446–1456, 2006.

[88] Andrew N Cleland. *Foundations of nanomechanics: from solid-state theory to device applications*. Springer Science & Business Media, 2013.

[89] N N Bogolyubov and Yu A Mitropolskii. *Asymptotic methods in the theory of nonlinear oscillations*, volume 10. CRC Press, 1961.

[90] Michael Feldman. Hilbert transform in vibration analysis. *Mechanical systems and signal processing*, 25(3):735–802, 2011.

[91] M Feldman. Nonparametric identification of asymmetric nonlinear vibration systems with the Hilbert transform. *Journal of Sound and Vibration*, 331(14):3386–3396, 2012.

[92] Julián M Londoño, Simon A Neild, and Jonathan E Cooper. Identification of backbone curves of nonlinear systems from resonance decay responses. *Journal of Sound and Vibration*, 348:224–238, 2015.

[93] Kari Moran, Christopher Burgner, Steven Shaw, and Kimberly Turner. A review of parametric resonance in microelectromechanical systems. *Nonlinear Theory and Its Applications, IEICE*, 4(3):198–224, 2013.

[94] KL Turner, PG Hartwell, and NC MacDonald. Multi-dimensional MEMS motion characterization using laser vibrometry. *Digest of Technical Papers Transducers' 99, Sendai, Japan*, 1999.

[95] William Weaver Jr, Stephen P Timoshenko, and Donovan Harold Young. *Vibration problems in engineering*. John Wiley & Sons, 1990.

[96] L. D. Landau and E. M. Lifshitz. *Mechanics*. Elsevier, Amsterdam, 3rd edition, 2004.

[97] Ali H Nayfeh, Mohammad I Younis, and Eihab M Abdel-Rahman. Dynamic pull-in phenomenon in MEMS resonators. *Nonlinear dynamics*, 48(1-2):153–163, 2007.

[98] Sayanu Pamidighantam, Robert Puers, Kris Baert, and Harrie AC Tilmans. Pull-in voltage analysis of electrostatically actuated beam structures with fixed-fixed and fixed-free end conditions. *Journal of Micromechanics and Microengineering*, 12(4):458, 2002.

[99] Jeffrey F Rhoads, Steven W Shaw, and Kimberly L Turner. The nonlinear response of resonant microbeam systems with purely-parametric electrostatic actuation. *Journal of Micromechanics and Microengineering*, 16(5):890, 2006.

[100] Marco Amabili and Michael P Paıdoussis. Review of studies on geometrically nonlinear vibrations and dynamics of circular cylindrical shells and panels, with and without fluid-structure interaction. *Applied Mechanics Reviews*, 56(4):349–381, 2003.

[101] Marco Amabili. *Nonlinear vibrations and stability of shells and plates*. Cambridge University Press, 2008.

[102] Paul Mansour Naghdi. *The theory of shells and plates*. Springer, 1973.

[103] F Moussaoui and R Benamar. Non-linear vibrations of shell-type structures: a review with bibliography. *Journal of sound and vibration*, 255(1):161–184, 2002.

[104] Andrei M Shkel. Type I and Type II micromachined vibratory gyroscopes. In *Position, Location, and Navigation Symposium, San Diego*, pages 25–27, 2006.

[105] Cenk Acar and Andrei Shkel. *MEMS vibratory gyroscopes: structural approaches to improve robustness*. Springer Science & Business Media, 2008.

[106] Navid Yazdi, Farrokh Ayazi, and Khalil Najafi. Micromachined inertial sensors. *Proceedings of the IEEE*, 86(8):1640–1659, 1998.

[107] Igor P Prikhodko, Alexander A Trusov, and Andrei M Shkel. Compensation of drifts in high-q mems gyroscopes using temperature self-sensing. *Sensors and Actuators A: Physical*, 201:517–524, 2013.

[108] Jae Yoong Cho, Jong-Kwan Woo, Jialiang Yan, Rebecca L Peterson, and Khalil Najafi. Fused-silica micro birdbath resonator gyroscope (μ-BRG). *Microelectromechanical Systems, Journal of*, 23(1):66–77, 2014.

[109] Igor P Prikhodko, Sergei A Zotov, Alexander A Trusov, and Andrei M Shkel. Microscale glass-blown three-dimensional spherical shell resonators. *Microelectromechanical Systems, Journal of*, 20(3):691–701, 2011.

[110] Todd Remtema and Liwei Lin. Active frequency tuning for micro resonators by localized thermal stressing effects. *Sensors and Actuators A: Physical*, 91(3):326–332, 2001.

[111] Chris C Painter and Andrei M Shkel. Active structural error suppression in MEMS vibratory rate integrating gyroscopes. *Sensors Journal, IEEE*, 3(5):595–606, 2003.

[112] Barry J Gallacher, John Hedley, James S Burdess, Alun James Harris, Alexandria Rickard, and David O King. Electrostatic correction of structural imperfections present in a microring gyroscope. *Microelectromechanical Systems, Journal of*, 14(2):221–234, 2005.

[113] Dong Joon Kim and Robert Closkey. A systematic method for tuning the dynamics of electrostatically actuated vibratory gyros. *Control Systems Technology, IEEE Transactions on*, 14(1):69–81, 2006.

[114] Riccardo Antonello, Roberto Oboe, Luciano Prandi, and Fabio Biganzoli. Automatic mode matching in MEMS vibrating gyroscopes using extremum-seeking control. *Industrial Electronics, IEEE Transactions on*, 56(10):3880–3891, 2009.

[115] SJ Wong, CHJ Fox, and S McWilliam. Thermoelastic damping of the in-plane vibration of thin silicon rings. *Journal of sound and vibration*, 293(1):266–285, 2006.

[116] Shirin Ghaffari, Eldwin Jiaqiang Ng, Chae Hyuck Ahn, Yushi Yang, Shasha Wang, Vu Hong, Thomas W Kenny, et al. Accurate modeling of quality factor behavior of complex silicon MEMS resonators. *Microelectromechanical Systems, Journal of*, 24(2):276–288, 2015.

[117] Jong-Hyun Lee, Boo-Yeon Choi, Kyung-ho Park, and Hyung-Joun Yoo. Vibrating disk type micro-gyroscope, July 21 1998. US Patent 5,783,749.

[118] Houri Johari and Farrokh Ayazi. Capacitive bulk acoustic wave silicon disk gyroscopes. In *Electron Devices Meeting, 2006. IEDM'06. International*, pages 1–4. IEEE, 2006.

[119] Randall L Kubena and David T Chang. Disc resonator gyroscopes, September 1 2009. US Patent 7,581,443.

[120] D Rugar and P Grütter. Mechanical parametric amplification and thermomechanical noise squeezing. *Physical Review Letters*, 67(6):699, 1991.

[121] Jeffrey F Rhoads, Steven W Shaw, Kimberly L Turner, and Rajashree Baskaran. Tunable microelectromechanical filters that exploit parametric resonance. *Journal of Vibration and Acoustics*, 127(5):423–430, 2005.

[122] Jeffrey F Rhoads, Steven W Shaw, Kimberly L Turner, Jeff Moehlis, Barry E DeMartini, and Wenhua Zhang. Generalized parametric resonance in electrostatically actuated microelectromechanical oscillators. *Journal of Sound and Vibration*, 296(4):797–829, 2006.

[123] Ales Tondl. *Autoparametric resonance in mechanical systems*. Cambridge University Press, 2000.

[124] J Warminski and K Kecik. Autoparametric vibrations of a nonlinear system with pendulum. *Mathematical Problems in Engineering*, 2006, 2006.

[125] S Fatimah and M Ruijgrok. Bifurcations in an autoparametric system in 1: 1 internal resonance with parametric excitation. *International journal of non-linear mechanics*, 37(2):297–308, 2002.

[126] HJR Westra, M Poot, HSJ Van der Zant, and WJ Venstra. Nonlinear modal interactions in clamped-clamped mechanical resonators. *Physical review letters*, 105(11):117205, 2010.

[127] Tyler Dunn, Josef-Stefan Wenzler, and Pritiraj Mohanty. Anharmonic modal coupling in a bulk micromechanical resonator. *Applied Physics Letters*, 97(12):123109, 2010.

[128] MH Matheny, LG Villanueva, RB Karabalin, John E Sader, and ML Roukes. Nonlinear mode-coupling in nanomechanical systems. *Nano letters*, 13(4):1622–1626, 2013.

[129] David A Evensen. Nonlinear flexural vibrations of thin circular rings. *Journal of Applied Mechanics*, 33(3):553–560, 1966.

[130] A Maewal. Nonlinear harmonic oscillations of gyroscopic structural systems and the case of a rotating ring. *Journal of Applied Mechanics*, 48(3):627–633, 1981.

[131] S Natsiavas. Dynamics and stability of non-linear free vibration of thin rotating rings. *International journal of non-linear mechanics*, 29(1):31–48, 1994.

[132] W Kim and J Chung. Free non-linear vibration of a rotating thin ring with the in-plane and out-of-plane motions. *Journal of Sound and Vibration*, 258(1):167–178, 2002.

[133] CH Ahn, S Nitzan, EJ Ng, VA Hong, Y Yang, T Kimbrell, DA Horsley, and TW Kenny. Encapsulated high frequency (235 kHz), high-Q (100 k) disk resonator gyroscope with electrostatic parametric pump. *Applied Physics Letters*, 105(24):243504, 2014.

[134] Werner Soedel. *Vibrations of shells and plates*. CRC Press, 2004.

[135] Chan Il Park. Frequency equation for the in-plane vibration of a clamped circular plate. *Journal of Sound and Vibration*, 313(1):325–333, 2008.

[136] Satya Prasad Maganty and WB Bickford. Large amplitude oscillations of thin circular rings. *Journal of applied mechanics*, 54(2):315–322, 1987.

[137] Wenhua Zhang and Kimberly L Turner. Application of parametric resonance amplification in a single-crystal silicon micro-oscillator based mass sensor. *Sensors and Actuators A: Physical*, 122(1):23–30, 2005.

[138] Fadi M Alsaleem, Mohammad I Younis, and Laura Ruzziconi. An experimental and theoretical investigation of dynamic pull-in in MEMS resonators actuated electrostatically. *Microelectromechanical Systems, Journal of*, 19(4):794–806, 2010.

[139] S Nima Mahmoodi, Nader Jalili, and Siamak E Khadem. An experimental investigation of nonlinear vibration and frequency response analysis of cantilever viscoelastic beams. *Journal of Sound and vibration*, 311(3):1409–1419, 2008.

[140] MRM Crespo da Silva and CC Glynn. Nonlinear flexural-flexural-torsional dynamics of inextensional beams. I. Equations of motion. *Journal of Structural Mechanics*, 6(4):437–448, 1978.

[141] John Guckenheimer and Philip Holmes. *Nonlinear oscillations, dynamical systems, and bifurcations of vector fields*, volume 42. Springer Science & Business Media, 2013.

[142] Kimberly L Turner, Scott A Miller, Peter G Hartwell, Noel C MacDonald, Steven H Strogatz, and Scott G Adams. Five parametric resonances in a microelectromechanical system. *Nature*, 396(6707):149–152, 1998.

[143] Astitva Tripathi and Anil K Bajaj. Computational synthesis for nonlinear dynamics based design of planar resonant structures. *Journal of Vibration and Acoustics*, 135(5):051031, 2013.

[144] Nikolai N Bogoliubov and Yuri A Mitropolskii. *Asymptotic methods in the theory of non-linear oscillations*, volume 10. CRC Press, 1961.